IUNIVERSITY OF QUEBEC AT CHICOUTIMI

A DISSERTATION PRESENTED TO THE UNIVERSITY OF

QUEBEC AT CHICOUTIMI IN PARTIAL FULFILLMENT

OF THE REQUIREMENTS FOR THE DOCTOR

OF PHILOSOPHY IN ENGINEERING

BY

JIAN QIN

MECHANICAL PROPERTIES AND HOT WORKABILITY OF AL-15%B_4C METAL MATRIX COMPOSITES WITH SC AND ZR FOR ELEVATED TEMPERATURE APPLICATIONS

JUNE 2016

UNIVERSITE DU QUEBEC A CHICOUTIMI

THESE PRÉSENTÉ À L'UNIVERSITÉ DU QUÉBEC À

CHICOUTIMI COMME EXIGENCE PARTIELLE DU DOCTORAT

EN INGÉNIERIE

PAR

JIAN QIN

PROPRIETES MECANIQUES ET MANIABILITÉ CHAUD DE AL-15% COMPOSITES B_4C METAL MATRIX AVEC SC ET ZR POUR APPLICATIONS À CHAUD

JUN 2016

ABSTRCT

The study presented in this thesis focuses on mechanical properties and hot workability of Al–15vol.% B_4C metal matrix composites (MMCs) with scandium and zirconium for elevated temperature applications. The mechanical properties and their thermal stability, strengthening mechanisms, microstructure features, heat treatment, hot deformation and processing maps of as-cast and hot deformed Al–B_4C composites with scandium and zirconium was investigated.

In this study, the mechanical properties and long-term thermal stability of the composites at ambient and elevated temperatures were evaluated by Vickers' hardness measurements, tensile and compression tests, respectively. A transmission electron microscope, a scanning electron microscope and an optical microscope equipped with an image analysis system were employed to observe and quantitatively analyze the precipitation, grain and sub-grains structure, dislocations and tensile fractures of the composites. To examine the hot deformation and workability of the composites, uniaxial compression tests were performed at various strain rates and deformation temperatures using a Gleeble-3800 thermo-mechanical simulation unit.

The results of the present thesis are divided into three parts.

In the first part, scandium and zirconium as alloying elements were introduced into Al–15 vol.% B_4C composites to examine the effect of precipitates and B_4C particles on the mechanical properties and their thermal stability of as cast Al–B_4C composites at ambient and elevated temperatures. It was found that the presence of B_4C particles with microscale dimension has a moderate but stable strengthening effect on Al–B_4C composites at ambient and elevated temperatures, while the precipitates of nanoscale Al_3Sc and Al_3(Sc, Zr) in the composite matrix provides a predominate contribution to the composite strength, which is varied by tested temperatures. The Al_3Sc precipitates in Al–15vol.%B_4C–0.4wt.%Sc composite remain coarsening resistant at 250 °C, whereas the Al_3(Sc, Zr) precipitates in Al–15 vol.% B_4C–0.4 wt.% Sc–0.24 wt.% Zr are thermally stable at 300 °C during 2000 h of annealing. At higher annealing temperatures, 300 °C for the composite containing Sc and 350 °C for the composite containing Sc and Zr, both Al_3Sc and Al_3(Sc, Zr) precipitates become coarsening with prolonged annealing time. The yield strength of the two composites at ambient temperature decreases with increasing precipitate size, which can be explained by the classical precipitate shearing and Orowan bypass mechanisms. At elevated temperatures (250–350 °C), considerably lower yield stresses, which approximately are independent of precipitate coarsening, are observed compared to those at ambient temperature. It invokes a dislocation climb mechanism. A strengthening model based on the combination of dislocation climb and Orowan mechanisms is established. The predicted

yield strengths with the strengthening model at elevated temperatures are in good agreement with the experimental data.

In the second part, the mechanical properties and their thermal stability of the hot rolled Al–15 vol.% B_4C composite sheets with 0.4 wt.% Sc, and 0.4 wt.% Sc plus 0.24 wt.% Zr were investigated. The results demonstrate that under an appropriate post-rolling heat treatment, the hot-rolled sheets regained a significant precipitation hardening, due to the precipitation of fine nanoscale Al_3Sc and $Al_3(Sc,Zr)$ that uniformly distributed in aluminum matrix. The UTS at ambient temperature of the deformed composite sheets with Sc and Sc plus Zr can reach 197 MPa and 210 MPa, respectively. During 2000 h annealing at 300 ºC, the strengths at ambient temperature of both composites decreased slowly with increasing annealing time. However, the UTS and YS at 300 ºC of all deformed composite sheets remained almost unchanged and they were less sensible with annealing time and more tolerable for precipitate coarsening, showing an excellent long-term thermal stability of both composites at elevated temperature. The tensile fracture at ambient temperature of the Al–15 vol.% B_4C deformed composites with 0.4 wt.% Sc, and 0.4 wt.% Sc plus 0.24 wt.% Zr was dominated by the brittle B_4C particle fracture, while the interfacial decohesion of B_4C particles became the prominent characteristic of the fracture at 300 ºC.

In the third part, the focus is on the hot deformation behaviours and processing maps of Al–15 vol.% B_4C composites with and without Sc and Zr additions. The results show that the flow stress of the composites increases with the additions of Sc and Zr, attributing to the synthetic effect of dynamic precipitation and solute atoms. The additions of Sc and Zr moderately increase the activation energy for hot deformation of Al–B_4C composites. The constitutive equations of the three composites, Al–15 vol.% B_4C, Al–15 vol.% B_4C composite with 0.4 wt.% Sc, and 0.4 wt.% Sc plus 0.24 wt.% Zr, were established to describe the effect of the temperature and strain rate on hot deformation behaviors. Using the proposed constitutive equations, the predicted flow stresses on various deformation conditions are in good agreement with experimental data for all three composites. The processing maps of three composites were established to understand the hot workability of the composites. Two safe domains in the processing map were recommended for each composite, in which dynamic recovery and dynamic recrystallization were involved as softening mechanism. The additions of Sc and Zr limit the dynamic softening process, especially for dynamic recrystallization during hot deformation. The microstructure analysis reveals that the flow instability is attributed to the void formation, cracking and flow localization during hot deformation of the composites.

RÉSUMÉ

Cette thèse met l'accent sur les propriétés mécaniques et à l'usinage à chaud des alliages d'aluminium composites à matrice métallique à 15 vol.% de B_4C avec du scandium et du zirconium pour des applications à température élevée. Des études sur leurs propriétés mécaniques, leur stabilité thermique, leurs mécanismes de durcissement, leurs caractéristiques des microstructures, les traitements thermiques, les précipitations et les déformations à chaud ont été effectuées.

Les propriétés mécaniques et de stabilité thermique à long terme des composites, à températures ambiantes et élevées, ont été évaluées par des mesures de dureté et des essais de traction et de compression. Un microscope électronique à transmission, un microscope électronique à balayage et un microscope optique, équipé d'un système d'analyse d'images, ont été utilisés pour observer et analyser les précipitations de façon quantitative, la structure des grains et des sous-grains, les dislocations et les fractures sous tension des composites. Pour examiner la déformation à chaud et à l'usinage des composites, des essais de compression uniaxiale ont été effectués à des vitesses de déformation et à des températures de déformation variées en utilisant une unité de simulation thermomécanique Gleeble-3800.

Les résultats de cette thèse sont présentés en trois parties.

Dans la première partie, le scandium et le zirconium, comme éléments d'alliage, ont été introduits dans les composites Al–15vol.%-B_4C, pour examiner l'effet des précipités et des particules B_4C sur les propriétés mécaniques ainsi que leur stabilité thermique brutes de coulée à températures ambiante et élevée. Nous avons constaté que la présence de particules B_4C avec une dimension à l'échelle micrométrique a un effet de renforcement mécanique modéré, mais stable sur les composites Al–B_4C à températures ambiantes et élevées, tandis que les précipitations à l'échelle nanométrique, des composés Al_3Sc et Al_3(Sc, Zr) dans les composites, fournissent une contribution prédominante sur les propriétés de résistance mécanique des composites, qui varie selon les températures testées. Les précipitations d'Al_3Sc dans le composite Al–15 vol. % B_4C– 0.4 wt. % Sc demeurent grossièrement résistantes à 250 °C, alors que les précipitations Al_3(Sc, Zr) dans Al–15 vol. % B_4C–0.4 wt. % Sc–0.24 wt. % Zr sont stables thermiquement à 300 °C sur 2000 h de recuit. À de plus hautes températures de recuit, 300 °C pour les composites contenant Sc et 350 °C pour les composites contenant Sc et Zr, avec un temps de recuit prolongé, les deux précipitations Al_3Sc et Al_3(Sc, Zr) deviennent grossières. La limite d'élasticité des deux composites à température ambiante diminue avec la taille croissante des précipitations, qui peut être expliquée par les théories de cisaillement classiques des précipitations et les mécanismes de dérivation d'Orowan. À des températures élevées (250–350 °C), des limites de contraintes considérablement moindres, qui sont presque indépendantes de précipitations

grossières, sont observées comparées à celles à température ambiante. Cela montre donc un mécanisme de dislocation en escalade. Un modèle de renforcement a été établi sur la combinaison d'escalades de dislocations et le mécanisme d'Orowan. Les limites d'élasticité prévues avec le modèle de renforcement à températures élevées concordent bien avec les données expérimentales.

Dans la deuxième partie, nous avons fait l'étude des propriétés mécaniques et de la stabilité thermique des composites déformés à chaud Al–15 vol. % B_4C avec 0.4 wt. % Sc, et 0.4 wt. % Sc plus 0.24 wt. % Zr. Les résultats démontrent que sous un traitement thermique postlaminage adéquat, les plaques laminées à chaud regagnent un important durcissement par précipitation, à l'échelle nanométrique, des composés Al_3Sc et $Al_3(Sc,Zr)$, qui est répartie uniformément dans la matrice d'aluminium. Le UTS à température ambiante des feuilles composites déformées avec Sc et Sc-Zr peut atteindre 197 MPa et 210 MPa respectivement. Durant 2000 h de recuit à 300 °C, les résistances à température ambiante des deux composites diminuent lentement avec la croissance du temps de recuit. Toutefois, les UTS et YS à 300°C de toutes les feuilles composites déformées sont demeurés presque inchangés et ils étaient moins sensibles avec le temps de recuit et plus tolérables à la précipitation grossière, montrant une excellente stabilité thermique à long terme des deux composites à température élevée. La fracture sous tension à température ambiante des composites déformés Al–15 vol. % B_4C avec 0.4 wt. % Sc, et 0.4 wt. % Sc plus 0.24 wt. %

Zr a été dominée par la fracture fragile des particules B_4C, pendant que la décohésion interfaciale des particules B_4C est devenue la cause majeure de la fracture à 300 °C.

Dans la troisième partie, l'accent a été mis sur la déformation à chaud et les processus de traitements des composites Al–15 vol. % B_4C, avec et sans l'addition de scandium et de zirconium. Les résultats montrent que la contrainte de fluage des composites augmente avec les ajouts de Sc et Zr, attribué à l'effet synthétique de la précipitation dynamique et d'atomes en solution. Les ajouts de Sc et Zr augmentent modérément l'énergie d'activation pour la déformation à chaud des composites Al–B_4C. Les équations constitutives des trois composites, le composite Al–15 vol. % B_4C, Al–15 vol. % B_4C avec 0.4 wt. % Sc, et 0.4 wt. % Sc plus 0.24 wt. % Zr, ont été établies pour décrire l'effet de la température et la vitesse de déformation sur les comportements en déformation à chaud. En utilisant les équations constitutives proposées, la contrainte de fluage prévue sous les conditions variées de déformation concorde bien avec les données expérimentales pour les trois composites. Les processus de traitement a été établi pour les trois composites, en tenant compte du

revenu et de la recristallisation dynamique afin de comprendre les mécanismes d’adoucissement. Les ajouts de Sc et Zr limitent le procédé dynamique d'adoucissement, spécialement pour la recristallisation dynamique durant la déformation à chaud. L'analyse de la microstructure révèle que l'instabilité de l'écoulement est attribuée à la formation de vides, à la fissuration et à la localisation des écoulements durant la déformation à chaud des composites.

ACKNOWLEDGEMENTS

It is a pleasure to convey my sincere gratefulness to everyone who encouraged and supported me during my Ph.D. studies at University of Quebec at Chicoutimi (UQAC).

I would like to express my gratitude to my supervisor Dr. X. Grant Chen for his guidance and providing me the opportunity to study in Canada. He introduces me to a new, extremely interesting area, i.e. the high-temperature properties and hot deformation of Al–B_4C composites containing Sc and Zr. Also, I would like to express my deepest gratitude and thanks to my co-supervisor Dr. Zhan Zhang. He always inspired me to explore new possibilities and overcome difficulties. Additionally, Dr. Chen gave me all the necessary support in my convenient life. My Ph.D. graduate thesis is a challenge for me since I have no experience in modeling field and composite field. Dr. Mao, Dr. Zhang and Dr. Chen sheared their ideas. The discussions were always very interesting and useful.

Secondly, I would like to thank my relative group members in CURAL and start the list with Dr. J. Lai, she is the one with whom I took my first steps in this project. Thank my office mate Dr. C. Shi to provide me suggestion on studying hot deformation behavior. Also I would like to thank the friends in CURAL as Émélie Brideau, Martin Bouchard, Dany Racine, Pier-Luc Prive, Dr. Emad Elgallad, Dr. Ying Huang, Lei Pan, Zhen Li and Jiawei Xiong. All above I had the chance to live with, we shared summer and winter during these years.

Most importantly, I could not possibly have finished this work without encouragement and support from my parents and my beloved girlfriend Yuanyuan Wang for giving me their endless love.

Finally, thank China Scholarship Council and Dr. Chen to provide me an opportunity and award the scholarship to support me study in Canada.

TABLE OF CONTENTS

PUBLICATIONS

PEER-REVIEWED JOURNAL ARTICLES

1. J. Qin, Z. Zhang, X-Grant Chen. "Mechanical Properties and Strengthening Mechanisms of Al-15 Pct B_4C Composites with Sc and Zr at Elevated Temperatures." *Metallurgical and Materials Transactions A*, 2016, online published, DOI: 10.1007/s11661-016-3606-4.
2. J. Qin, Z. Zhang, X-Grant Chen. Mechanical properties and thermal stability of hot rolled Al-15%B_4C composites containing Sc and Zr, 2015, Prepared for Submission.
3. J. Qin, Z. Zhang, X-Grant Chen. Hot deformation and processing maps of Al–15%B_4C composites with Sc and Zr, 2015, Prepared for Submission.
4. J. Qin, Z. Zhang, X-Grant Chen. Effect of hot deformation on microstructure and mechanical properties of Al–B_4C composite containing Sc. Materials Science Forum, 2014, Vols. 794-796, pp. 821-826.

POSTERS

5. J. Qin, Z. Zhang, X.-G. Chen. Hot deformation behavior and workability characteristics of Al–B_4C composites containing Sc and Zr. REGAL student's day, Chicoutimi, Canada, Nov. 2015, (awarded **CHAIRE CIMTAL** prize).
6. J. Qin, Z. Zhang, X.-G. Chen. Model for yield strength in precipitation strengthened Al–B_4C composites at elevated temperature. REGAL student's day, Sherbrook, Canada, Nov. 2014.
7. J. Qin, Z. Zhang, X.-G. Chen. Thermal-stability of Al–B_4C composites alloyed with Sc and Zr at elevated temperatures. REGAL student's day, Montreal, Canada, Oct. 2013, (awarded **ALCOA** prize).
8. J. Qin, Z. Zhang, X.-G. Chen. On the mechanical properties of Al–B_4C alloyed with

Sc and Zr at elevated temperatures. REGAL student's day, Trois-Riviere, Canada, Nov. 2012.

9. J. Qin, Z. Zhang, X.-G. Chen. Effect of heat treatment on microstructure and mechanical property of rolled Al–B_4C composites with Sc and Zr additions. Conference of Metallurgists (COM 2011), Montreal, Canada, Oct. 2011.

LIST OF SYMBOL

a : Coarsening rate constant

a_m : Lattice parameters of matrix

a_p : Lattice parameters of precipitate

A : Material constant

α : Material parameter

α' : Material constant

$\boldsymbol{b}$: Burgers vector

β: Material parameter

d : Average grain size

δ: Lattice mismatch

ε : Constrained strain

$\dot{\boldsymbol{\varepsilon}}$: Strain rate

E : Interaction energy for a unit length of an edge dislocation

f : Precipitate volume fraction

F : Force acts on the dislocation

G : Dissipator content

G_m : Shear modulus of matrix alloy

G_p : Shear modulus of precipitates

η : Dissipation efficiency

h : Distance between the dislocation glide plane and precipitate center

HV : Vickers' hardness

θ : Angle between origin plane and dislocation climb plane

J : Dissipator co-content

J_{max} : Maximum dissipator co-content

Γ : Modulus mismatch parameter

γ_{apb}: antiphase boundary energy

k : exponent

k_m : Poisson parameter of matrix

k_p : Poisson parameter of precipitate

λ : Inter precipitate spacing

M : Mean matrix orientation factor

m : Strain rate sensitivity of flow stress

χ : Dimensionless constants.

n : Material constant

n_1 : Material constant

ξ : Continuum instability criterion

v_m : Poisson's ratio of matrix

v_p : Poisson's ratio of precipitate

σ : Flow stress

σ_{Al+B_4C} : Strength contributed by the unalloyed Al-15%B_4C composite

σ_t : overall strength

$\Delta\sigma_i$: Characteristic strength increment

$\Delta\sigma_p$: Precipitate strength increments

$\Delta\sigma_C$: Dislocation climb strengthening

$\Delta\sigma_{LMC}$: Strength increments of lattice mismatch modulus mismatch

$\Delta\sigma_{MMC}$: Strength increments of modulus mismatch

$\Delta\sigma_O$: Contribution of Orowan mechanism

$\Delta\sigma_s$: Contribution of shearing mechanism

$\Delta\sigma_{MMS}$: Contributions of modulus mismatch

$\Delta\sigma_{LMS}$: Contributions of lattice mismatch

P : Power absorbed by work piece

Q : hot deformation activation energy

R : Universal gas constant

r : Precipitate radius

$\overline{r}_0$: Initial mean precipitate radius

$\overline{r}_t$: Mean precipitate radius at a specific time

$\bar{r}$: Mean precipitate radius

τ: Critical resolved shear stress

t : Time

T : Absolute temperature

T_m : Melting temperature

x : dislocation position factor

x_0 : unraveling distance

y : dislocation position factor

z : dislocation position factor

z_0 : Height of the dislocation segment climbed above its glide plane

Z : Zener-Holloman parameter

LIST OF FIGURES

LIST OF TABLES

CHAPTER 1

INTRODUCTION

Chapter 1

Introduction

1.1 Background

Al−B_4C metal matrix composites have been widely used as neutron absorber materials in the transport and storage of spent nuclear fuels in the nuclear industry because of the special capacity of B_4C on excellent neutron absorption [1, 2]. In service, the composites can be exposed at elevated temperatures (250−350 °C) for different lengths of time owing to the heat generation and accumulation by absorbing thermal neutrons from the spent fuels [1, 3]. To improve the overall performance of the neutron absorber materials, it is desirable to maximize the operating temperature and thermal stability of the materials at such high temperature. As the matrix of metal matrix composites, most commercial precipitation-strengthened 2xxx, 6xxx and 7xxx aluminum alloys are limited to be used

below 200 °C. The mechanical properties of these matrices can be seriously deteriorated at higher temperature because of the rapid coarsening of their precipitates (overaging effect) [4]. For precipitation-strengthened aluminum alloys, the Al-Sc alloy is a rare exception, which can be used up to 300 °C because it can form nanoscale coherent Al_3Sc precipitates with a low coarsening rate [5]. Above this temperature, the Al_3Sc precipitates may coarsen and lose coherency, which results in the degradation of mechanical properties of the materials [6, 7]. It was reported that Zr could partially substitute Sc to form $Al_3(Sc1\text{-}xZrx)$ precipitates with better coarsening resistance [8, 9], which improves the thermal stability of the precipitates up to 350 °C [9] and increases the strength and recrystallization resistance [10-12].

The presence of B_4C particles can provide an additional strengthening to Al matrix not only at ambient but also at elevated temperatures. The composites of Al–B_4C were thermally stable and the mechanical properties of those composites remained unchanged at 300 °C after a long holding period [13]. However, the contribution of B_4C particles to the

composite strength was limited due to the large B_4C particle size (in micrometer scale). So, it is reasonable to introduce scandium and zirconium into Al–B_4C composites to further improve their strengths at elevated temperatures. The microstructure and mechanical properties of Al−B_4C composites containing Sc and Zr additions have been studied [7, 13-15]. It had been [7] demonstrated that the yield strength at ambient temperature of the Al−B_4C composites with Sc had not significantly changed after annealing at 250°C up to 2000 h, whereas the strengths at ambient temperature remained stable after annealing at 300 °C up to 2000 h for the Al−B_4C composite strengthened by Al_3(Sc, Zr) precipitates. However, the mechanical properties and their thermal stability of the composites with Sc and Zr at elevated temperatures have not been reported yet.

Al metal matrix composites (MMCs) are frequently deformed through rolling, extrusion and forging processes. The deformation processes can cause a series microstructure changes that will affect the final mechanical properties [14]. Only a few works reported the hot deformation behavior of Al−B_4C composites [16, 17]. Moreover, it

was reported that the Al_3Sc precipitation hardening in deformed materials would be difficult because of severe limits on the solution treatment [18]. The public information concerning the Al_3Sc precipitation in deformed aluminum metal matrix composites is very scarce.

Base on the information mentioned above, the mechanical properties and their thermal stability at elevated temperature should be investigated for the Al–B_4C composites with and without Sc and Zr. The effect of hot deformation on Al_3Sc and Al_3(Sc, Zr) precipitation has to be clarified. Moreover, a good understanding of the hot deformation behaviours and work ability of the composites is necessary to obtain optimum mechanical properties and manufacture process.

1.2 Objectives

This project aims to study the mechanical properties and their thermal stability as well as hot workability of Al–B_4C composites containing scandium and zirconium for

elevated temperature applications. To gain the achievements, following objectives are proposed:

Investigate the mechanical properties and their thermal stability of as cast Al–B_4C composite containing Sc and Zr at elevated temperatures:

- Evaluate the mechanical properties of as cast Al–B_4C composites with and without Sc and Zr at various temperatures;
- Evaluate the evolution of the thermal stability of the composites at ambient and elevated temperature during long term annealing;
- Examine the evolution of microstructure, including grain size, precipitate radius, precipitate distribution, precipitate volume fracture and its coarsening rate during long term annealing at elevated temperature;
- Clarify the strengthening mechanisms at ambient and elevated temperature of the composites.

Investigate the mechanical properties and their thermal stability of hot-rolled Al–B_4C composites containing Sc and Zr:

- Study the effect of hot deformation on Al_3Sc and Al_3(Sc, Zr) precipitation strengthening in Al–B_4C composites containing Sc and Zr;
- Study post-deformation heat treatments to obtain precipitation strengthening in the composites;
- Evaluate the influence of test temperatures on mechanical properties of the hot rolled composites;
- Evaluate the thermal stability of mechanical properties during long-term annealing;
- Investigate the evolution of microstructure including grain structure, precipitates, and the tensile fracture during the long term annealing.

Investigate hot deformation and processing maps of Al–B_4C composites with and without Sc and Zr:

- Study the flow stress behavior and microstructure evolution of the composites during hot deformation at various temperatures and strain rates;
- Establish constitutive equations of the three composites to describe the effect of the temperature and strain rate on hot deformation behavior;
- Determine the activation energies of the composites and study the effect of Sc and Zr on the activation energies;
- Establish the processing maps for the composites and study the effect of Sc and Zr on the evolution of the maps.

1.3 References

[1] Chen X-G. Application of Al-B_4C Metal Matrix Composites in the Nuclear Industry for Neutron Absorber Materials. In: Nikhil Gupta WHH, editor. Solidification Processing of Metal Matrix Composites: Rohatgi Honorary Symposium. USA: TMS, November 2006. p.343.

[2] Bonnet G, Rohr V, Chen X-G, Bernier J-L, Chiocca R, Issard H. Use of Alcan's Al-B_4C metal matrix composites as neutron absorber material in TN International's transportation and storage casks. Packaging, Transport, Storage & Security of Radioactive Material 2009;20:98.

[3] Deng JX, Sun JL. Microstructure and mechanical properties of hot-pressed B4C/TiC/Mo ceramic composites. Ceramics International 2009;35:771.

[4] Kaufman JG. Properties of aluminum alloys: tensile, creep, and fatigue data at high and low temperatures. USA, 1999.

[5] Hyland RW. Homogeneous nucleation kinetics of Al3Sc in a dilute Al-Sc alloy. Metallurgical Transactions A 1992;23:1947.

[6] Royset J, Ryum N. Scandium in aluminium alloys. International Materials Reviews 2005;50:19.

[7] Lai J, Zhang Z, Chen XG. The thermal stability of mechanical properties of Al-B4C composites alloyed with Sc and Zr at elevated temperatures. Materials Science and Engineering a-Structural Materials Properties Microstructure and Processing 2012;532:462.

[8] Fuller CB, Seldman DN. Temporal evolution of the nanostructure of Al(Sc,Zr) alloys: Part II-coarsening of $Al_3(Sc_{1-x}Zr_x)$ precipitates. Acta Materialia 2005;53:5415.

[9] Elagin VIZ, V V; Pavlenko, S G; Rostova, T D Influence of Zirconium Additions on Aging of Aluminum--Scandium Alloys. (Translation) Physics of Metals and Metallography 1985;60:88.

[10] Fuller CB, Seidman DN, Dunand DC. Mechanical properties of Al(Sc,Zr) alloys at ambient and elevated temperatures. Acta Materialia 2003;51:4803.

[11] Riddle YW, Sanders TH. A study of coarsening, recrystallization, and morphology of microstructure in Al-Sc-(Zr)-(Mg) alloys. METALLURGICAL AND MATERIALS TRANSACTIONS A 2004;35A:341.

[12] Belov NA, Alabin AN, Eskin DG, Istomin-Kastrovskii VV. Optimization of hardening of Al-Zr-Sc cast alloys. Journal of Materials Science 2006;41:5890.

[13] Lai J, Zhang Z, Chen X. Effect of Sc and Zr alloying on microstructure and precipitation evolution of as cast Al-B4C metal matrix composites. Materials Science and Technology 2012;28:1276.

[14] Chen XG, St-Georges L, Roux M. Mechanical Behavior of High Boron Content Al-B4C Metal Matrix Composites at Elevated Temperatures. Materials Science Forum, vol. 706: Trans Tech Publ, 2012. p.631.

[15] Lai J, Zhang Z, Chen XG. Precipitation strengthening of Al–B4C metal matrix composites alloyed with Sc and Zr. Journal of Alloys and Compounds 2013;552:227.

[16] Gangolu S, Rao A, Prabhu N, Deshmukh V, Kashyap B. Hot Workability and Flow Characteristics of Aluminum-5 wt.% B4C Composite. Journal of materials engineering and performance 2014;23:1366.

[17] Gale WF, Totemeier TC. Smithells metals reference book: Butterworth-Heinemann, 2003.

[18] L.S. Toropova DGE, M.L. Kharakterova and T.V. Dobatkina. Advanced aluminum alloys containing scandium: structure and properties Amsterdam, The Netherlands: Gordon and Breach Science, 1998.

CHAPTER 2

LITERATURE REVIEW

Chapter 2

Literature review

In recent years, metal matrix composites (MMCs) with light metal matrixes gain successful applications in aerospace industry, traffic engineering, especially in automotive and transport technology. Commonly ceramic particles, fibers or carbon fibers, are used for metal reinforcement. Particle reinforced light metals gain popularization in industry with their potential as low cost, high modulus and strength, high wear resistance, and easily fabricated material.

2.1 Matrix alloys

Al–based alloys used for metal matrix composites (MMCs) have several remarkable characteristics that make them attractive for the development of high strength and high temperature materials. The works on the improvement of aluminum alloy strength at

elevated temperature have been carried out for decades [1-4]. A remarkable improvement of mechanical properties at elevated temperatures is on the addition of 0.1−1 wt.% Sc in Al alloys [5]. The Al−Sc alloys are strengthened by the formation of Al_3Sc precipitates with finer radius and high volume fraction [6]. After decades developments, Drits [7-9], Elagin, Zakharov, Dunand, Marquis, Seidman and Fuller *et al.* [10-21], made a great progressing on the research of Al−Sc alloys in the fields such as strengthening effects, thermal stability, creep behaviours, composition optimization, strengthening mechanisms etc. Dramatic strengthening effect (350 MPa) is reported in an annealing Al–0.41 wt.% ingot [22]. However, the medium diffusivity of scandium in aluminum limits its strengthening effect [23]. Based on this fact, ternary or quaternary systems were developed [24-26].

2.1.1 Al–Sc binary alloys

2.1.1.1 Phase diagram

The Al–Sc binary phase diagram at Al rich corner is shown in Fig. 2.1. There is a eutectic reaction at aluminum rich side of the phase diagram:

$$\text{Liq.} = \alpha\ (\text{Al}) + \text{Al}_3\text{Sc} \qquad \text{Eq. 2. 1}$$

It is reported that the eutectic temperature varies between 655 and 659 °C [7, 27-31]. The eutectic composition is approx. 0.6 wt. % [7, 29] and the solid solubility of Sc in Al at the eutectic temperature is approx. 0.35 wt. % [27].

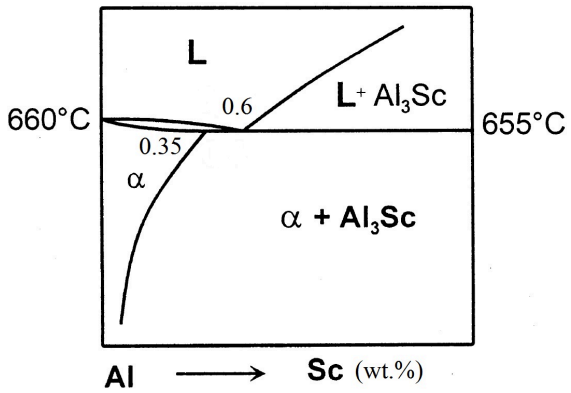

Fig. 2. 1. Phase diagram for Al–Sc system at Al rich corner [32].

2.1.1.2 Al_3Sc phase

Lattice structure of Al_3Sc was reported to be of $L1_2$ type [33]. The structure can be described as ordered FCC, and atomic arrangement of Al_3Sc phase is shown in Fig. 2.2. Rechkin *et al.* had identified Al_3Sc phase as cubic with lattice parameter 4.10 Å [34]. This particular atomic arrangement of Al_3Sc phase shows misfit with Al matrix of 1.34 % at 24°C and 1.05 % at 300 °C [24, 35]. The orientation relationship between Al_3Sc and the matrix is suggested to be (110) Al_3Sc // (100) matrix, [010] Al_3Sc // [010] matrix [36]. The Al_3Sc precipitate with spherical shape is most frequently reported [11, 14, 16-18, 20, 21, 23, 37-49].

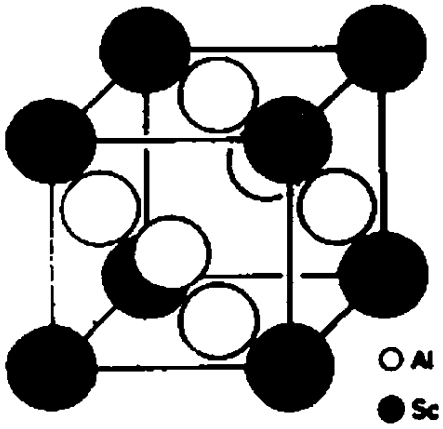

Fig. 2. 2. Atomic arrangement of Al_3Sc phase [39].

The shear modulus of Al_3Sc was reported to be 68 and 63 GPa at room temperature and 300°C, respectively [50]. The Poisson's ratio of Al_3Sc is 0.2 [50]. The temperature dependence of the Yong's modulus of Al_3Sc is given by $\partial E / \partial T$ =-26 MPa/K [51]. When a matrix dislocation shears an ordered precipitate and creates an antiphase boundary (APB) on the slip plane of the precipitate phase. γ_{apb} is APB energy per unit area on the slip plane represents the force per unit length opposing the motion of the dislocation as it penetrates the particle, and $\gamma_{apb} \approx 0.5 J/m^2$ [19, 42, 52-56]. The activation energy for diffusion of Sc in Al are determined to be 176±9 kJ/mol [57]. The thermal expansion of Al_3Sc has been measured [58] and based on the differences in thermal expansion between Al [59] and Al_3Sc, the misfit as a function of temperature has been calculated [58]. This calculation is reproduced by Royset *et al.* and shown in Fig. 2.3 by the solid line. Contribution from vacancies on thermal expansion of Al at elevated temperatures had been taken into account as represented by the dotted line [60].

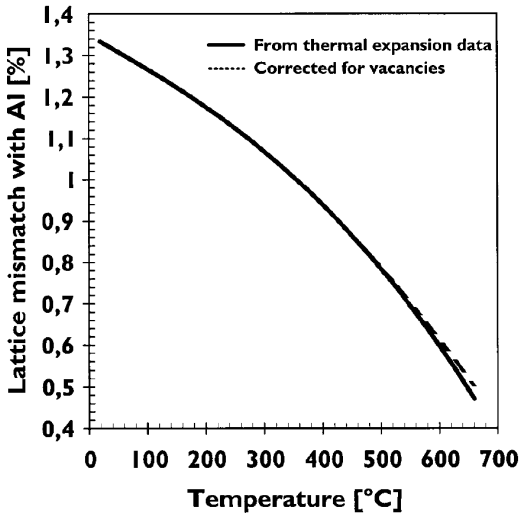

Fig. 2. 3. Lattice mismatch between Al and Al_3Sc as a function of temperature: solid line represents calculation based on linear thermal expansion of the two phases; dotted line represents correction for vacancies in Al lattice [32].

The coherency loss of Al_3Sc precipitates will not only increased its coarsening rate, but also will reduce their pinning effects on the migration of dislocations and migrating grain boundaries. S. Iwamura *et al.* investigate the correlation between the coarsening behaviour and coherency of the Al_3Sc particles in the Al–0.2 wt. % Sc alloy based on TEM observations and the calculation using numerical model [61]. The critical radius for coherent/semi-coherent transition of the Al_3Sc precipitates was determined as 15 nm. In the

range from 15 nm to 40 nm, coherent and semi-coherent coexist and the coarsening is delayed [61].

The relationship between average radius of the Al_3Sc precipitates, in coherent and semi-coherent, and annealing time obeys the Lifshitz–Slyozov–Wagner (LSW) theory [62-64]. It is shown as:

$$r^3 = at \qquad \text{Eq. 2. 2}$$

where r is average precipitate radius, a is coarsening rate and t is annealing time. C. Watanabe *et al.* investigated the coarsening kinetics of the Al_3Sc precipitates in an Al–0.28 wt. % Sc alloy aged at 400 °C (673 K), 425 °C (698 K), and 450 °C (723 K) and measured both of the coarsening rate of precipitates and the depletion rate of the supersaturated solid solution [57]. The coarsening behaviors of Al_3Sc in Al–0.28 wt. % Sc alloy annealed at 400 °C (673 K), 425 °C (698 K), and 450 °C (723 K) are presented in Fig. 2.4, where mean precipitate radius is plotted as a function of aging time.

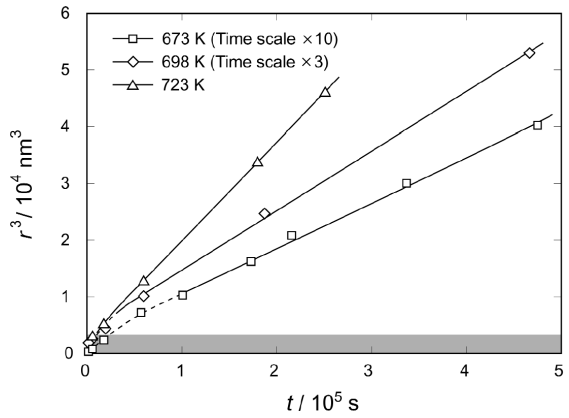

Fig. 2. 4. Coarsening plot of Al_3Sc precipitates in an Al–0.28 wt. % Sc alloy aged at 673, 698, and 723 K. The shaded area indicates the coherent stage (<15 nm) [57].

Experimental values of coarsening rates at different aging temperature were determined from the slopes from Fig. 2.4 and these values are listed in table 2.1 [57]. The coarsening rate shows an acceleration coarsening kinetics with increasing temperature.

Table 2. 1. Values of the Coarsening Rate of Al_3Sc in a Al–0.28wt% Sc alloy [57].

Temperature (K)	Coarsening rate (m^3/s)
673	$(8.75 \pm 0.16) \times 10^{-30}$
698	$(4.11 \pm 0.16) \times 10^{-29}$
723	$(1.77 \pm 0.12) \times 10^{-28}$

The precipitate radius distribution also follows the predictions of LSW theory as shown in Fig. 2.5 [18].

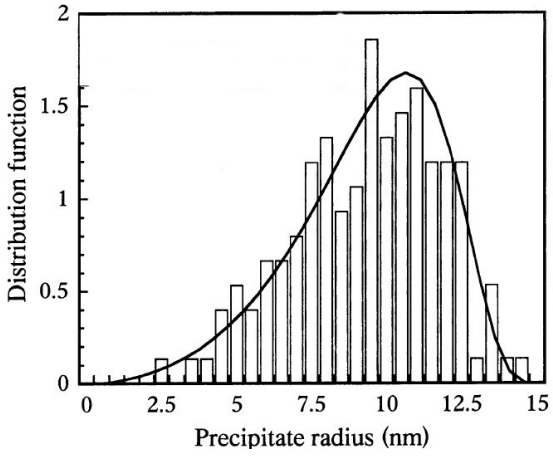

Fig. 2. 5. Precipitate size distributions for the Al-0.3 wt. % Sc alloy aged at 400 °C for 10 hours. The theoretical LSW distribution function is shown as a solid line for comparison [18].

2.1.1.3 Mechanical properties of Al–Sc binary alloys

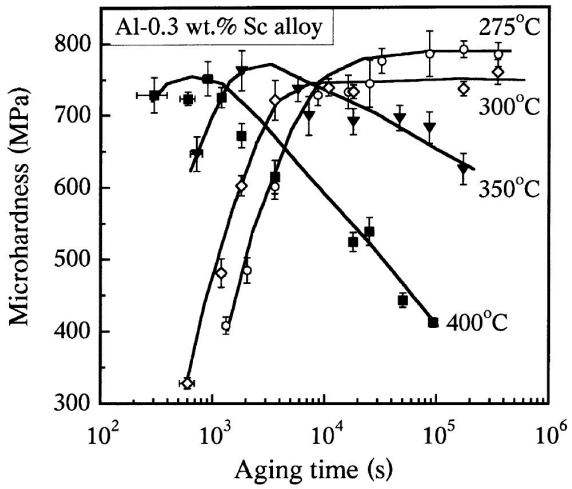

Fig. 2. 6. Vickers micro–hardness versus aging time for an Al–0.3 wt. % Sc alloy as a function of aging temperatures (275, 300, 350 and 400 °C) [18].

It has been noted that Al_3Sc precipitates can give a significant enhancement in strength of the alloy. The hardness curves reflect the precipitation hardening occurring during aging in the Al–0.3 wt. % Sc alloy as a function of annealing time at various temperatures is shown in Fig. 2.6 [18].

The dependence of hardness on scandium concentration was measured by aging Al–0.1, 0.2 and 0.3 wt. % Sc alloys at 300 °C as shown in Fig. 2.7. As the scandium concentration increases, the incubation time decreases and the value of peak hardness increases [18].

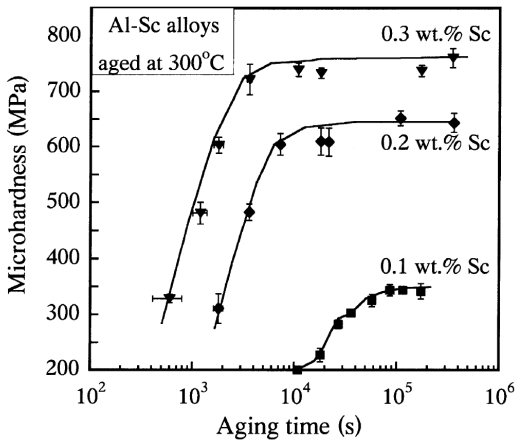

Fig. 2. 7. Vickers micro–hardness versus aging time at 300 °C as a function of Sc concentration (0.1, 0.2 and 0.3 wt.%) [18].

D.N. Seidman *et al*. [18] presented the contribution of Al_3Sc precipitates in the hardness as a function of precipitate radius [65] as shown in Fig. 2.8. The direct comparison become possible for the Al−0.3%Sc alloy hardness with different aging temperature and time because the volume fraction of Al_3Sc precipitates is approximately constant. Fig. 2.8 shows a maximum in hardness increase for radii between 1.5 and 2.0 nm. This result suggests a transition from a shearing mechanism to an Orowan dislocation bypass mechanism.

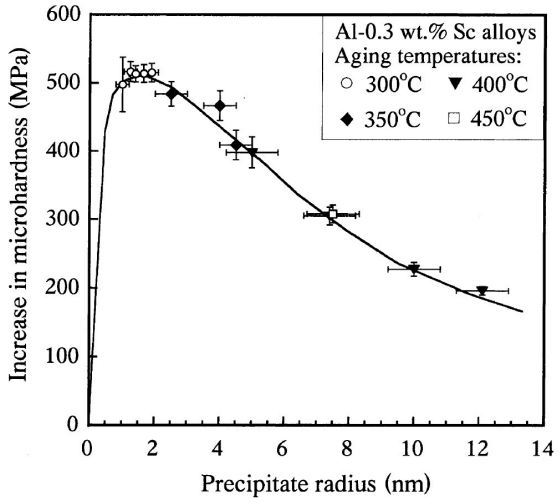

Fig. 2. 8. Increase in ambient temperature microhardness versus precipitate radius for an Al–0.3 wt.% Sc alloy aged at different temperatures [18].

Although the Al–Sc binary alloys have a dramatic improvement in strengthening and thermal stable at elevated temperature, these binary alloys was still limited for application owing to the following two reasons, i.e., the strengthening capability of Al–Sc alloys decreases after long term annealing at elevated temperature which is caused by coarsening of Al_3Sc precipitate and the high cost of scandium [66, 67].

2.1.2 Al–Sc–Zr ternary alloys

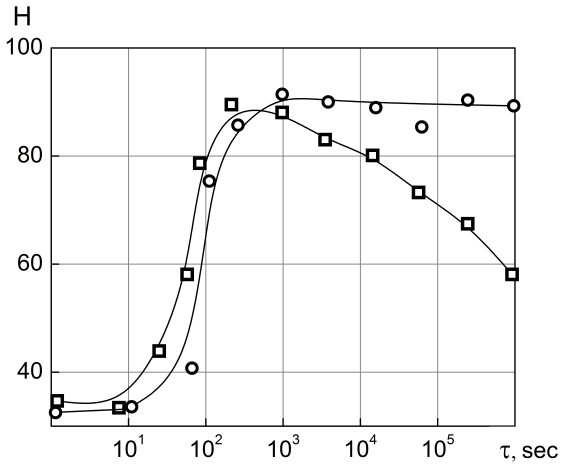

Fig. 2. 9. Microhardness of Al–0.4 wt. % Sc alloy and Al–0.4 wt. % Sc–0.15 wt. % Zr alloy (ingots) vs. annealing time at 350°C [68].

A zirconium addition to binary Al–Sc alloys decreases coarsening ability of the Al_3Sc precipitate while prolonging annealing time at elevated temperatures [68]. Fig. 2.9 presents

two curves showing micro-hardness of Al–0.4 wt. % Sc alloy ingot and a similar alloy alloyed with 0.15 wt. % Zr versus annealing time. The zirconium addition results in a dramatic stabilizing effect, while the strengthening effect is not changed [68].

2.1.2.1 $Al_3(ScZr)$ phase

Elagin *et al.* [69] first suggested that Zr could substitute for Sc in Al_3Sc precipitates formed $Al_3(Sc_{1-x}Zr_x)$ precipitates. The chemical composition of $Al_3(Sc_{1-x}Zr_x)$ precipitates has been investigated using analytical TEM [70, 71] and a combination of TEM and Atom probe tomography (APT) [72]. All of the three papers indicated that Zr was present within $Al_3(Sc_{1-x}Zr_x)$ precipitates, in agreement with Ref. [73, 74], and that Zr was detected at the $\alpha-Al/Al_3(Sc_{1-x}Zr_x)$ interfaces [71]. Fig. 2.10b shows the integrated number of counts under the Sc K_α and Zr K_α peaks along the line shown in Fig. 2.10a. It is clearly apparent that the composition is not uniform within the particle. Both Sc and Zr are found on the rim of the particle. In the core of the particle, the Zr content drops sharply to almost zero, while the Sc

content is roughly constant. Hence, the coherent $Al_3(ScZr)$ precipitates were found to consist of a core containing Al and Sc surrounded by a Zr-rich shell.

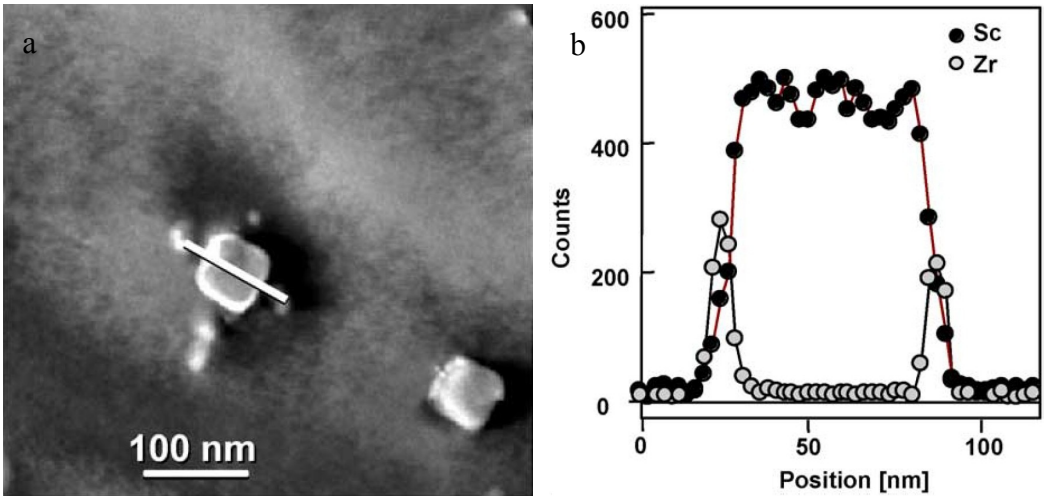

Fig. 2. 10. (a) Annular dark field image of a precipitate in ternary Al–Sc–Zr. The image was obtained close to the 001 zone axis. (b) Composition profile along the line indicated in (A) showing the number of EDS counts under the Sc K_α and Zr K_α peaks as a function of position [72].

The calculated diffusivity of Sc and Zr [75-77] demonstrates that Zr diffuses four orders of magnitude slower than Sc in Al at 300 °C [23, 78]. Thus, this phenomenon leads to the increased resistance to coarsening of Al_3ScZr precipitates in these ternary alloys.

2.1.2.2 Lattice mismatch of $Al_3(Sc,Zr)$ precipitate

Zr was reported could decrease lattice parameter and resulting in the decrease of the lattice parameter misfit [24]. The reduced lattice parameter mismatch as observed by Harada Y. *et al.* [58] decreases the rate of Ostwald ripening of precipitates, thus benefits the thermal stability of materials [23]. Lattice mismatch of $Al_3(Sc, Zr)$ with the α-Al matrix decreases from 1.05% to 0.78% at 300 °C. The coefficient of thermal expansions (CTEs) for binary Al_3Sc and ternary $Al_3(Sc, Zr)$ were measured as $(16 \pm 1)\times10^{-6} K^{-1}$ [58].

2.1.2.3 Coarsening of $Al_3(Sc, Zr)$

C. B. Fuller *et al.* indicate that diffusion-limited coarsening is operative during annealing of $Al_3(Sc, Zr)$ precipitate, which is supported by the agreement of the activation energy values [79]. The coarsening behavior of Al−0.09 at. % Sc−0.047 at. % Zr and Al−0.14 at. % Sc−0.012 at. % Zr alloys at aging temperatures between 300, 350, or 375 °C follow LSW theory and their coarsening rates are displayed in table 2.2 [79].

Table 2. 2. Experimentally coarsening rate constants of Al_3ScZr precipitates in different alloys at 300−375 °C [79].

Alloy (at.%)	Coarsening rate (m^3/s)		
	300 °C	350 °C	375 °C
Al-0.06 Sc-0.005 Zr	$(5.13 \pm 2.07) \times 10^{-33}$	$(1.5 \pm 0.22) \times 10^{-30}$	$(8.27 \pm 4.15) \times 10^{-33}$
Al-0.07 Sc-0.019 Zr	$(1.86 \pm 0.55) \times 10^{-33}$	$(1.62 \pm 0.24) \times 10^{-31}$	$(4.12 \pm 1.72) \times 10^{-30}$
Al-0.09 Sc-0.047 Zr	$(4.29 \pm 2.58) \times 10^{-34}$	$(6.75 \pm 0.73) \times 10^{-32}$	$(9.1 \pm 1.5) \times 10^{-31}$
Al-0.14 Sc-0.012 Zr	$(3.92 \pm 3.37) \times 10^{-34}$	$(9.2 \pm 9.1) \times 10^{-34}$	$(2.61 \pm 0.79) \times 10^{-32}$

As anticipated, the coarsening rate for each alloy increases with increasing temperature. The effect of volume fraction on the coarsening kinetics of Al−Sc−Zr alloys is examined [79]. The coarsening rate is decreasing with the precipitate volume fraction increases, as it would be an increase in diffusion and elastic interactions among precipitates associated with increasing precipitate volume fraction [79].

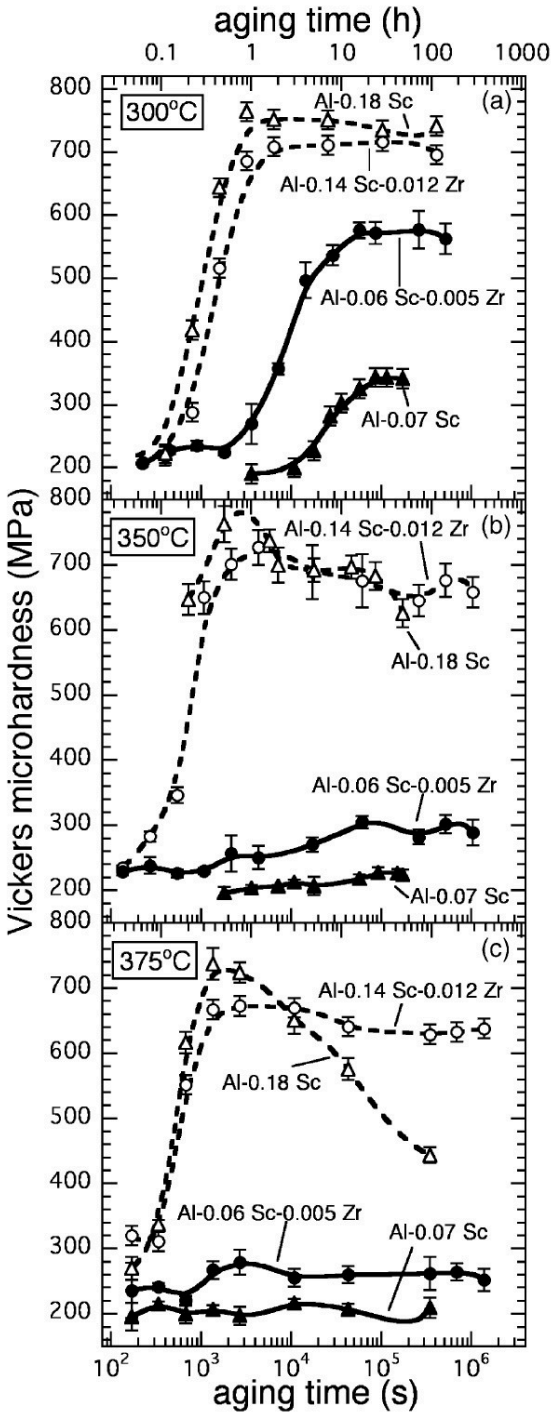

Fig. 2. 11. Vickers microhardness (MPa) of Al–Sc and Al-Sc-Zr alloys vs. aging time at: (a) 300 °C, (b) 350 °C, and (c) 375 °C [42].

2.1.2.4 Mechanical properties of Al–Sc–Zr ternary alloys

Fig. 2.11 demonstrates the variation in Vickers hardness as a function of aging temperature and time for Al–Sc–Zr alloys [42], and their equivalent Al–Sc alloys [18], respectively. At all temperatures the peak hardness of Al–Sc–Zr alloys are higher than that of corresponding Al–Sc alloys. Zirconium additions also increase the duration of peak hardness when alloys are aged at 350 and 375 °C.

2.2 Al–B_4C composites

B_4C has lower specific gravity of 2.51 g/cm^3 (less than that of Al, 2.7 g/cm^3), as well as high impact and wear resistance, high melting point, good resistance to chemical agents, and high capacity for neutron absorption [80-82], making itself a promising candidate for the reinforcement in an Al based MMCs [83].

2.2.1 Interface reactions in Al–B_4C composites

The interface in composites refers to a bounding surface between reinforcement and matrix, where there is variation in chemical composition, elastic modulus and coefficient of thermal expansion. The interface has a very important influence on the properties of all composites, as it not only has a large surface area per unit volume but also is related to interface reactions between reinforcement and matrix. An idea interface should promote wetting and bond the reinforcement and the matrix to a desirable degree, protect the reinforcement and allow load transfer from matrix to rigid reinforcement [84-87].

In 1989, Halverson [88] studied reaction thermodynamics of Al–B_4C and found reaction products consist of Al_3BC and AlB_2 in a temperature range from 800 to 1400 °C. Fig. 2.12a shows the isothermal section of the Al–B–C phase diagram at 750 °C, calculated using the Thermo-Calc software database. The phase diagrams indicate that B_4C particles were thermodynamically unstable in liquid aluminum and would continue to decompose as long as they contact liquid aluminum [89].

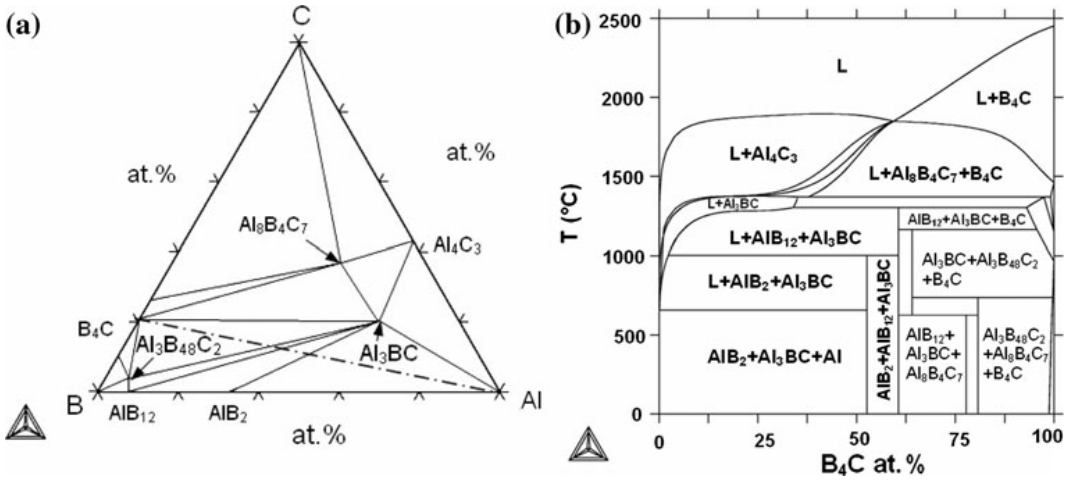

Fig. 2. 12. Calculated phase diagrams: (a) Al–B–C isothermal section at 750 °C, (b) Al–B_4C isopleths phase diagram [89].

Hence, the interfacial reaction in the Al–B_4C system in this temperature range was expressed as [90-92]:

$$9Al+2B_4C = 2Al_3BC+3AlB_2 \quad \text{Eq. 2. 3}$$

Fig. 2.13 shows the optical microstructure of Al–12 vol. % B_4C holding at 750 °C. Using SEM and TEM, it was identified that the yellow phase was AlB_2 and the gray phase was Al_3BC [89]. The formation of Al_3BC and AlB_2 at the interface led to a decomposition of B_4C, which confirmed the fact that these two compounds are unable to prevent the attack of liquid aluminum on B_4C [90, 91, 93, 94].

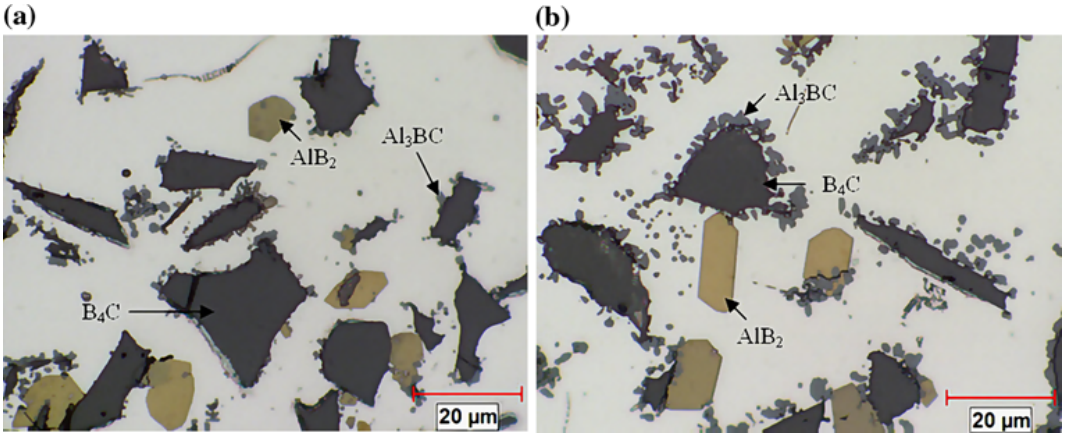

Fig. 2. 13. Optical microstructure of Al–12%B_4C held at 750 °C for (a) 5 min and (b) 120 min. [89].

In order to enhance the wettability of B_4C particles and limit its decomposition, Ti is introduced to in the Al–B_4C system [89]. When Ti is introduced in the Al–B_4C system at 730–750 °C, it would induce the generation of two phases (Al_3BC and TiB_2) in a relatively short time [89]. The interfacial reaction is shown as [94]:

$$6Al+3Ti+2B_4C=2Al_3BC+3TiB_2 \quad \text{Eq. 2. 4}$$

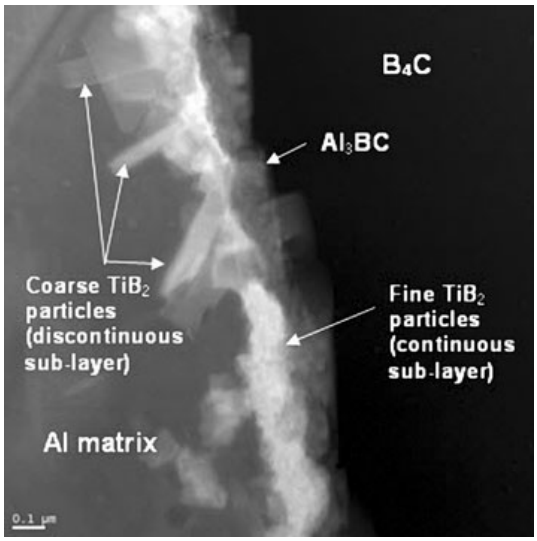

Fig. 2. 14. STEM dark field micrograph of the 1.0 % Ti composite, showing the TiB_2 layers in the interface region in great details [89].

An observation (Fig. 2.14) by TEM shown that the B_4C particle was firstly covered by Al_3BC reaction layer then followed by a TiB_2 layer. TiB_2 and Al_3BC build up a protection layer surrounding B_4C particle acted as a diffusion barrier [89]. Hence, with addition of Ti, Al–B_4C composites can be processed with low-cost stir casting routes [89, 95-98].

J. Lai *et al.* investigated the effect of Sc, Zr and Ti on the interfacial reactions of the Al–B_4C system [96]. They found in the B_4C/Al–Zr system, the interfacial reaction products

consists of Al_3BC and ZrB_2. Similar to the B_4C/Al–Ti system, the interfacial reaction in the B_4C/Al–Zr alloy can be express as:

$$6Al + 3Zr + 2B_4C = 2Al_3BC + 3ZrB_2 \qquad \text{Eq. 2. 5}$$

In the B_4C/Al–Sc system, three interfacial reaction products, Al_3BC, ScB_2 and Al_3ScC_3 were identified coexist in the interfacial microstructure. The interfacial reaction of this system can be expressed as [96]:

$$9Al + 10Sc + 5B_4C = 2Al_3BC + Al_3ScC_3 + 9ScB_2 \quad \text{Eq. 2. 6}$$

In the B_4C/Al–Sc–Zr–Ti system, there are two main interfacial reaction products, which are Al_3BC and TiB_2, and some Sc and Zr are also detected in this layer. The outside crystal layer is confirmed to be in the majority of TiB_2 type crystals that also contain traces of Sc and Zr. Hence, the TiB_2 layer can not only limit the decomposition of B_4C particle but also can reduce the consumption of strengthening elements Sc and Zr at the interface [96].

2.2.2 Mechanical properties of Al–B_4C composites containing Sc and Zr

J. Lai *et al.* studied the precipitation behaviour of Al–B_4C composites alloyed with Sc and Zr [95]. Fig. 2.15 shows the microhardness of three Al–B_4C composites with nominal composition 0.29 wt. % Sc, 0.40 wt. % Sc and 0.58 wt. % Sc as a function of aging time at temperatures of 300, 350, 400 and 450 °C. The aging curves of the Al–B_4C composites containing Sc have similar tendency experienced under-aging, peak aging and over-aging stages. The hardness values of three composites increase with the increasing of Sc concentration at all aging temperatures. With increasing of aging temperature, the microhardness peak comes earlier, and with prolonging of aging time, the microhardness dramatically decrease which is in the over-aging stage.

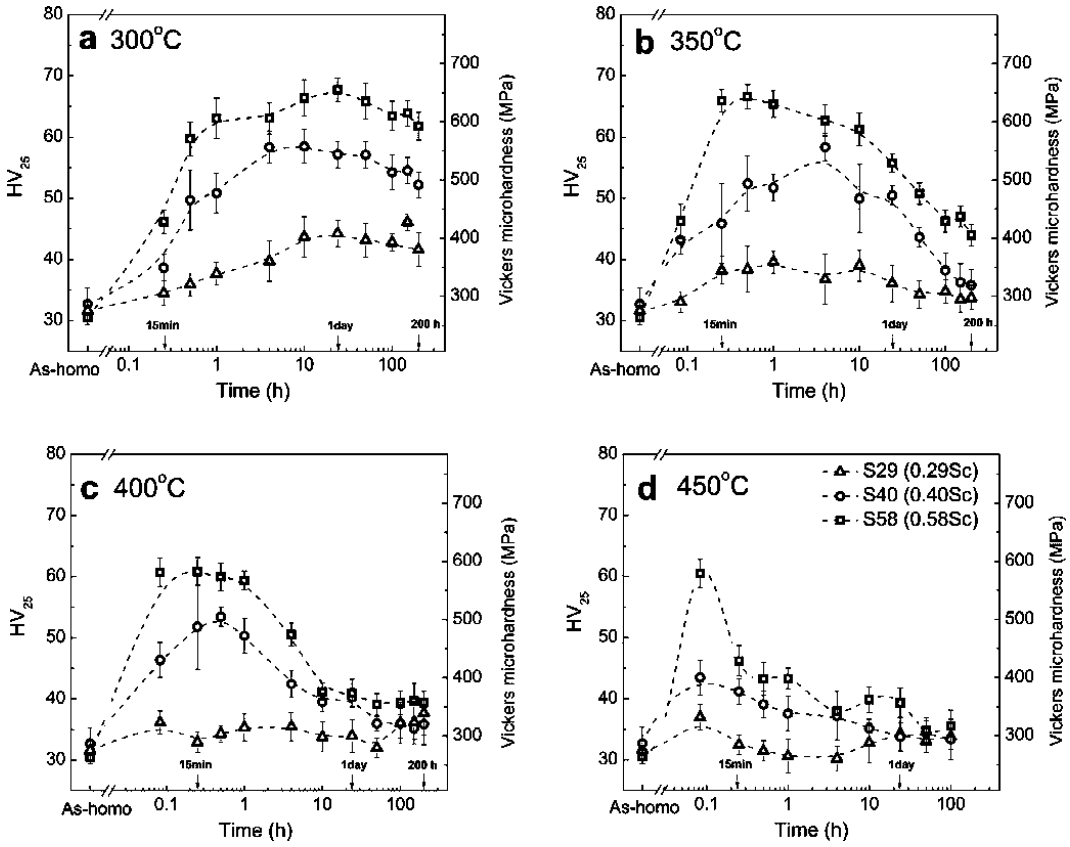

Fig. 2. 15. Vickers microhardness vs. aging time at: (a) 300, (b) 350, (c) 400 and (d) 450 °C for three Al–Sc composites [95].

Fig. 2.16 shows the microhardness of three Al–B_4C composites with nominal composition 0.29 wt. % Sc + 0.24 wt. % Zr, 0.40 wt. % Sc + 0.24 wt. % Zr and 0.58 wt. % Sc + 0.24 wt. % Zr aging at temperatures of 300, 350, 400 and 450 °C. The microhardness of these composites increase associated with increasing of matrix composition. These composites containing Sc and Zr exhibit similar tendency of the aging curves to the

composites containing Sc. The aging curves of the composites with Zr addition have an improvement in microhardness and can maintain the hardness for a period. Compared with Al–B_4C composites with Sc, addition of Zr not only increases the strengthening effect but also improves their thermal stability.

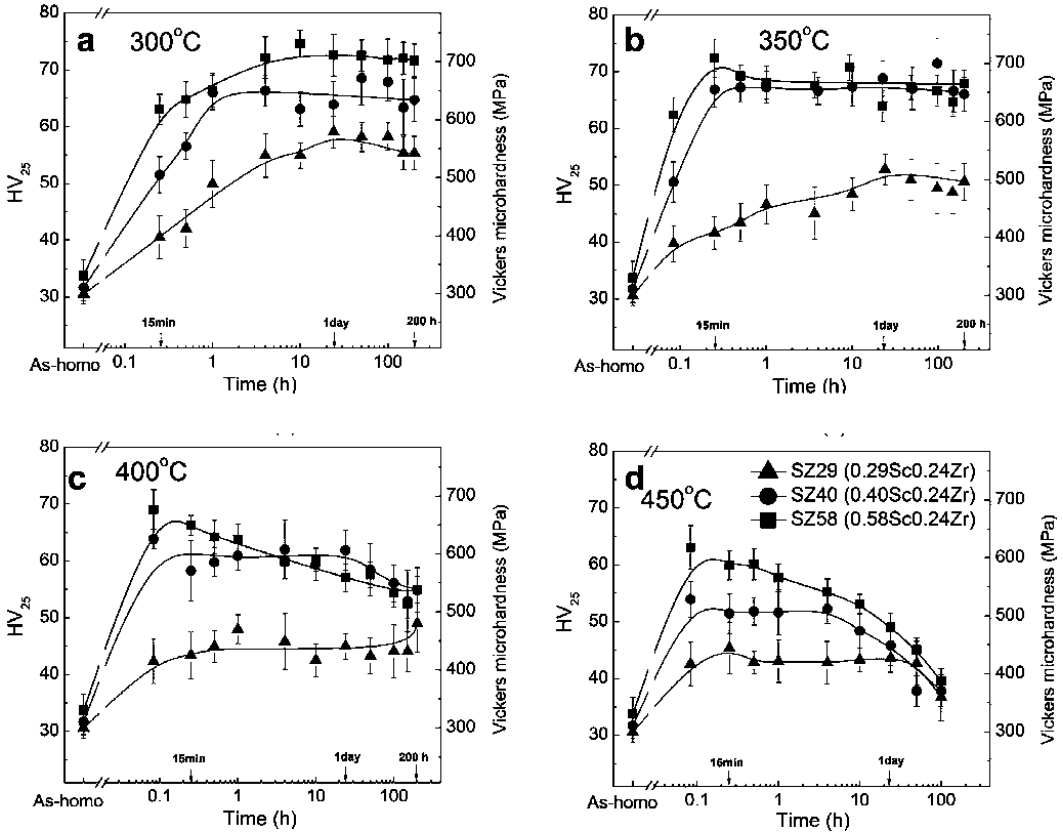

Fig. 2. 16. Vickers microhardness vs. aging time at: (a) 300, (b) 350, (c) 400 and (d) 450 °C for three Al–Sc–Zr composites [95].

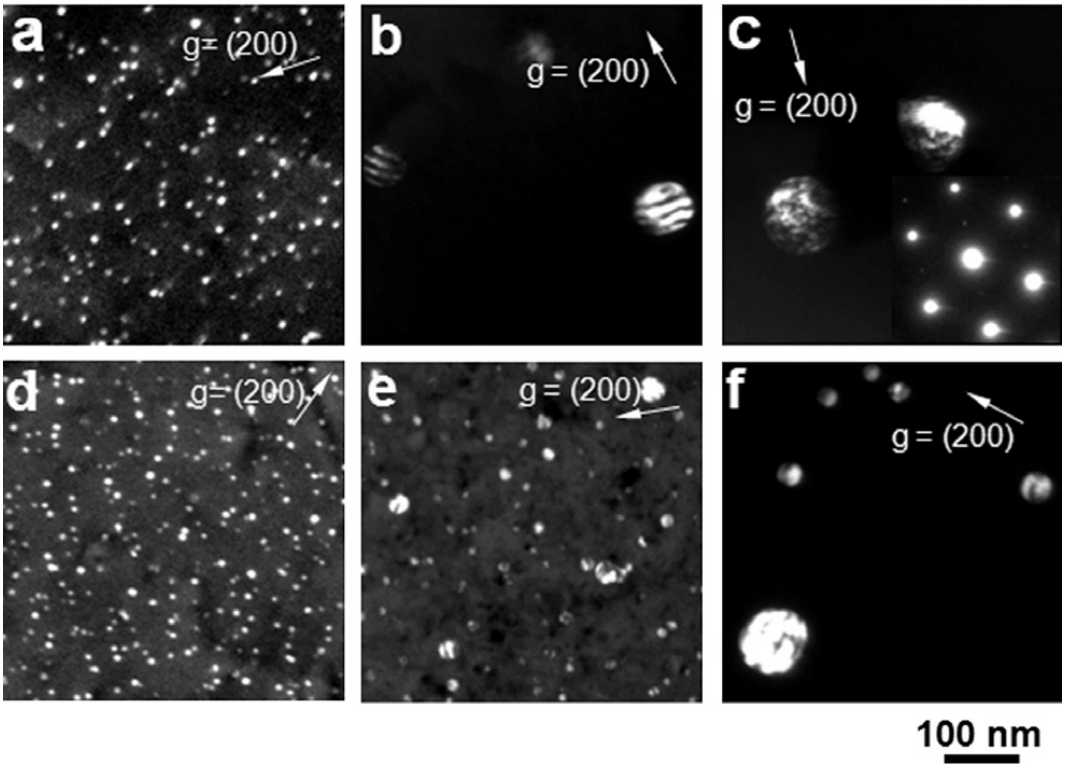

Fig. 2. 17. Dark-Field TEM images shows precipitates in the matrix of the composites with 0.58 wt. % Sc (a)–(c) and 0.58 wt. % Sc + 0.24 wt.% Zr (d)–(f) during aging at 450 °C for 5min, 10 hours and 100 hours exposure times [95].

TEM was employed to study the aging hardening effect and precipitation behavior of the composites containing Sc and Zr [95]. Fig. 2.17 shows representative TEM images that demonstrate the precipitate evolution of the composites with 0.58 wt. % Sc and 0.58 wt. % Sc + 0.24 wt. % Zr for 5min, 10 hours and 100 hours aging. Uniform distribute coherent precipitates of Al_3Sc and $Al_3(ScZr)$, with $L1_2$ structure, were observed in Al–B_4C

composites. $Al_3(Sc, Zr)$ precipitate exhibits a better coarsening resistance than Al_3Sc precipitate. Therefore, Al–B_4C composites which are alloyed with Sc and Zr are strengthened by both of B_4C particles and precipitates.

2.2.3 Thermal stability of Al–B_4C composites

2.2.3.1 Thermal stability of 1100–B_4C composites

X. G. Chen *et al.* investigated the mechanical properties of the 1100–B_4C composites annealing at elevated temperature for long period [99]. Fig. 2.18 shows the mechanical properties of 1100–25 vol. % B_4C composite tested at 25 °C as a function of holding time at 300 °C. The thermal stability of mechanical properties of the composites is related to the microstructural evolution during the annealing. During annealing at 300 °C for long term, B_4C particles are stable and matrix grain size barely change. Hence, the mechanical properties remain unchanged after a long term annealing at 300 °C for up to 1000 hours.

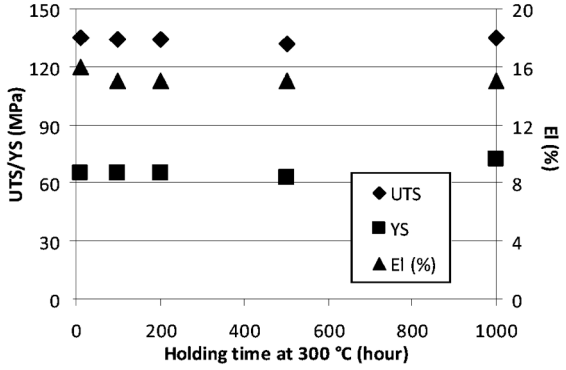

Fig. 2. 18. Effect of holding time at 300 °C on mechanical properties of 1100–25 vol. % B_4C composite tested at 25 °C [99].

2.2.3.2 Thermal stability of Al–B_4C composites containing Sc and Zr

To further improve the mechanical properties of the Al–B_4C composites, Sc and Zr were introduced into this system [95]. J. Lai *et al.* [97] investigated the Thermal stability of Al–B_4C composites containing 0.4 wt. % Sc (S40) and 0.4 wt.% Sc + 0.24 wt.% Zr (SZ40). The composites containing Sc and Zr were heat treated to T6 condition then assess their thermal stability of the mechanical properties.

Fig. 2.19 demonstrates the evolution of the mechanical properties of S40 and SZ40 composites during long term annealing. The S40 and SZ40 composite show good resistance of softening during 2000 hours annealing at 250 and 300 °C, respectively. The mechanical

properties of S40 and SZ40 decreases remarkably while the annealing temperature increases to 300 and 350 °C, respectively. During annealing at 350 °C, the grain size of SZ40 composite coarse from 43 to 51 μm [97], which according to Hall-Petch equation can only cause a 0.3 MPa reduction in strength. Therefore, decreases in mechanical properties of S40 and SZ40 composites are only cause by the variation of precipitates.

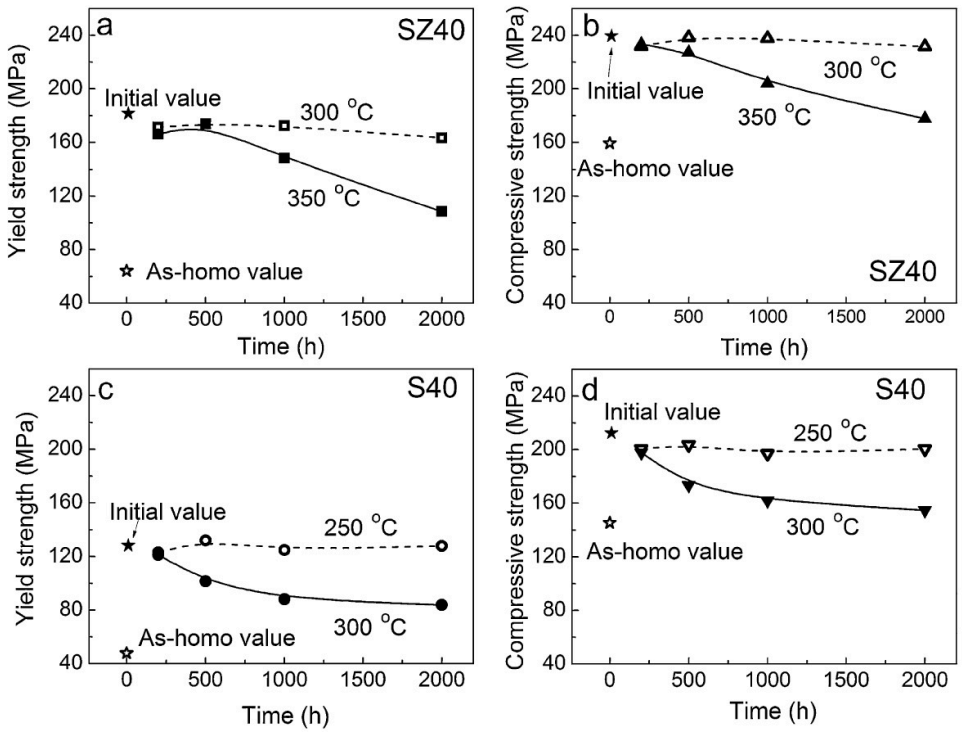

Fig. 2. 19. Yield and compressive strengths vs. annealing time, (a) the yield strength of SZ40, (b) the compressive strength of SZ40, (c) the yield strength of S40 and (d) the compressive strength of S40 [97].

The aluminum grain size, and the B_4C particles and their interfaces have no remarkable effect on the variation of the mechanical properties of the composites during annealing [99]. The softening of the composites is related to coarsening of the precipitates. The average precipitate radii of precipitates as a function of annealing treatment are measured by J. Lai *et al.* and listed in Table 2.3 [97].

Table 2. 3. Average precipitate radii of precipitates as a function of annealing treatment in the SZ40 composite [97].

Annealing treatment	Coarsening rate (m^3/s)
350 °C×10 hours (T6)	2.6 ± 0.7
350 °C×10 hours+300 °C×2000 hours	2.4 ± 1.1
350 °C×10 hours+350 °C×1000 hours	3.9 ± 2.0
350 °C×10 hours+350 °C×1000 hours	5.1 ± 4.7

2.3 Strengthening mechanisms of Al MMCs

The strengthening of Al–B_4C composites is mainly contributed by Al matrix and B_4C ceramic reinforcements. However, the strengthening mechanisms of matrix and B_4C particles are greatly different. Moreover, strengthening mechanisms can be affected by test temperature.

2.3.1 Strengthening mechanisms of 1100–B_4C composites

The presence of B_4C particles can provide an additional strengthening to Al matrix at both ambient and elevated temperatures [99]. The strengthening mechanisms of reinforcements in MMCs can be divided into two categories, direct and indirect strengthening. The former refers to the load transfer from the weak matrix, across the matrix/reinforcement interface, to the higher stiffness reinforcement [100, 101]. And the latter involves dislocations accumulation around the reinforce particles due to the thermal expansion mismatch [85, 102, 103]. Fig. 2.20a shows the tensile properties of 1100–25 vol. % B_4C composite as a function of the temperature on as-annealed condition. For

comparison, tensile properties of AA1100 on anneal condition alloy are also presented in Fig. 2.20b.

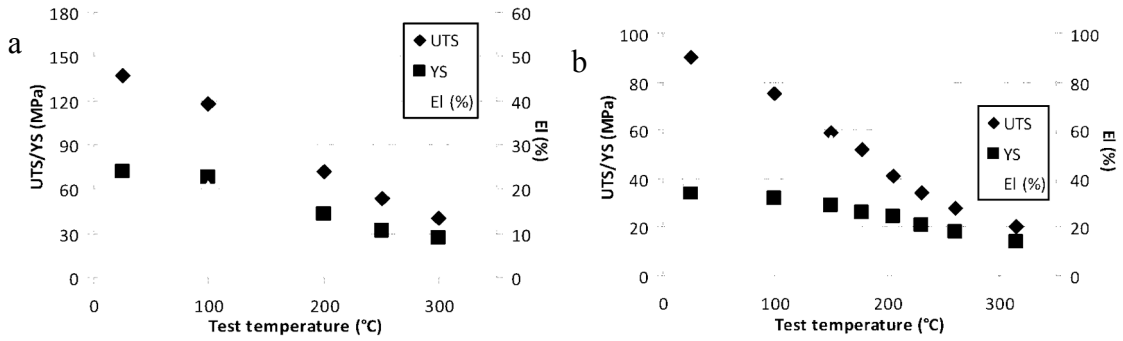

Fig. 2. 20. Effect of the temperature on mechanical properties of Al–25 vol. % B_4C composite on as-rolled condition (a) [99] and AA1100–O [104].

Yield strength and Ultimate strength of both materials decrease associated with increasing of test temperature. Increasing of test temperature refers to the shear modulus decreasing, multi slip system activation and dislocation climbing, which will lead to the softening of matrix. The presence of 25% volume fraction B_4C particles in the AA1100 matrix significantly increases the strength and reduces the elongation. At ambient temperature, the contribution to yield strength from the presence of B_4C particles was 38

MPa, while at 300 °C it was 13 MPa [99]. However, due to large particle size of B_4C particles (in the micrometer scale), their contribution to the composite strength was limited.

2.3.2 Strengthening mechanisms of Al alloys

Besides the ceramic particles, matrix alloys have a contribution to the strength of Al MMCs. There are four major strengthening mechanisms, *i.e.*, work hardening, solid solution strengthening, grain boundary strengthening, and precipitation strengthening. In the present study, the Al–B_4C MMCs are designed to service with high strength at elevated temperature. In the case of deformed Al–Sc and Al–Sc–Zr alloys, the supersaturated matrix will decompose, moreover, grain growing and recovery or recrystallization will reduce the work hardening effect at elevated temperature. Hence, precipitation strengthening from Al_3Sc and Al_3ScZr precipitates with low coarsening rate is expected to be a suitable strengthening mechanism.

2.3.2.1 Precipitation strengthening mechanisms at ambient temperature

Precipitate particles can impede the motion of dislocations through a variety of interaction mechanisms, including chemical strengthening, stacking fault strengthening, modulus hardening, coherency strengthening and order strengthening.

Shearing and Orowan bypass are two main mechanisms to explain the dislocation bypass the precipitates in Al–Sc and Al–Sc–Zr alloys [18, 42]. When the coherent precipitates are small, the strength is controlled by dislocation shearing while the precipitate radius is over the critical size Orowan bypass is operative. For this shearing mechanism, the increase in strengthening comes from three contributions, modulus hardening, coherency strengthening and order strengthening. For a given precipitate radius, the shearing stress is taken as the higher of two contributions: order strengthening and the sum of coherency and modulus hardening [18].

Shearing mechanism refers to:

1. Modulus hardening occurs when the shear moduli of the matrix and precipitate phases are different. The greatest interaction forces occurs when the dislocation has entered the precipitate are used to estimate the maximum increment in yield strength [64].
2. The coherency strengthening of alloys also know as lattice mismatch strengthening, which is caused by coherent precipitates due to the interaction between the stress fields of the precipitates and the dislocation.
3. Order strengthening is operative when a matrix dislocation shears an ordered precipitate and creates an antiphase boundary (APB) on the slip plane of the precipitate phase. Order strengthening gains its effect from the ordered precipitates, which have a crystal structure of the type $L1_2$. Dislocations typically travel in pairs to restore perfect order in the precipitate [64].

All of mentioned above mechanisms lead to increase in strength associated with the increasing of precipitates radii. With coarsening of precipitates, eventually a critical radius

is reached which precipitates are incoherent and no longer can be cut through by dislocation. The possible mechanisms of dislocation move over a precipitate include bowing, climb and cross slip [105, 106]. Orowan proposed the following strengthening mechanism: a dislocation loop appears around each particle when a dislocation bypasses precipitates [107]. This mechanism usually is operative for precipitates with larger sizes [18, 95]. To performance further deformation, additional stress is needed to overcome the back stress from the dislocation loops and leads to rapid strain hardening to the matrix [107-111].

2.3.2.2 Precipitation strengthening mechanism at elevated temperature

The presence of hard particles can improve the mechanical behavior of metallic materials at elevated temperature in different ways. It's widely accepted that at elevated temperatures with lower strain rates precipitates are climbed over by dislocations, no matter the precipitate can be shared or not. There are three kinds of models describe for dislocation climb over particles. The first one, local climb, which presumes that the climbing dislocation segment profiles the dispersoid, and the dislocation between the dispersoids

remains in its glide plane [112, 113], as shows in Fig. 2.21a [114]. The second one, general climb model in which the dislocation is allowed to “unravel”, i.e. to reduce, under the action of its line tension, the high curvature at the point where it meets the dispersoid [115], as shows in Fig. 2.21b [113].

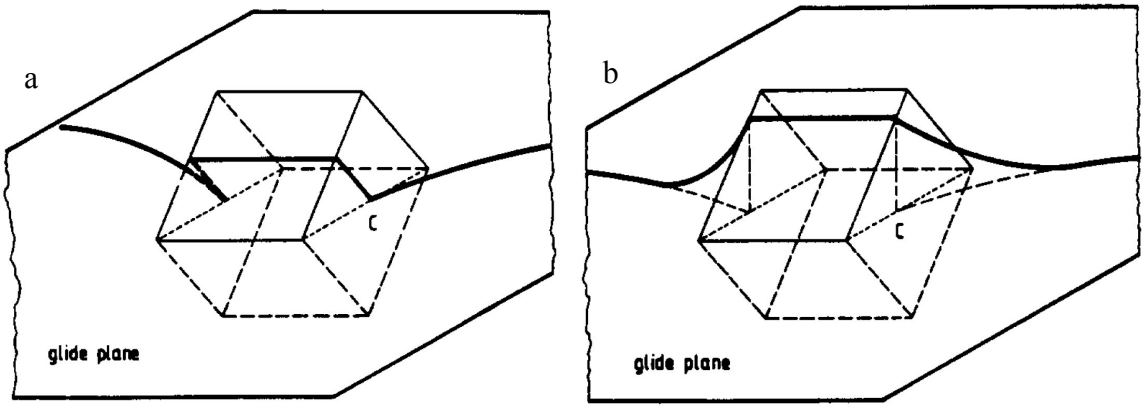

Fig. 2. 21. Schematic profile of a dislocation climbing over a cube-shaped particle, (a) according to “local” climb, with a sharp dislocation bend at C [114] and (b) according to “general” climb, where the high curvature at C is relaxed by “unravelling” [114].

The third one, a cylindrical particle of diameter and height equal to two times or its radius is employed to replace the cubic shape in the original general climb model [19]. The cylindrical shape particle model is an approximation of the spherical shape particle, as latter

is too complex to be introduced in general climb model. The glide plane of the dislocation intercepts the particle at height *h* above its center; the height of the dislocation segment, above its glide plane upon climb over the particle is z_0 and the unraveling distance is x_0, as shows in Fig. 2.22 [19]. In most precipitation hardening alloys, the precipitate is stiffer than the matrix, so the dislocation is repelled by the particles. The repulsion stress is the sum of the lattice and modulus mismatches hardening effect [55]. There is no simple solution of interaction energy exists for spherical particles, the solution derived by Dundurs et *al.* [116] for an infinitely long cylindrical particle interacting with an straight edge dislocation is used to describe the modulus mismatch effect.

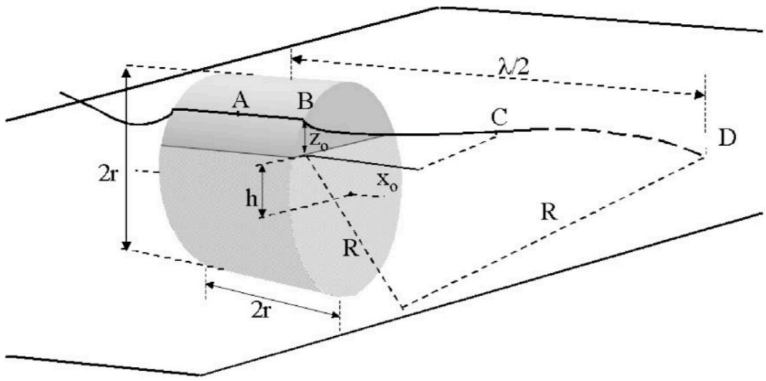

Fig. 2. 22. Geometry of general climb model, showing an edge dislocation with segment CD in the glide plane and segment AC climbing over a particle [19].

Most dislocation climb behaviours happen during creep test at elevated temperature. In the creep behaviour there exits a threshold stress is that matrix dislocations require some minimum amount of energy through the applied stress to bypass the second-phase precipitates [117]. Four possible mechanisms have been considered to explain the presence of threshold stresses in precipitation strengthening alloys [118]: (a) precipitate shearing; (b) Orowan dislocation looping; (c) dislocations climbing over precipitates; and (d) dislocation detachment from precipitates. The dislocation detachment mechanism can be ignored, as it is not active for coherent precipitates [119]. Marquis *et al.* [18] employed general climb with elastic interaction model predicted the normalized threshold stress of Al–Sc alloys at 300 °C, (threshold stress/Orowan stress), as a function of different mean precipitate radii as shown in Fig. 2.23. The threshold is caused by repulsive elastic interaction between the

matrix dislocations and the coherent precipitates. The threshold stress increases associated with increasing of mean precipitate radius.

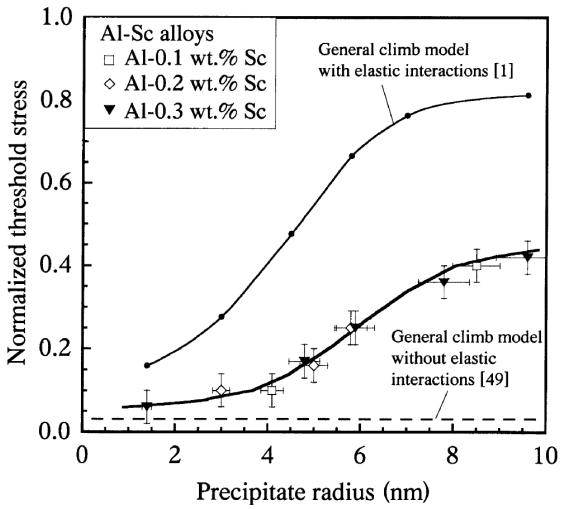

Fig. 2. 23. Normalized creep threshold stress with respect to Orowan stress at 300 °C as a function of precipitate radius for ternary Al–Sc alloys [18].

2.4 Hot deformation behavior and workability

The MMCs applied in industry, would be hot deformed at high temperature. For the deformation processing of Al–B_4C composites may refers to rolling, forging or extrusion. Hot deformation can be investigated and characterized through flow stress, which depends on deformation temperature, strain rate and strain [120-122]. Hence, to characteristic hot

deformation behavior, the examination of flow curves at a wide range of strain rates and deformation temperatures are necessary. For Al alloys, hot deformation can be considered to consist of two stages, the initial stage under control of work hardening in which flow stress increasing rapidly and the steady state in which work hardening mechanism is equilibrium with dynamic softening mechanisms. The dynamic softening mechanisms are the dynamic recovery (DRV) and dynamic recrystallization (DRX) processes which are active base on the rearrangement of dislocations associated with the increasing of strain [123].

Many investigations found that dynamic precipitation (DPN) occurred during hot deformation in 2×××, 6××× and 7××× series Al alloys [124-130]. The precipitation and following coarsening can increase the flow stress level, affect the flow curve shape and cause a softening behaviour [131]. The main softening mechanism of a precipitation strengthened Al–Cu–Mg alloy was reported transformed from dynamic recovery (DRV) to dynamic recrystallization (DRX) [132]. The precipitates formed during hot deformation

were reported that could restrain DRX level and increased the hot deformation energy [124]. It is reported that Sc and Zr can reduce grain size and increase recrystallization resistance by forming $L1_2$ structure precipitates [9, 133-136]. The fine precipitates of Al_3Sc can inhibit the migration of grain boundaries, sub-grain boundaries and dislocation movement, thereby, restrain the recrystallization effect and therefore result in a high work hardening stress [133-135, 137-142]. As shown in Fig. 2.24 is the microstructure of Al–Mg–Sc alloy deformed to 22 %, primarily consists of grains and sub-grains. Al_3Sc precipitates are observed to be quite effective in pinning those subgrain boundaries [138].

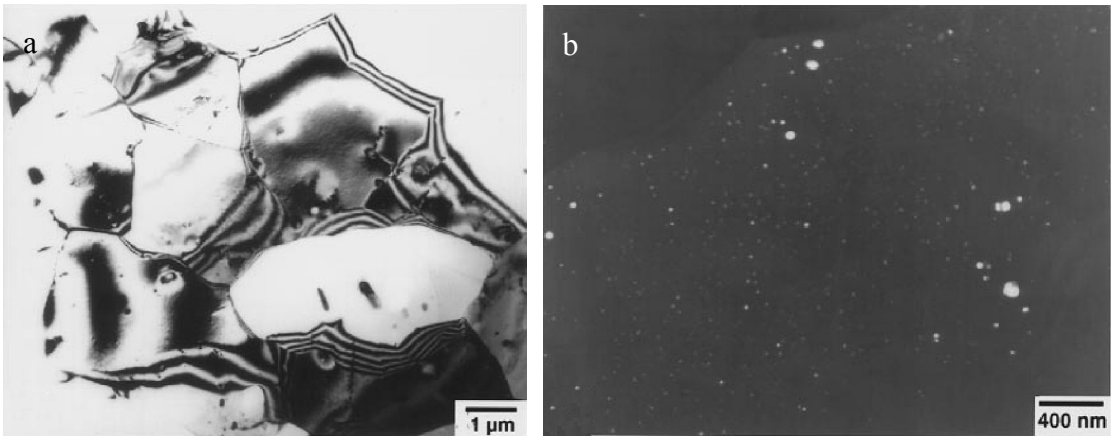

Fig. 2. 24. (a) Microstructure of Al-6Mg-0.3Sc sample deformed to 22% at 475 °C and at a strain rate of 1.4×10^{-2} s^{-1} and (b) significant amounts of fine Al_3Sc precipitates begin to appear[138].

The hot deformation behaviours of Al MMCs also can be influenced by enforcement particles in the form of enforcement particle cracking [143], interface decohesion [144], void formation [145], thermal residual stress caused by coefficient of thermal expansion (CTE) mismatch [146], flow localization [147] and deformation incompatibility between matrix and enforcement particles [148]. Hot deformation behaviour of Al MMCs is complex and greatly affected by deformation temperature and strain rate [120, 121]. It had been reported that the enforcement particles with greater volume fraction and finer size in Al MMCs will benefit the flow stress [149, 150].

2.4.1 Constitutive equations

Constitutive equations are developed to demonstrate the hot deformation behaviors and to describe the relationship among strain rate, deformation temperature and flow stress [120]. In hot working, the hyperbolic sin law can be used for a large range of strain rate and stress levels.

$$\dot{\varepsilon} = A\left[\sinh(\alpha\sigma)\right]^{n} \exp\left(-Q/RT\right) \quad \text{Eq. 2. 7}$$

Where *A, n,* and α are material constants, $\dot{\varepsilon}$ is strain rate, σ is flow stress (always take the peak stress of flow curve), R=8.31 J·mol^{-1}K^{-1} is universal gas constant and T is absolute temperature (K). The Q, hot deformation activation energy, is an important physical parameter represents the difficulty level in hot deformation. The activation energy for pure Al is about 140−156 kJ/mol [151-153]. The activation energy Q for Al has been found varies with composition, microstructure and range of T and $\dot{\varepsilon}$ [154]. The activation energy of pure aluminum for creep is found to have a distinct relation with temperature, shows in Fig. 2.25 [155]. The activation energy for a Al–5 wt. % B_4C composite is found to be 200.1 kJ/mol [156] which is higher than pure Al as enforcement particles increase the flow stress. Activation energies of a 2026 Al alloy is reported to be 341 kJ/mol [127], indicates the strengthening elements present in Al matrix can also restrain the flow of material.

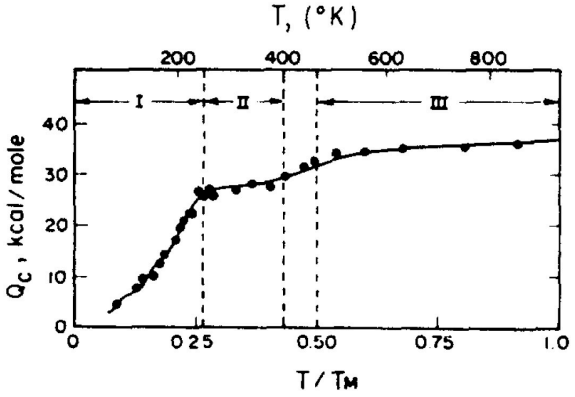

Fig. 2. 25. Activation energy for creep of pure polycrystalline aluminum as a function of temperature [155].

2.4.2 Processing Maps

Dynamic Materials Model is developed by Prasad [157, 158] to understand the constitutive behaviour of the work piece [159, 160]. A typical constitutive relation for a simple dissipater is schematically represented in Fig. 2.26 in the form of the variation of flow stress with strain rate at constant temperature and strain. At any given strain rate, the power P absorbed by the work piece during plastic flow is given by [161]:

$$P = \sigma\dot{\varepsilon} = G + J = \int_0^{\dot{\varepsilon}} \sigma \, d\dot{\varepsilon} + \int_0^{\sigma} \dot{\varepsilon} \, d\sigma \qquad \text{Eq. 2. 8}$$

In Fig. 2.26 the area below the curve is the dissipator content $G = \int_0^{\dot{\varepsilon}} \sigma \, d\dot{\varepsilon}$, and the area above the curve is the dissipator co-content $J = \int_0^{\sigma} \dot{\varepsilon} \, d\sigma$. The G term represents the power dissipated by plastic work, most of which is converted into heat; the remaining small part is stored as lattice defects. The dissipator co-content J is related to the metallurgical mechanisms which occur dynamically to dissipate power [159]. The dynamic material behaviour can be modeled explicitly in terms of variations in the power co-content J with the process parameters.

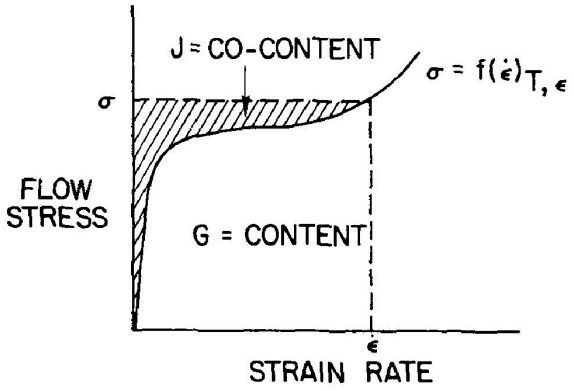

Fig. 2. 26. Schematic representation of G content and J co-content for work piece [159].

From Eq. 2.8, it follows that at any given temperature and strain, the partitioning of power between J and G is given by:

$$\left(\frac{\partial J}{\partial G}\right)_{T,\varepsilon} = \left(\frac{\partial \ln \sigma}{\partial \ln \dot{\varepsilon}}\right)_{T,\varepsilon} = m \qquad \text{Eq. 2. 9}$$

Where m is the strain rate sensitivity of flow stress. In the hot-working range for pure metals, m is temperature and strain rate independent; but in complicated alloy systems, it has been shown to vary with temperature and strain rate [162]. At any given deformation temperature, J is evaluated by combine Eq. 2.8 and Eq. 2.9 as:

$$J = \frac{\sigma \dot{\varepsilon} m}{m+1} \qquad \text{Eq. 2. 10}$$

Considering that the maximum possible rate of dislocation annihilation can only be as fast as the dislocations are generated, the value of J reaches its maximum J_{max} when m=1, shows in Fig. 2.27 and the work piece acts as a linear dissipator; thus [160],

$$J_{\max} = \frac{\sigma \dot{\varepsilon}}{2} \qquad \text{Eq. 2. 11}$$

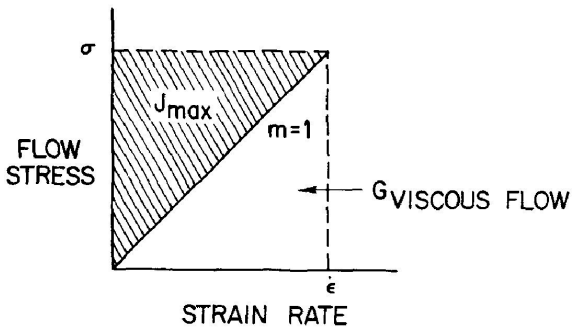

Fig. 2. 27. Schematic representation showing J_{max} which occurs when strain-rate sensitivity m=1 [159].

In this case, one-half of the power is dissipated as material flow and the other half is dissipated as heat. The behaviour of superplastic materials approaches this extreme. The effect of J on the plastic flow of materials can be expressed in terms of efficiency of dissipation, η, which is defined as J/J_{max}. It can be express as [122, 159, 160, 163, 164]:

$$\eta = \frac{J}{J_{\max}} = \frac{2m}{m+1} \qquad \text{Eq. 2. 12}$$

This parameter helps in mapping the dissipative microstructural characteristic of the work piece in a wide range of strain rate and temperature. A schematic three-dimensional map of the efficiency of power dissipation with temperature and strain rate is shown in Fig. 2.28.

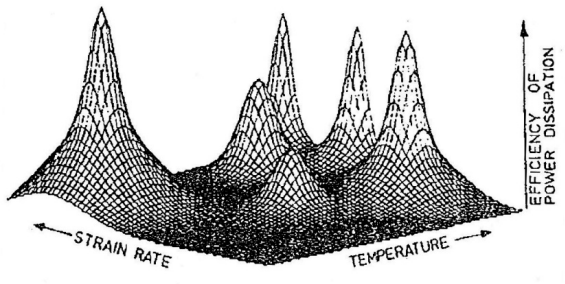

Fig. 2. 28. Schematic map of the variation of the efficiency of power dissipation with temperature and strain rate [164].

In view of the non-linear variation of the flow stress with strain rate, the map will have hills and valleys. A better representation will be in the form of a contour map obtained by sectioning the three-dimensional map at constant efficiency levels, as shown in Fig. 2.29 [164].

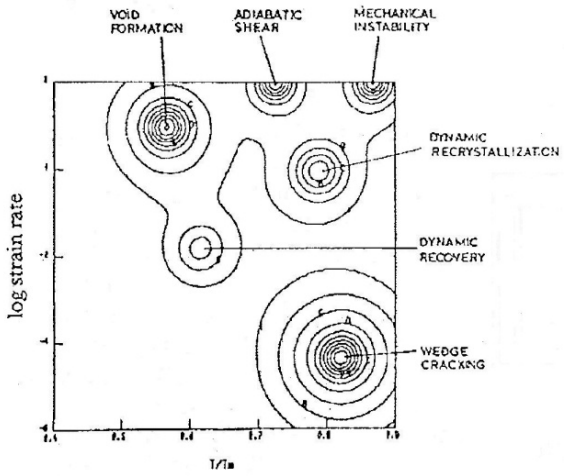

Fig. 2. 29. Contour map showing iso-efficiency contours [164].

Power dissipation maps are generated on the basis of experimental data of flow stress as a function of temperature and strain rate in a wide range. While tensile, compression or torsion techniques may be used; hot compression tests have decisive advantages. First of all,

in a compression test, it is easy to obtain a constant true strain rate. Secondly, in view of a simple cylindrical specimen is convenient to measure the adiabatic temperature rise in the specimen so that temperature correction may be incorporated.

A continuum instability criterion based on the extremum principles of irreversible thermodynamics as applied to large plastic flow [165] has been used to identify the regimes of flow instabilities. The principle of maximum rate of entropy production in metallurgical system results in an instability criterion given by[164]:

$$\xi(\dot{\varepsilon}) = \frac{\partial \ln\left(m/m+1\right)}{\partial \ln \dot{\varepsilon}} + m \leq 0 \quad \text{Eq. 2. 13}$$

The variation of dimensionless parameter $\xi(\dot{\varepsilon})$ with temperature and strain rate constitutes an instability map. Typical microstructural manifestations of flow instabilities are adiabatic shear bands formation, flow localization, dynamic strain aging, mechanical twinning and kinking or flow rotations. The instability map may be superimposed on the power dissipation map in order to show regimes of flow instability. The superimposed map

is called processing maps, on the basis of which metalworking processes may be designed and controlled to optimize hot workability and to produce desired microstructures.

By using the map, the deformation mechanisms in varied deformation conditions can be predicted, and the instable deformation domains that should be avoided during hot deformation process can be received. Accordingly, the deformation techniques can be optimized using the map, and finally, it is also possible to control the structures and properties, reduce the failure rate in deformation process, and increase the production quality and reliability.

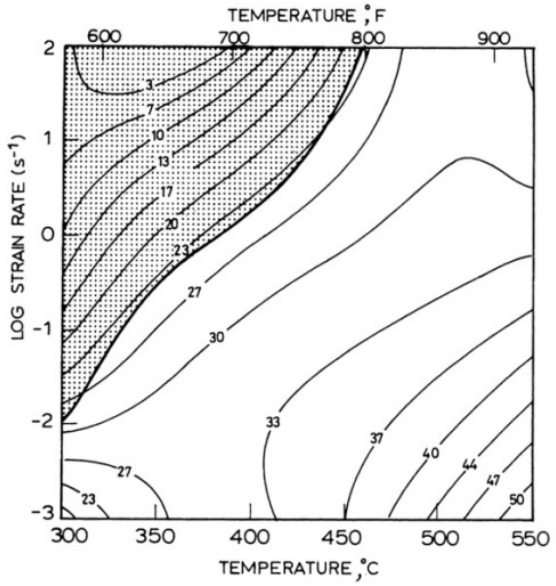

Fig. 2. 30. Processing map of aluminum (99.9%) at a strain of 0.4 [122].

As shown in Fig. 2.30 is the processing map of aluminum (99.9%) at strain of 0.4. Contour numbers represent percent efficiency of power dissipation. Shaded region corresponds to flow instability domain. Fig. 2.31 shows power dissipation map (Fig. 2.31a) and instability map (Fig. 2.31b) for Al−5 vol. % B_4C composite [156]. The maximum dissipation efficiency of 64% occurs in the region of strain rate around 10^{-4} s^{-1} and temperatures 425–475 °C. This high efficiency is caused by dynamic recrystallization (DRX). The low dissipation efficiency regions observed over (i) strain rates 10^{-2}–10^{-1} s^{-1} and temperatures 340–450 °C; and (ii) strain rates 10^{-4}–10^{-3} s^{-1} and temperatures 200–280 °C lead to flow localization in composites.

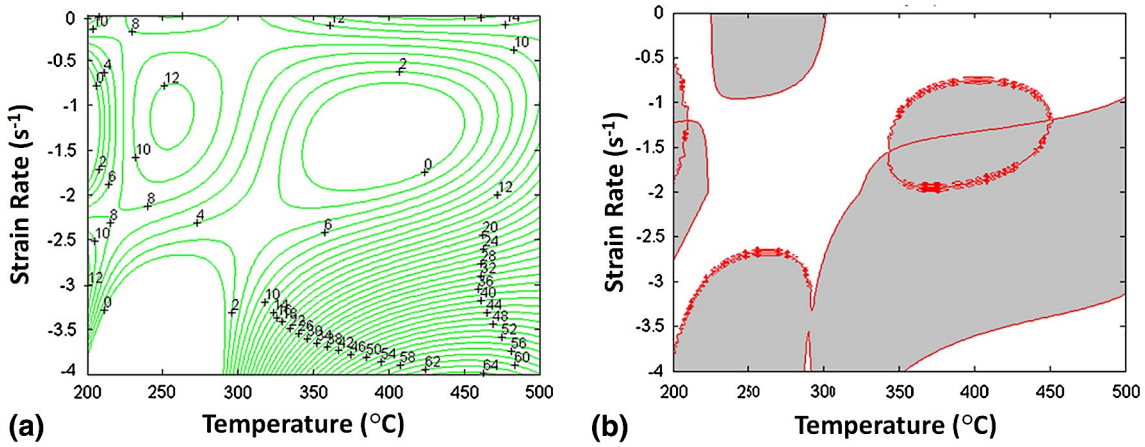

Fig. 2. 31. (a) Power dissipation map and (b) instability map calculated at true strain of 0.5 from compression tests for Al−5 vol. % B_4C composite (inside curves represent isoefficiency labeled) [156].

2.4.3 Post deformation heat treatment

In recent years, many papers have reported the strengthening behaviours and creep behaviours of non-deformed Al–Sc and Al–Sc–Zr alloys [16, 18, 20, 42, 65, 79, 166]. However, the information about post-deformation heat treatment, precipitation behaviour and thermal stability for deformed Al–Sc and Al–Sc–Zr alloys are still limited. The precipitation hardening of Al_3Sc in deformed Alloys were reported to be difficult because of severe limits on the post deformation solution treatment and the post aging heat treatment [6]. In our group previous work, J. Lai found that after an appropriate heat treatment, the hot deformed composites (93% deformation ratio) with Sc and Zr could gain a certain strengthening effect from Al_3ScZr precipitates. The Rockwell hardness of the composites decreases greatly associate with prolong of solution treatment (640 °C) time. Although some research had been done, the reason of this phenomenon was still an

assumption. To improve the mechanical properties of hot rolled composites containing Sc and Zr a good understanding of relation between post deformation heat treatment and mechanical properties is necessary.

2.5 References

[1] Fine ME. Precipitation hardening of aluminum alloys. Metallurgical Transactions A. 1975;6(4):625-30.

[2] Perepezko J, Paik J, Kear B, Giessen B, Cohen M. Rapidly Solidified amorphous and crystalline alloys. Materials Research Society Symposia Proceedings, BH Kear and BC Giessen, eds, Materials Research Society, North-Holland, New York, NY1982.

[3] Griffith W, Sanders Jr R, Hildeman G, Koczak M, Hildeman G. High Strength Powder Metallurgy Aluminum Alloys. The Metallurgical Society of AIME. 1982;209.

[4] Kim Y-W, Griffith WM. Dispersion strengthened aluminum alloys. Phoenix. 1988:1988.

[5] Willey LA. Aluminum Scandium Alloy USA: Aluminum Co. of America 1971.

[6] Toropova LSED, Kharakterova ML, Dobatkina, TV. Advanced aluminum alloys containing scandium : structure and properties. Moscow, Russia: Gordon and Breach Science Publishers; 1998.

[7] Drits ME, Kadaner ES, Dobatkin.Tv, Turkina NI. Scandium-Aluminum Interactions in Aluminum-Rich Side of Al-Sc System. Russ Metall. 1973(4):152-4.

[8] Drits ME, Rokhlin LL, Nikitina NI. Phase-Equilibria in Magnesium-Rich Mg-Y-Sc Alloys. Russ Metall. 1976(4):187-90.

[9] Drits ME, Toropova LS, Bykov YG, Gushchina FL, Elagin VI, Filatov YA. Metastable State Diagram of the Al-Sc System in the Range Rich in Aluminum. Russ Metall. 1983(1):150-3.

[10] Elagin VI, V.V. Zakharov, A.A. Petrova, E.V. Vyshegorodtseva Influence of Scandium on the Structure and Properties of Al-Zn-Mg Alloys. Russ Metall. 1983(4):143-6.

[11] Elagin VI, Zakharov VV, Rostova TD. Some Features of Decomposition for the Solid-Solution of Scandium in Aluminum. Met Sci Heat Treat. 1983;25(7-8):546-9.

[12] Elagin VI, Zakharov VV, Rostova TD. SCANDIUM-ALLOYED ALUMINUM-ALLOYS. Met Sci Heat Treat. 1992;34(1-2):37-45.

[13] Elagin VI, Zakharov VV, Rostova TD. Effect of Scandium on the Structure and Properties of Alloy Al-5.5-Percent Zn-2.0-Percent Mg. Met Sci Heat Treat. 1994;36(7-8):375-80.

[14] Marquis EA, Seidman DN, Dunand DC. Effect of Mg addition on the creep and yield behavior of an Al-Sc alloy. Acta Mater. 2003;51(16):4751-60.

[15] Seidman DN, Marquis EA, Dunand DC. Precipitation strengthening at ambient and elevated temperatures of heat-treatable Al(Sc) alloys. Acta Mater. 2002;50(16):4021-35.

[16] van Dalen ME, Seidman DN, Dunand DC. Creep- and coarsening properties of Al-0.06 at.% Sc-0.06 at.% Ti at 300-450 degrees C. Acta Mater. 2008;56(16):4369-77.

[17] van Dalen ME, Dunand DC, Seidman DN. Effects of Ti additions on the nanostructure and creep properties of precipitation-strengthened Al-Sc alloys. Acta Mater. 2005;53(15):4225-35.

[18] Marquis EA, Seidman DN, Dunand DC. Precipitation strengthening at ambient and elevated temperatures of heat-treatable Al(Sc) alloys. Acta Mater. 2002;50(16):4021-35.

[19] Marquis EA, Dunand DC. Model for creep threshold stress in precipitation-strengthened alloys with coherent particles. Scripta Materialia. 2002;47(8):503-8.

[20] Fuller CB, Seidman DN, Dunand DC. Creep properties of coarse-grained Al(Sc) alloys at 300¬∞C. Scr Mater. 1999;40(6):691-6.

[21] Fuller CB, Krause AR, Dunand DC, Seidman DN. Microstructure and mechanical properties of a 5754 aluminum alloy modified by Sc and Zr additions. Materials Science and Engineering A. 2002;338(1-2):8-16.

[22] Davydov VG, Rostova TD, Zakharov VV, Filatov YA, Yelagin VI. Scientific principles of making an alloying addition of scandium to aluminium alloys. Mater Sci Eng A-Struct Mater Prop Microstruct Process. 2000;280(1):30-6.

[23] Knipling KE, Dunand DC, Seidman DN. Criteria for developing castable, creep-resisitant aluminum-based alloys-A review. ZMetallkd. 2006;97(3):246-65.

[24] Harada Y, Dunand DC. Microstructure of Al_3Sc with ternary transition-metal additions. Materials Science and Engineering A. 2002;329-331:686-95.

[25] van Dalen M. Microstructure and Creep Properties of Al-Sc Alloys Micro-alloyed with Lanthanides (Yb or Gd) and Transition Metals (Ti or Zr). EVANSTON: NORTHWESTERN UNIVERSITY; 2007.

[26] Forbord B, Auran L, Lefebvre W, Hallem H, Marthinsen K. Rapid precipitation of dispersoids during extrusion of an Al-0.91 wt.% Mn-0.13 wt.% Zr-0.17 wt.% Sc-alloy. Materials Science and Engineering A. 2006;424(1-2):174-80.

[27] Fujikawa SI, Sugaya M, Takei H, Hirano K. SOLID SOLUBILITY AND RESIDUAL RESISTIVITY OF SCANDIUM IN ALUMINUM. Journal of the Less-Common Metals. 1979;63(1):87-97.

[28] Blake N, Hopkins MA. Constitution and age hardening of Al-Sc alloys. J Mater Sci. 1985;20(8):2861-7.

[29] Kononenko VL, Golubev SV. PHASE-DIAGRAMS OF BINARY-SYSTEMS OF ALUMINUM WITH LA, CE, PR, ND, SM, EU, YB, SC AND Y. Russ Metall. 1990(2):193-5.

[30] Sawtell RR, Morris JW. EXPLORATORY ALLOY DEVELOPMENT IN THE SYSTEM AL-SC-X. Journal of Metals. 1988;40(11):113-.

[31] Sawtell RR, Jensen CL. MECHANICAL-PROPERTIES AND MICROSTRUCTURES OF AL-MG-SC ALLOYS. Metallurgical Transactions a-Physical Metallurgy and Materials Science. 1990;21(2):421-30.

[32] Royset J, Ryum N. Scandium in aluminium alloys. Int Mater Rev. 2005;50(1):19-44.

[33] Zalutskii I, Kripyakevich P. RAl $ sub 3$ COMPOUNDS IN RARE EARTH--ALUMINUM SYSTEMS AND THEIR CRYSTAL STRUCTURES. Lvov State Univ.; 1967.

[34] Rechkin V, Lamikhov L, Samsonova T. CRYSTAL STRUCTURES OF SOME SCANDIUM ALUMINIDES. Soviet Phys-Cryst(English Transl). 1964;9:325-7.

[35] Murray JL. The Al-Sc (aluminum-scandium) system. J Phase Equilib. 1998;19(4):380-4.

[36] L.S. Toropova DGE, M.L. Kharakterova and T.V. Dobatkina. Advanced aluminum alloys containing scandium: structure and properties Amsterdam, The Netherlands: Gordon and Breach Science; 1998.

[37] Jo HH, Fujikawa SI. Kinetics of Precipitation in Al-Sc Alloys and Low-Temperature Solid Solubility of Scandium In Aluminum Studied by Electrical-Resistivity Measurements. Materials Science and Engineering A. 1993;171(1-2):151-61.

[38] Nakayama M, Furuta A, Miura Y. Precipitation of Al_3Sc in Al-0.23 mass%Sc alloy. Mater Trans JIM. 1997;38(10):852-7.

[39] Sano N, Hasegawa Y, Hono K, Jo H, Hirano K, Pickering H, et al. Precipitation process of Al-Sc alloys. Le Journal de Physique Colloques. 1987;48(C6):C6-337-C6-42.

[40] Miura Y NM, Furuta A. In: Proceedings of 7th JIM Int Symp on Aspects of High Temperature Deformation and Fracture in Crystalline Materials. Nagoya, Conference 1993, Conference. p. 25-5.

[41] Marquis EA, Seidman DN. Coarsening kinetics of nanoscale Al_3Sc precipitates in an Al-Mg-Sc alloy. Acta Mater. 2005;53(15):4259-68.

[42] Fuller CB, Seidman DN, Dunand DC. Mechanical properties of Al(Sc,Zr) alloys at ambient and elevated temperatures. Acta Mater. 2003;51(16):4803-14.

[43] Karnesky RA, van Dalen ME, Dunand DC, Seidman DN. Effects of substituting rare-earth elements for scandium in a precipitation-strengthened Al,Äì0.08 at. %Sc alloy. Scr Mater. 2006;55(5):437-40.

[44] Karnesky RA, van Dalen ME, Dunand DC, Seidman DN. Effects of substituting rare-earth elements for scandium in a precipitation-strengthened Al-0.08 at. %Sc alloy. Scr Mater. 2006;55(5):437-40.

[45] Karnesky RA, Dunand DC, Seidman DN. Evolution of nanoscale precipitates in Al microalloyed with Sc and Er. Acta Mater. 2009;57(14):4022-31.

[46] Beeri O, Dunand DC, Seidman DN. Roles of impurities on precipitation kinetics of dilute Al-Sc alloys. Materials Science and Engineering A. 2010;527(15):3501-9.

[47] Knipling KE, Karnesky RA, Lee CP, Dunand DC, Seidman DN. Precipitation evolution in Al-0.1Sc, Al-0.1Zr and Al-0.1Sc-0.1Zr (at.%) alloys during isochronal aging. Acta Mater. 2010;58(15):5184-95.

[48] Knipling KE, Seidman DN, Dunand DC. Ambient- and high-temperature mechanical properties of isochronally aged Al-0.06Sc, Al-0.06Zr and Al-0.06Sc-0.06Zr (at.%) alloys. Acta Mater. 2011;59:943–54.

[49] Krug ME, Seidman DN, Dunand DC. Creep properties and precipitate evolution in Al–Li alloys microalloyed with Sc and Yb. Materials Science and Engineering: A. 2012;550(0):300-11.

[50] Hyland Jr R, Stiffler R. Determination of the elastic constants of polycrystalline Al< sub> 3</sub> Sc. Scripta metallurgica et materialia. 1991;25(2):473-7.

[51] Drits ME, Toropova LS, Bykov YG, Gushchina FL, Elagin VI, Filatov YA. Metastable State Diagram of the Al-Sc System in the Range Rich in Aluminum. Russian Metallurgy. 1984(1):83.

[52] Fu C. Electronic, elastic, and fracture properties of trialuminide alloys: Al3Sc and Al3Ti. Journal of Materials Research. 1990;5(05):971-9.

[53] Fukunaga K, Shouji T, Miura Y. Temperature dependence of dislocation structure of L12–Al3Sc. Materials Science and Engineering: A. 1997;239–240(0):202-5.

[54] George EP, Pope DP, Fu CL, Schneibel JH. Deformation and Fracture of L1$_2$ Trialuminides. ISIJ International. 1991;31(10):1063-75.

[55] Karnesky RA, Meng L, Dunand DC. Strengthening mechanisms in aluminum containing coherent Al3Sc precipitates and incoherent Al2O3 dispersoids. Acta Materialia. 2007;55(4):1299-308.

[56] Nembach E. Particle strengthening of metals and alloys: Wiley-VCH; 1 edition December 6, 1996.

[57] Watanabe C, Kondo T, Monzen R. Coarsening of Al3Sc precipitates in an Al-0.28 wt pct Sc alloy. METALLURGICAL AND MATERIALS TRANSACTIONS A. 2004;35A(9):3003-8.

[58] Harada Y, Dunand DC. Thermal expansion of Al3Sc and Al-3(Sc0.75X0.25). Scr Mater. 2003;48(3):219-22.

[59] Touloukian Y, Kirby R, Taylor R, Desai P. Thermal expansion: Metallic elements and alloys.[Handbook. 1975.

[60] Simmons R, Balluffi R. Measurements of equilibrium vacancy concentrations in aluminum. Physical Review. 1960;117(1):52.

[61] Iwamura S, Miura Y. Loss in coherency and coarsening behavior of Al 3 Sc precipitates. Acta Materialia. 2004;52(3):591-600.

[62] Lifshitz IM, Slyozov VV. THE KINETICS OF PRECIPITATION FROM SUPERSATURATED SOLID SOLUTIONS. J Phys Chem Solids. 1961;19(1-2):35-50.

[63] Wagner C. Theorie Der Alterung Von Niederschlagen Durch Umlosen (Ostwald-Reifung). Zeitschrift Fur Elektrochemie. 1961;65(7-8):581-91.

[64] Ardell AJ. Precipitation hardening. Metallurgical Transactions A. 1985;16(12):2131-65.

[65] Marquis E, Seidman D. Nanoscale structural evolution of Al 3 Sc precipitates in Al (Sc) alloys. Acta materialia. 2001;49(11):1909-19.

[66] Davydov VG, Elagin VI, Zakharov VV, Rostova TD. Alloying aluminum alloys with scandium and zirconium additives. Met Sci Heat Treat. 1996;38(7-8):347-52.

[67] Forbord B, Hallem H, Royset J, Marthinsen K. Thermal stability of $Al_3(Sc_x,Zr_{1-x})$-dispersoids in extruded aluminium alloys. Materials Science and Engineering A. 2008;475(1-2):241-8.

[68] Davydov V, Rostova T, Zakharov V, Filatov YA, Yelagin V. Scientific principles of making an alloying addition of scandium to aluminium alloys. Materials Science and Engineering: A. 2000;280(1):30-6.

[69] Elagin VIZ, V V; Pavlenko, S G; Rostova, T D Influence of Zirconium Additions on Aging of Aluminum--Scandium Alloys. (Translation) Physics of Metals and Metallography. 1985;60(1):88-92.

[70] Vetrano JS, Henager CH, Smith MT, Bruemmer SM. Microstructural development for superplasticity in Al-Mg-Mn alloys. Warrendale: Minerals, Metals & Materials Soc; 1999.

[71] Tolley A, Radmilovic V, Dahmen U. Segregation in Al-3(Sc,Zr) precipitates in Al-Sc-Zr alloys. Scripta Materialia. 2005;52(7):621-5.

[72] Forbord B, Lefebvre W, Danoix F, Hallem H, Marthinsen K. Three dimensional atom probe investigation on the formation of Al-3(Sc,Zr)-dispersoids in aluminium alloys. Scripta Materialia. 2004;51(4):333-7.

[73] Harada Y, Dunand DC. Microstructure of Al(3)Sc with ternary transition-metal additions. Mater Sci Eng A-Struct Mater Prop Microstruct Process. 2002;329:686-95.

[74] Toropova LS, Kamardinkin AN, Kindzhibalo VV, Tyvanchuk AT. STUDIES OF AL-SC-ZR ALLOYS IN ALUMINUM-RICH REGION. Fiz Metallov Metalloved. 1990(12):108-11.

[75] Fujikawa SI. Impurity diffusion of scandium in aluminum. Defect and Diffusion Forum. 1997;143:115-20.

[76] Clouet E, Barbu A, Lae L, Martin G. Precipitation kinetics of Al_3 Zr and Al_3 Sc in aluminum alloys modeled with cluster dynamics. Acta Mater. 2005;53:2313-25.

[77] Senkov ON, Shagiev MR, Senkova SV, Miracle DB. Precipitation of Al_3 (Sc,Zr) particles in an Al-Zn-Mg-Cu-Sc-Zr alloy during conventional solution heat treatment and its effect on tensile properties. Acta Mater. 2008;56(15):3723-38.

[78] Fuller CB, Seldman DN. Temporal evolution of the nanostructure of Al(Sc,Zr) alloys: Part II-coarsening of $Al_3(Sc_{1-x}Zr_x)$ precipitates. Acta Materialia. 2005;53(20):5415-28.

[79] Fuller CB, Seldman DN. Temporal evolution of the nanostructure of Al(Sc,Zr) alloys: Part II-coarsening of $Al_3(Sc_{1-x}Zr_x)$ precipitates. Acta Mater. 2005;53(20):5415-28.

[80] Chen XG. Interface reaction of boron carbide in aluminum matrix composites and its control. In: Schlesinger ME, editor. EPD congress 2005: TMS 2005. p. 101-6.

[81] Thevenot F. Boron Carbide - A Comprehensive Review. J European Ceram Soc. 1990(6):205-25.

[82] Gericke MT, Bowman JD, Carlini RD, Chupp TE, Coulter KP, Dabaghyan M, et al. Commissioning of the NPDGamma detector array: Counting statistics in current mode operation and parity violation in the capture of cold neutrons on B4C and Al-27. J Res Natl Inst Stand Technol. 2005;110(3):215-9.

[83] JICHUN YE JH, and JULIE M. SCHOENUNG. Cryomilling for the Fabrication of a Particulate B4C Reinforced Al Nanocomposite: Part I. Effects of Process Conditions on Structure. METALLURGICAL AND MATERIALS TRANSACTIONS A. 2006;37(10):3099.

[84] Asthana R. Interfaces in cast composites. Solidification Processing of Reinforced Metals. Zurich-Uetikon: Transtec Publications Ltd; 1998. p. 301-50.

[85] Chawla N, Shen YL. Mechanical behavior of particle reinforced metal matrix composites. Adv Eng Mater. 2001;3(6):357-70.

[86] Asthana R. Processing effects on the engineering properties of cast metal-matrix composites. Adv Perform Mater. 1998;5(3):213-55.

[87] Alman DE. Properties of Metal-Matrix Composites. ASM Handbook: composites. OH: ASM International; 2001.

[88] Halverson DC, Pyzik AJ, Aksay IA, Snowden WE. Processing of Boron Carbide-Aluminum Composites. J Am Ceram Soc. 1989;72(5):775-80.

[89] Zhang Z, K. Fortin, A. Charette, X.-G. Chen. Effect of Titanium on castability of Al-B_4C composites. In: Hirsch J, Günter Gottstein, Birgit Skrotzki, editor. Aluminium

Alloys: Their Physical and Mechanical Properties (ICAA 11). Aachen, Germany: Wiley-VCH 2008. p. 434-40.

[90] Zhang Z, Chen XG, Charette A. Fluidity and microstructure of an Al-10% B4C composite. J Mater Sci. 2009;44(2):492-501.

[91] Viala JC, Bouix J, Gonzalez G, Esnouf C. Chemical reactivity of aluminium with boron carbide. J Mater Sci. 1997;32(17):4559-73.

[92] Kouzeli M, San Marchi C, Mortensen A. Effect of reaction on the tensile behavior of infiltrated boron carbide-aluminum composites. Materials Science and Engineering A. 2002;337(1-2):264-73.

[93] Zhang Z, Chen XG, Charette A. Particle distribution and interfacial reactions of Al-7%Si-10%B4C die casting composite. J Mater Sci. 2007;42(17):7354-62.

[94] Zhang Z, Fortin K, Charette A, Chen XG. Effect of titanium on microstructure and fluidity of Al-B_4C composites. J Mater Sci.

[95] Lai J, Zhang Z, Chen XG. Precipitation strengthening of Al–B4C metal matrix composites alloyed with Sc and Zr. J Alloy Compd. 2013;552(0):227-35.

[96] Lai J, Zhang Z, Chen XG. Effect of Sc, Zr, and Ti on the interfacial reactions of the B_4C/Al system. J Mater Sci. 2011;46(2):451-9

[97] Lai J, Zhang Z, Chen XG. The thermal stability of mechanical properties of Al-B4C composites alloyed with Sc and Zr at elevated temperatures. Mater Sci Eng A-Struct Mater Prop Microstruct Process. 2012;532:462-70.

[98] Lai J, Zhang Z, Chen X. Effect of Sc and Zr alloying on microstructure and precipitation evolution of as cast Al-B4C metal matrix composites. Materials Science and Technology. 2012;28(11):1276-86.

[99] Chen XG, St-Georges L, Roux M. Mechanical Behavior of High Boron Content Al-B4C Metal Matrix Composites at Elevated Temperatures. Materials Science Forum: Trans Tech Publ; 2012. p. 631-7.

[100] Clyne TW, Withers PJ. An Introduction to Metal Matrix Composites. Cambridge [England]: New York, NY, USA : Cambridge University Press; 1993.

[101] Miracle DB, Donaldson SL, Committee ASMIH. ASM handbook. Volume 21, Composites. Material Park, Ohio: ASM International; 2001.

[102] Taya M, Lulay KE, Lloyd DJ. Strengthening of a Particulate Metal Matrix Composite by Quenching. Acta Metall Mater. 1991;39(1):73-87.

[103] Smagorinski ME, Tsantrizos PG, Grenier S, Brzezinski T, Kim G. The properties and microstructure of Al-based composites reinforced with ceramic particles. Materials Science and Engineering A. 1998;244(1):86-90.

[104] Kaufman JG. Properties of aluminum alloys: tensile, creep, and fatigue data at high and low temperatures. USA1999.

[105] Kisel VP. MECHANISM OF FORMATION AND MECHANICAL-BEHAVIOR OF TILT GRAIN-BOUNDARIES. Phys Status Solidi A-Appl Res. 1995;149(1):61-8.

[106] Kissel NS, Kisel VP. Microscopic mechanisms of low-temperature yield stress anomaly in solids. Materials Science and Engineering A. 2001;309:97-101.

[107] Dieter GE, Bacon D. Mechanical metallurgy. London: McGraw-Hill; 1988.

[108] Kakani SL, Kakani A. Material science. New Delhi: New Age International; 2004.

[109] Nembach E. Particle strengthening of metals and alloys. New York: Wiley; 1997.

[110] Argon AS, Orowan E. Physics of strength and plasticity. Cambridge: M.I.T. Press; 1969.

[111] Kelly A, Nicholson R. Strengthening methods in crystals. Amsterdam; New York: Elsevier Pub. Co.; 1971.

[112] Brown L, Ham R. Dislocation-particle interactions. Strengthening methods in crystals. 1971:9-135.

[113] Shewfelt R, Brown L. High−temperature strength of dispersion-hardened single crystals II. Theory. Philosophical Magazine. 1977;35(4):945-62.

[114] Rösler J, Arzt E. The kinetics of dislocation climb over hard particles—I. Climb without attractive particle-dislocation interaction. Acta Metallurgica. 1988;36(4):1043-51.

[115] Lagneborg R. Bypassing of dislocations past particles by a climb mechanism. Scripta Metallurgica. 1973;7(6):605-13.

[116] Dundurs J. Elastic interaction of dislocations with inhomogeneities. Mathematical theory of dislocations. 1969:70-115.

[117] Arzt E, Ashby MF. Threshold stresses in materials containing dispersed particles. Scripta Metallurgica. 1982;16(11):1285-90.

[118] Cadek J, Zhu S, Milicka K. Threshold creep behaviour of aluminium dispersion strengthened by fine alumina particles. Materials Science and Engineering: A. 1998;252(1):1-5.

[119] Srolovitz D, Luton M, Petkovic-Luton R, Barnett D, Nix W. Diffusionally modified dislocation-particle elastic interactions. Acta Metallurgica. 1984;32(7):1079-88.

[120] Sellars C, Tegart WMG. Relation between flow stress and structure in hot deformation. Memoires Scientifiques de la Revue de Metallurgie. 1966;67(9):731-46.

[121] McQueen HJ, Ryan ND. Constitutive analysis in hot working. Materials Science and Engineering: A. 2002;322(1–2):43-63.

[122] Prasad YVRK. Hot Working Guide: A Compendium of Processing Maps: ASM International; 1997.

[123] McQueen H. Dynamic recovery and recrystallization. Encyclopedia of Materials: Science and Technology. 2001:2375-81.

[124] Li Y, Liu Z, Lin L, Peng J, Ning A. Deformation behavior of an Al–Cu–Mg–Mn–Zr alloy during hot compression. Journal of materials science. 2011;46(11):3708-15.

[125] Cavaliere P. Hot and warm forming of 2618 aluminium alloy. Journal of light metals. 2002;2(4):247-52.

[126] Ebrahimi G, Zarei-Hanzaki A, Haghshenas M, Arabshahi H. The effect of heat treatment on hot deformation behaviour of Al 2024. journal of materials processing technology. 2008;206(1):25-9.

[127] Huang X, Zhang H, Han Y, Wu W, Chen J. Hot deformation behavior of 2026 aluminum alloy during compression at elevated temperature. Materials Science and Engineering: A. 2010;527(3):485-90.

[128] Zhang H, Li L, Yuan D, Peng D. Hot deformation behavior of the new Al–Mg–Si–Cu aluminum alloy during compression at elevated temperatures. Materials Characterization. 2007;58(2):168-73.

[129] Cerri E, Evangelista E, Forcellese A, McQueen H. Comparative hot workability of 7012 and 7075 alloys after different pretreatments. Materials Science and Engineering: A. 1995;197(2):181-98.

[130] Chen S, Chen K, Peng G, Chen X, Ceng Q. Effect of heat treatment on hot deformation behavior and microstructure evolution of 7085 aluminum alloy. Journal of Alloys and Compounds. 2012;537:338-45.

[131] Jin N, Zhang H, Han Y, Wu W, Chen J. Hot deformation behavior of 7150 aluminum alloy during compression at elevated temperature. Materials characterization. 2009;60(6):530-6.

[132] Liu XY, Pan QL, He YB, Li WB, Liang WJ, Yin ZM. Flow behavior and microstructural evolution of Al–Cu–Mg–Ag alloy during hot compression deformation. Materials Science and Engineering: A. 2009;500(1):150-4.

[133] Fridlyander JN, Kolobnev NI, Grushko OE, Sheveleva LM, Khokhlatova LB, Miller WS, et al. Alloying components optimization of weldable Ag-Li-Mg alloy. In: Driver JH, Dubost B, Durand F, Fougeres R, Guyot P, Sainfort P, et al., editors. Aluminium Alloys: Their Physical and Mechanical Properties, Pts 1-3. Zurich-Uetikon: Transtec Publications Ltd; 1996. p. 1847-51.

[134] Miura Y, Shioyama T, Hara D. Recrystallization of Al-3Mg and Al-3Mg-0.2Sc alloys. In: Driver JH, Dubost B, Durand F, Fougeres R, Guyot P, Sainfort P, et al., editors. Aluminium Alloys: Their Physical and Mechanical Properties, Pts 1-3. Zurich-Uetikon: Transtec Publications Ltd; 1996. p. 505-10.

[135] Roder O, Schauerte O, Lutjering G, Gysler A. Correlation between microstructure and mechanical properties of Al-Mg alloys without and with scandium. In: Driver JH, Dubost B, Durand F, Fougeres R, Guyot P, Sainfort P, et al., editors. Aluminium Alloys:

Their Physical and Mechanical Properties, Pts 1-3. Stafa-Zurich: Trans Tech Publications Ltd; 1996. p. 1835-40.

[136] Davydov VG, Yelagin VI, Zakharov VV, Filatov YA. On prospects of application of new 01570 high-strength weldable Al-Mg-Sc alloy in aircraft industry. In: Driver JH, Dubost B, Durand F, Fougeres R, Guyot P, Sainfort P, et al., editors. Aluminium Alloys: Their Physical and Mechanical Properties, Pts 1-3. Zurich-Uetikon: Transtec Publications Ltd; 1996. p. 1841-6.

[137] Lee WS, Chen TH. Strain rate and temperature effects on dynamic properties of high-strength weldable aluminum-scandium alloy. Journal of Materials Research. 2009;24(1):198-211.

[138] Nieh TG, Hsiung LM, Wadsworth J, Kaibyshev R. High strain rate superplasticity in a continuously recrystallized Al-6%Mg-0.3%Sc alloy. Acta Materialia. 1998;46(8):2789-800.

[139] Kaibyshev R, Sitdikov O, Olenyov S. Ultrafine grain formation during equal channel angular extrusion in an Al-Mg-Sc alloy. Warrendale: Minerals, Metals & Materials Soc; 2002.

[140] Sitdikov O, Sakai T, Avtokratova E, Kaibyshev R, Kimura Y, Tsuzaki K. Grain refinement in a commercial Al-Mg-Sc alloy under hot ECAP conditions. Mater Sci Eng A-Struct Mater Prop Microstruct Process. 2007;444(1-2):18-30.

[141] Fuller CB, Krause AR, Dunand DC, Seidman DN. Microstructure and mechanical properties of a 5754 aluminum alloy modified by Sc and Zr additions. Mater Sci Eng A-Struct Mater Prop Microstruct Process. 2002;338(1-2):8-16.

[142] Ferry M, Hamilton NE, Humphreys FJ. Continuous and discontinuous grain coarsening in a fine-grained particle-containing Al-Sc alloy. Acta Mater. 2005;53(4):1097-109.

[143] Srivatsan T, Mattingly J. Influence of heat treatment on the tensile properties and fracture behaviour of an aluminium alloy-ceramic particle composite. Journal of materials science. 1993;28(3):611-20.

[144] Christman T, Needleman A, Suresh S. An experimental and numerical study of deformation in metal-ceramic composites. Acta Metallurgica. 1989;37(11):3029-50.

[145] Srivastava V, Jindal V, Uhlenwinkel V, Bauckhage K. Hot-deformation behaviour of spray-formed 2014 Al+ SiC P metal matrix composites. Materials Science and Engineering: A. 2008;477(1):86-95.

[146] Dutta I, Sims J, Seigenthaler D. An analytical study of residual stress effects on uniaxial deformation of whisker reinforced metal-matrix composites. Acta metallurgica et materialia. 1993;41(3):885-908.

[147] Senthilkumar V, Balaji A, Narayanasamy R. Analysis of hot deformation behavior of Al 5083–TiC nanocomposite using constitutive and dynamic material models. Materials & Design. 2012;37:102-10.

[148] Chen C, Qin S, Li S, Wen J. Finite element analysis about effects of particle morphology on mechanical response of composites. Materials Science and Engineering: A. 2000;278(1):96-105.

[149] Sørensen N, Suresh S, Tvergaard V, Needleman A. Effects of reinforcement orientation on the tensile response of metal-matrix composites. Materials Science and Engineering: A. 1995;197(1):1-10.

[150] Vasudevan A, Richmond O, Zok F, Embury J. The influence of hydrostatic pressure on the ductility of Al□ SiC composites. Materials Science and Engineering: A. 1989;107:63-9.

[151] McQueen HJ, Blum W. Dynamic recovery: sufficient mechanism in the hot deformation of Al (< 99.99). Materials Science and Engineering a-Structural Materials Properties Microstructure and Processing. 2000;290(1-2):95-107.

[152] McQueen HJ, Evangelista E, Kassner ME. The classification and determination of restoration mechanisms in the hot working of al alloys. Zeitschrift für Metallkunde. 1991;82(5):336-45.

[153] Blum W, McQueen H. Dynamics of recovery and recrystallization. Materials Science Forum: Trans Tech Publ; 1996. p. 31-42.

[154] McQueen HJ, Spigarelli S, Kassner ME, Evangelista E. Hot deformation and processing of aluminum alloys: CRC Press; 2011.

[155] Sherby OD, Burke PM. Mechanical behavior of crystalline solids at elevated temperature. Progress in Materials Science. 1968;13:323-90.

[156] Gangolu S, Rao A, Prabhu N, Deshmukh V, Kashyap B. Hot Workability and Flow Characteristics of Aluminum-5 wt.% B4C Composite. Journal of materials engineering and performance. 2014;23(4):1366-73.

[157] Prasad Y, Sasidhara S. Hot working guide: a compendium of processing maps: ASM international; 1997.

[158] Wellstead PE. introduction to physical systems modeling. london: academic press; 1979.

[159] Prasad Y, Gegel HL, Doraivelu SM, Malas JC, Morgan JT, Lark KA, et al. MODELING OF DYNAMIC MATERIAL BEHAVIOR IN HOT DEFORMATION - FORGING OF TI-6242. Metallurgical Transactions a-Physical Metallurgy and Materials Science. 1984;15(10):1883-92.

[160] Gegel HL, Malas JC, Doraivelu SM, Shende VA. Modeling techniques used in forging process design: american society for matals; 1987.

[161] Prasad Y. Processing maps: a status report. Journal of Materials Engineering and Performance. 2003;12(6):638-45.

[162] Dadras P, Thomas JF. CHARACTERIZATION AND MODELING FOR FORGING DEFORMATION OF TI-6AL-2SN-4ZR-2MO-0.1 SI. Metallurgical Transactions a-Physical Metallurgy and Materials Science. 1981;12(11):1867-76.

[163] Parker BA, Zhou ZF, Nolle P. The Effect of Small Additions of Scandium on the Properties of Aluminum-Alloys. J Mater Sci. 1995;30(2):452-8.

[164] Prasad Y. RECENT ADVANCES IN THE SCIENCE OF MECHANICAL PROCESSING. Indian Journal of Technology. 1990;28(6-8):435-51.

[165] Ziegler H, Sneedon IN. Progress in Solid Mechanics. New York: Wiley; 1963.

[166] Fuller CB, Murray JL, Seidman DN. Temporal evolution of the nanostructure of Al(Sc,Zr) alloys: Part I - Chemical compositions of $Al_3(Sc_{1-x}Zr_x)$ precipitates. Acta Mater. 2005;53(20):5401-13.

CHAPTER 3

EXPERIMENTAL

Chapter 3

Experimental

3.1 Al−B_4C composites preparation

Three experimental Al−B_4C composites were prepared. Their nominal chemical compositions are listed in Table 3.1.

Table 3. 1. Nominal chemical composition of experimental composites

Code	Element (wt.%)				
	Sc	Zr	Ti	B_4C (vol.%)	Al
Base composite	−	−	1.50	15	
S40	0.40	−	1.50	15	Balance
SZ40	0.40	0.24	1.50	15	

In the composite melt preparation, commercial pure aluminum (99.7%) was first melted in an electric resistance furnace. The preheated master alloys, Al−2 wt. % Sc, Al−15

wt. % Zr and Al−10 wt. % Ti were then added into the aluminum liquid and held at 800 °C for 40 minutes to encourage the dissolution of master alloys. The electric resistance furnace is shown in Fig. 3.1.

Fig. 3. 1. The electric resistance furnace used for composites preparation with a controllable stirring facility.

Prefabricated Al 1100−25 vol. % B_4C with 2.0 wt. % Ti cast ingots, supplied by Rio Tinto Alcan, were subsequently introduced into the alloyed melt. The average size of the

B_4C particles (F360) was 23 μm. The composite melt was held at 740 °C for 30 minutes with mechanical stirring to ensure a uniform distribution of B_4C particles in the melt, and then cast into a preheated permanent steel mould with a dimension of 30×40×80 mm as shown in Fig. 3.2.

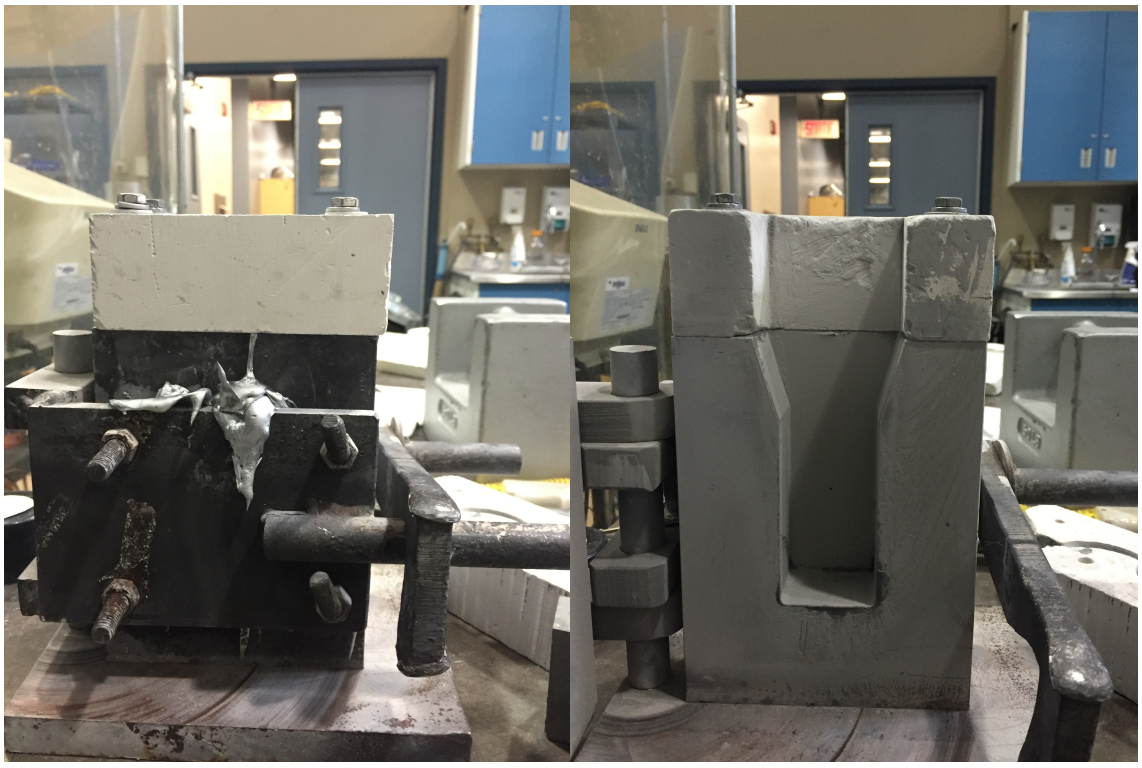

Fig. 3. 2. Steel mold.

3.2 Hot deformation of Al−B_4C composites

Before hot rolling, the S40 and SZ40 composites were homogenized at 640 °C for 24 hours and 96 hours, respectively, then quenched to water at room temperature. The cast ingots were hot-rolled on a laboratory scale rolling mill (STANAT CX-100) as shown in Fig. 3.3, with multi-passes at 500 °C. Due to the limitation of the small mill, multi-passes were applied during the hot rolling process. Prior to the hot rolling, the composites were preheated to 500 °C and kept at this temperature for 5 to 30 minutes, depending on the thickness of intermediate rolling plates. The cracking edges were cut during hot rolling. The detailed hot-rolling procedure is listed in Table 3.2.

Fig. 3. 3. STANAT CX–100 laboratory scale rolling machine.

Table 3. 2. Hot-rolling procedure and parameter.

Step	Thickness (mm)	Decrease (mm)	Pass number	Deformation ratio (%)	Annealing temperature (°C)
1	27.8	5.8	6	0.209	500
2	22	4	4	0.182	500
3	18	3	4	0.167	500
4	15	2.25	3	0.150	500
5	12.75	2.25	3	0.176	500
6	Cutting edge				
7	10.5	1	1	0.095	500
8	9.5	0.75	1	0.079	500
9	8.5	0.75	1	0.088	500
10	8	0.75	1	0.094	500
11	7.25	0.75	1	0.103	500
12	6.5	0.75	1	0.115	500
13	5.75	0.75	1	0.130	500
14	5	0.5	1	0.100	500
15	4.5	0.5	1	0.111	500
16	4	0.5	1	0.125	500
17	Cutting edge				
18	3.5	0.5	1	0.143	500
19	3	0.25	1	0.083	500
20	2.75	0.25	1	0.091	500
21	2.5	0.25	1	0.100	500
22	2.25	0.25	1	0.111	500
23	2				

3.3 Heat treatment

A series of heat treatments were conducted in order to follow the homogenization of segregations, dissolution of strengthening elements and the precipitation of precipitates of the Al–B_4C composites. The homogenization and solution heat treatments were carried out in a BLUE-M ELECTRIC furnace having ± 5 °C as a temperature variation at 640°C. The specimens were quenched in water at room temperature after treatment. The long term annealing procedures were conducted in the electric furnaces (THERMOLYNE) with temperature variation of ± 2°C.

3.3.1 Heat treatment of un-deformed Al–B_4C composites

To obtain the precipitation strengthening, the cast ingots of S40 were homogenized at 640 ºC for 24 h whereas SZ40 were treated at 640 ºC for 96 h, and then quenched in water at room temperature. The homogenized samples of S40 and SZ40 were aged at 300 ºC for 24 h, at which the hardness or yield strength of the composites reached the maximum

values [1]. The applied heat treatment processes were based on our previous works [1, 2] and the aging paraments are listed in Table 3.3. The unalloyed Al 1100–15 vol. % B_4C samples (base composite) were tested in the as-cast condition due to its non-heat-treatable nature. Moreover, to evaluate the long-term thermal stability, S40 and SZ40 samples on the peak aging condition were annealed at elevated temperatures 250 to 350 °C up to 2000 hours (Table 3.3).

Table 3. 3. Peak aging and annealing parameters

Code	Aging		Annealing			
	T (°C)	Time (h)	T (°C)	Time (h)		
S40	300	24	250	500	1000	2000
			300	500	1000	2000
SZ40	300	24	300	500	1000	2000
			350	500	1000	2000

3.3.2 Post deformation heat treatment of Al–B_4C composites

To investigate the effect of deformation ratio on the mechanical properties Al–B_4C composites, the rolled plates with thicknesses of 13, 7, 4, and 2 mm, corresponding to a 58, 77, 87 and 93% reduction ratio respectively, were solutionized in an air furnace or an argon atmosphere furnace at 640 ºC for 24 h, quenched in water at room temperature and then aged at 300 ºC for 24 h in an air furnace. Moreover, to investigate the influence of the solution time on the mechanical properties of the composites, the 2 mm final plates were treated in an air furnace at 640 ºC for different times, quenched in water and then aged at 300 ºC for 24 h.

The 4 mm sheets with a total reduction ratio of 87 % are used for studying the precipitation hardening and thermal stability of Al–B_4C composites. After hot rolling, the composite sheets were solution-treated at 640 °C for different time, quenched to water at room temperature, and followed by the aging at 300 °C for 24 hours. To assess the

long-term thermal stability of mechanical properties, the heat-treated sheets were annealed at 300 °C up to 2000 hours.

3.4 Evaluation of mechanical properties

3.4.1 Hardness

Vickers microhardness was applied to evaluate the mechanical properties at ambient temperature of Al–B_4C composite in this research, performed on a QUALI TEST HVS–1000 Vickers' hardness tester. The tests were carried on a polished surface of specimens. According to the ASTM standard E92–16, the load is chosen to be 25 g and with 15 s of indentation, keep the size of impression in the range of 25–40 μm. 20 measurements were performed on the matrix of each sample. The mean value and standard deviation were calculated.

3.4.2 Compression test

Compression tests were applied to access the mechanical properties at elevated temperature of Al–B_4C composites in this research. The tests were performed on a Gleebe 3800 thermo-mechanical testing unit, as shown in Fig. 3.4, with a strain rate 10^{-3} s^{-1} to determine the 0.2 % offset yield strength (YS) at ambient and elevated temperatures based on ASTM E9-89a standard. The samples were deformed to a total trues train of 0.2. The dimensions of the cylindrical specimens for compression tests are 15 mm in length and 10 mm in diameter. An average value of yield strength was obtained from five compression tests.

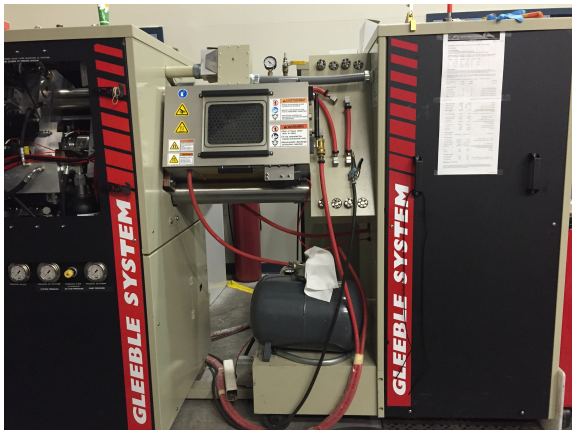

Fig. 3. 4. Gleebe 3800 thermo-mechanical testing unit.

3.4.3 Tensile test

Tensile properties are determined with a tensile testing machine according to the ASTM E8M-04 standard (tensile test at room temperature), and ASTM E21 standard (tensile test at 250°C and 300°C). Ultimate tensile strength (UTS), 0.2% yield strength (YS), and fraction strain (Elongation) were averaged over three tests for each condition. All tensile test samples with a thickness of 4 mm, overall length of 100 mm, and gage width of 6mm and gauge length of 25 mm were machined from the rolled composite plates based on ASTM E8M-04 standard.

3.5 Microstructure observation

3.5.1 Optical microscopy and sample preparation

The optical microstructures of the experimental composites were examined by optical microscope (Nikon Eclipse ME600). The samples were mounted and polished to 1 micron diamond suspension. The detailed preparation procedure of the optical sample is listed in

table 3.3. To reveal the grain boundaries of the matrix under optical microscope, polished samples were etched with a 0.5% HF solution. Grain size was evaluated following ASTM E112 standard.

Table 3. 4. Polishing procedure

Compound	Force (N)	Speed (round/m)	Time (min)	Lubricant
SiC sand paper 120 grit	30	120	5	Water
DP suspension 15 μm	30	120	10	DP Lubricant (red)
DP suspension 6 μm	30	150	10	DP Lubricant (red)
DP suspension 3 μm	20	150	10	DP Lubricant (red)
DP suspension 1 μm	15	150	15	DP Lubricant (red)
DP suspension 0.5 μm	5	120	3	Water

3.5.2 Scanning electron microscopy (SEM)

The microstructural features of the composites were observed by optical and a scanning electronic microscope (SEM, JSM-6480LV), equipped with an electron backscatter diffraction system (EBSD) and an energy dispersive spectrometer (EDS),

shown as Fig. 3.5. Moreover, the fractography of tensile test samples were examined by using the SEM.

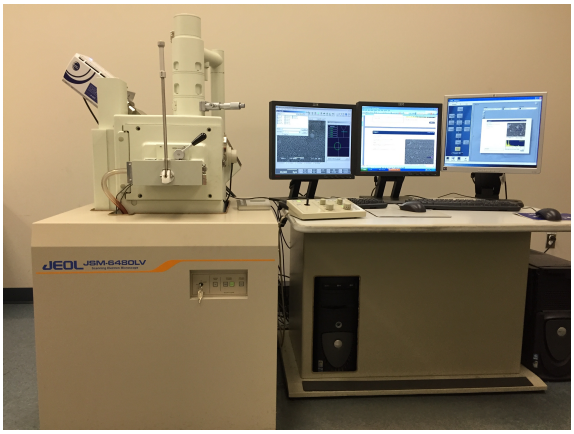

Fig. 3. 5. JEOL JSM-6480LV scanning electron microscope.

3.5.3 Transmission electron microscopy (TEM)

For TEM sample preparation, a 500-μm-thick specimen was first sliced from the composite samples, from which 3-mm-diameter discs were punched. TEM disc foils were prepared by metallographic grinding and polishing as well as dimpling (Fig. 3.6 (a)) followed by milling using a Gatan PIPS (Model 691) (Fig. 3.6 (b)).

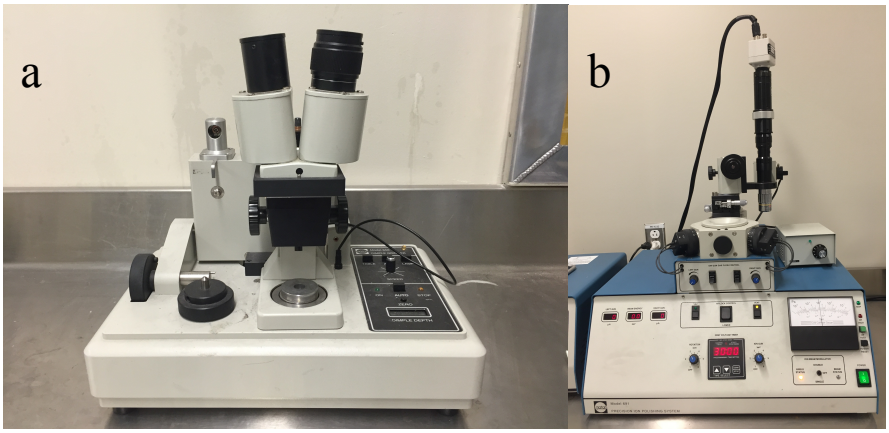

Fig. 3. 6. Gatan dimple machine (a) and Gatan PIPS (b).

The transmission electron microscope (TEM, JEM-2100) was employed to study the precipitation in Al−B_4C composites (Fig. 3.7). Centered dark-field images of the precipitates were recorded using the {100} superlattice reflections near the <011> direction on two-beam diffraction conditions. Convergent-beam electron diffraction (CBED) patterns were used to measure the thickness of the TEM specimens. The precipitate volume fractions and the equivalent diameters were determined using image analysis system on TEM images. To solve the precipitate overlap effect in TEM images, the method in Ref. [3] was used for the calculation of volume fraction.

Fig. 3. 7. JEM-2100 transmission electron microscope.

3.6 References

[1] Lai J, Zhang Z, Chen XG. Precipitation strengthening of Al–B4C metal matrix composites alloyed with Sc and Zr. Journal of Alloys and Compounds 2013;552:227.

[2] Lai J, Zhang Z, Chen XG. The thermal stability of mechanical properties of Al-B4C composites alloyed with Sc and Zr at elevated temperatures. Materials Science and Engineering a-Structural Materials Properties Microstructure and Processing 2012;532:462.

[3] Kelly PM. Quantitative electron microscopy. Metals Forum 1982;5:13~23.

CHAPTER 4

MECHANICAL PROPERTIES AND STRENGTHENING MECHANISMS OF Al–15%B_4C COMPOSITES WITH SC AND ZR AT ELEVATED TEMPERATURES

Chapter 4

Mechanical properties and strengthening mechanisms of Al–15%B_4C composites with Sc and Zr at elevated temperatures

4.1 Introduction

Al–B_4C metal matrix composites (MMCs) have been widely used as neutron absorber materials in the transport and storage of spent nuclear fuels in the nuclear industry because of the special capacity of B_4C for excellent neutron absorption [1, 2]. In service, the composites can be exposed at elevated temperatures 250−350 °C for extended periods of time, owing to the heat generation and accumulation by absorbing thermal neutrons from the spent fuels [1, 3]. To improve the overall performance of the neutron absorber materials, it is desirable to maximize the operating temperature and thermal stability of materials at

such high temperature. As the matrix of MMCs, most commercial precipitation strengthened 2xxx, 6xxx and 7xxx aluminum alloys are limited to be used below 200 °C. The mechanical properties of these matrices can be seriously deteriorated at higher temperature because of rapid coarsening of their precipitates (overaging effect) [4]. For precipitation-strengthened aluminum alloys, Al–Sc alloy is a rare exception, which can be used up to 300 °C because it can form nanoscale coherent Al_3Sc precipitates with a low coarsening rate [5]. Above this temperature, Al_3Sc precipitates may coarsen and lose coherency, which results in the degradation of mechanical properties of materials [6, 7]. It was reported that Zr could partially substitute Sc to form $Al_3(Sc_{1-x}Zr_x)$ precipitates with better coarsening resistance [8, 9], which improves the thermal stability of precipitates up to 350 °C [9] and increases the strength and recrystallization resistance [10-12]. Compared to Sc, Zr has lower diffusivity, and its substitution forms a shell at the α-Al/$Al_3(Sc_{1-x}Zr_x)$ interfaces, which inhibits Sc diffusion [13-15]. Moreover, Zr can decrease the lattice parameter of the Al_3Sc precipitates, which decreases the lattice parameter misfit [16]. Thus,

Zr decreases the coarsening rate of precipitates and benefits the thermal stability of materials [17].

In our previous works [18, 19], the mechanical properties of Al–B_4C (15–30 vol.% B_4C) MMCs without alloying at elevated temperatures have been investigated. The reinforcement of B_4C particles and their interfaces with Al matrix were very stable at high temperature. The presence of B_4C particles can provide an additional strengthening to Al matrix at both ambient and elevated temperatures. The strengthening mechanisms of reinforcements in MMCs can be divided into two categories, direct and indirect strengthening. The former refers to the load transfer from the weak matrix, across the matrix/reinforcement interface, to the higher stiffness reinforcement. And the latter involves dislocations accumulation around the reinforce particles due to the thermal expansion mismatch [20]. However, due to large particle size of B_4C particles (in the micrometer scale), their contribution to the overall composite strength was limited. To further improve the strength at elevate temperatures, the microstructure and mechanical

properties of Al–B_4C MMCs with Sc and Zr additions have been studied [7, 18, 19, 21]. To facilitate the manufacture of Al–B_4C composites, the addition of a certain amount of Ti was necessary to prevent the degradation of B_4C with liquid Al using a liquid-mixing process [22]. Ti could also significantly reduce the consumption of Sc and Zr in the interface reactions and enable most of the Sc and Zr amounts to be retained in the matrix for precipitation strengthening [23]. The results of our previous study [7] demonstrated that the yield strength at ambient temperature of Al–B_4C MMCs with Sc and Zr was thermally stable at 250–300 °C up to 2000 h. However, there is currently limited information available in the literature about the mechanical properties and their thermal stability at elevated temperatures (T > 0.5 Tm (the absolute melting temperature of the alloy)) of Al alloys and composites with Sc and Zr.

The present study examines the mechanical properties and their thermal stability of Al–B_4C MMCs with Sc and Zr addition at elevated temperatures (T > 0.5 Tm), particularly in the range of 250−350 °C, which are correlated with the microstructural evolution during

long-term thermal annealing. The study also aims to identify the governing strengthening mechanisms at elevated temperature and verify with experimental results, which will be used for future development of high-temperature, thermally stable Al-base MMCs.

4.2 Experimental procedure

Two experimental Al 1100–15 vol.% B_4C composites, namely S40 with 0.4 wt.% Sc and SZ40 with 0.4 wt.% Sc plus 0.24 wt.% Zr, were prepared for this investigation. In addition, an unalloyed Al 1100–15 vol.% B_4C composite without Sc and Zr as a base material was prepared to compare the effect of the precipitates on mechanical properties. Their nominal chemical compositions are listed in Table 4.1.

Table 4. 1. Peak aging and annealing parameters

Code	Aging		Annealing	
	T (K/°C)	Time (h)	T (K/°C)	Time (h)
S40	573 (300)	24	523 (250)	up to 2000
			573 (300)	up to 2000
SZ40	573 (300)	24	573 (300)	up to 2000
			623 (350)	up to 2000

In the composite melt preparation, commercial pure aluminum (99.7%) was first melted in an electric resistance furnace. The preheated master alloys, Al–2 wt.% Sc, Al–15 wt.% Zr, Al–10 wt.% Ti were then added into the aluminum liquid and held at 800 °C for 40 minutes to encourage the dissolution of master alloys. Prefabricated Al 1100–25 vol.% B_4C with 2.0 wt.% Ti cast ingots, supplied by Rio Tinto Alcan, were subsequently introduced into the alloyed melt. Ti is deliberately added to limit the Al/B_4C interface reaction during Al–B_4C composite preparation [22]. The average size of the B_4C particles (F360) was 23 μm. The composite melt was held at 740 °C for 30 minutes with mechanical

stirring to ensure a uniform distribution of B_4C particles in the melt, and then cast into a preheated permanent steel mold with a dimension of 30×40×80 mm.

To obtain the precipitation strengthening, the cast ingots of S40 were homogenized at 640 ºC for 24 h whereas SZ40 were treated at 640 ºC for 96 h, and then quenched in water at room temperature. The homogenized samples of S40 and SZ40 were aged at 300 ºC for 24 h, at which the hardness or yield strength of the composites reached the maximum values [21]. The applied heat treatment processes were based on our previous works [7, 21] and the peak aging paraments are listed in Table 4.2. The unalloyed Al 1100–15 vol.% B_4C samples (the base composite) were tested in the as-cast condition due to its non-heat-treatable nature. Moreover, to evaluate the long-term thermal stability, S40 and SZ40 samples on the peak aging condition were annealed at elevated temperatures (250 to 350 °C) up to 2000 hours (Table 4.2).

Table 4. 2. Peak aging and annealing parameters

Code	Aging		Annealing	
	T (°C)	Time (h)	T (°C)	Time (h)
S40	300	24	250	up to 2000
			300	up to 2000
SZ40	300	24	300	up to 2000
			350	up to 2000

Compression tests were performed on a Gleebe 3800 thermo-mechanical testing unit with a strain rate 10^{-3} s^{-1} to determine the 0.2% offset yield strength (YS) at ambient and elevated temperatures based on ASTM E9-89a standard. The samples were deformed to a total true train of 0.2. The dimensions of the cylindrical specimens for compression tests are 15 mm in length and 10 mm in diameter. An average value of yield strength was obtained from five compression tests. Vickers microhardness was also used to assess the mechanical properties at ambient temperature (25°C) with a load of 25 g and indentation time of 15 s on polished surface. A minimum of 20 measurements were performed on the

composite matrix of each sample, from which the mean value and standard deviation were calculated.

The microstructures of the experimental composites were examined by an optical microscope, a scanning electronic microscope (SEM, JSM-6480LV), and a transmission electron microscope (TEM, JEM-2100). For TEM sample preparation, a 500-μm-thick specimen was first sliced from the composite samples, from which 3-mm-diameter discs were punched. TEM disc foils were prepared by metallographic grinding and polishing as well as dimpling, followed by milling using a Gatan PIPS (Model 691). Centered dark-field images of the precipitates were recorded using the {100} superlattice reflections near the <011> direction on two-beam diffraction conditions. Convergent-beam electron diffraction (CBED) patterns were used to measure the thickness of the TEM specimens. The precipitate volume fractions and the equivalent diameters were determined using image analysis on TEM images. To consider the precipitate truncation effect in TEM images, the method in [24] was used for the calculation of volume fraction. To reveal the grain

boundaries of the matrix under optical microscoper, some of samples were polished and etched with a 0.5%HF solution. Grain size was evaluated following ASTM E112 standard.

4.3 Results

4.3.1 Microstructure characterization

Fig. 4.1 shows the typical microstructure of Al 1100–15 vol.% B_4C composites in an example of S40. The B_4C particles were uniformly distributed in the Al matrix (Fig. 4.1a), and particle clusters were rarely found. The Al matrix of the composites has all coarse grains, and the average grain sizes are approximately 100 μm in SZ40 and 130 μm in S40 at the peak aging condition. At high magnification (Fig. 4.1b), some small reaction-induced particles, which were generated during the melt preparation such as TiB_2, Al_3BC, ScB_2 and Al_3ScC (identified in [23]), are observed around the B_4C particles. During the long-term thermal annealing at the temperature range of 250−350 °C, the B_4C ceramic particles and

Al grains were notably stable. The variation of grain sizes for both S40 and SZ40 before and after 2000 h annealing was less than 0.8%.

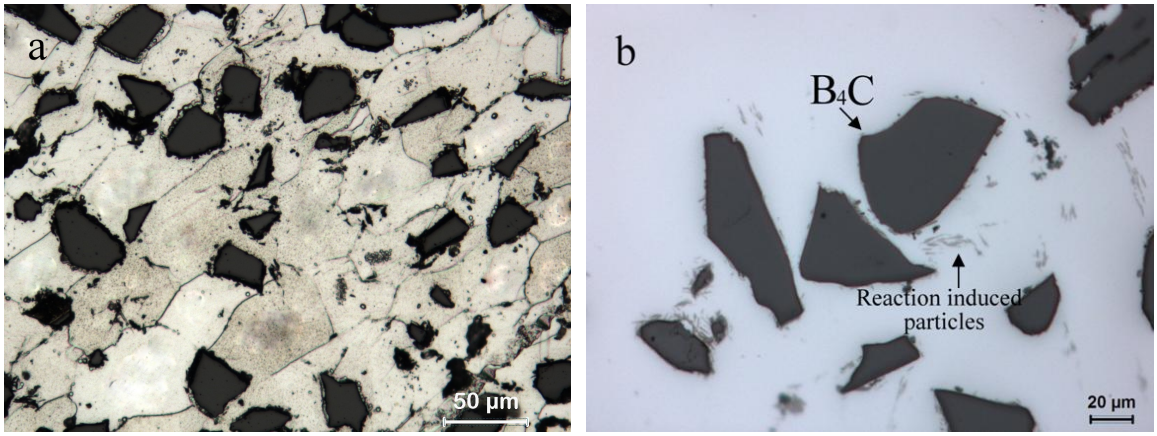

Fig. 4. 1. Optical microstructure of S40 composite at the peak aging: (a) low magnification and etched sample and (b) high magnification.

The precipitation evolution of the S40 and SZ40 composites under the peak aging condition and long-term annealing was examined using TEM. Fig. 4.2 shows representative TEM micrographs at different thermal-treatment conditions. At the peak aging condition (Figs. 4.2a and 4.2d), fine and coherent Al_3Sc and $Al_3(Sc, Zr)$ precipitates of S40 and SZ40 composites were formed in the Al matrix with a high number density. Most Al_3Sc and $Al_3(Sc, Zr)$ precipitates exhibit a spherical morphology and homogeneously distribute in the Al matrix. The volume fraction of the Al_3Sc precipitates in S40 is approximately 0.24%

with an average radius of 1.7 ± 0.7 nm, whereas the volume fraction of Al_3(Sc Zr) in SZ40 is approximately 0.33% with an average radius of 1.1 ± 0.32 nm.

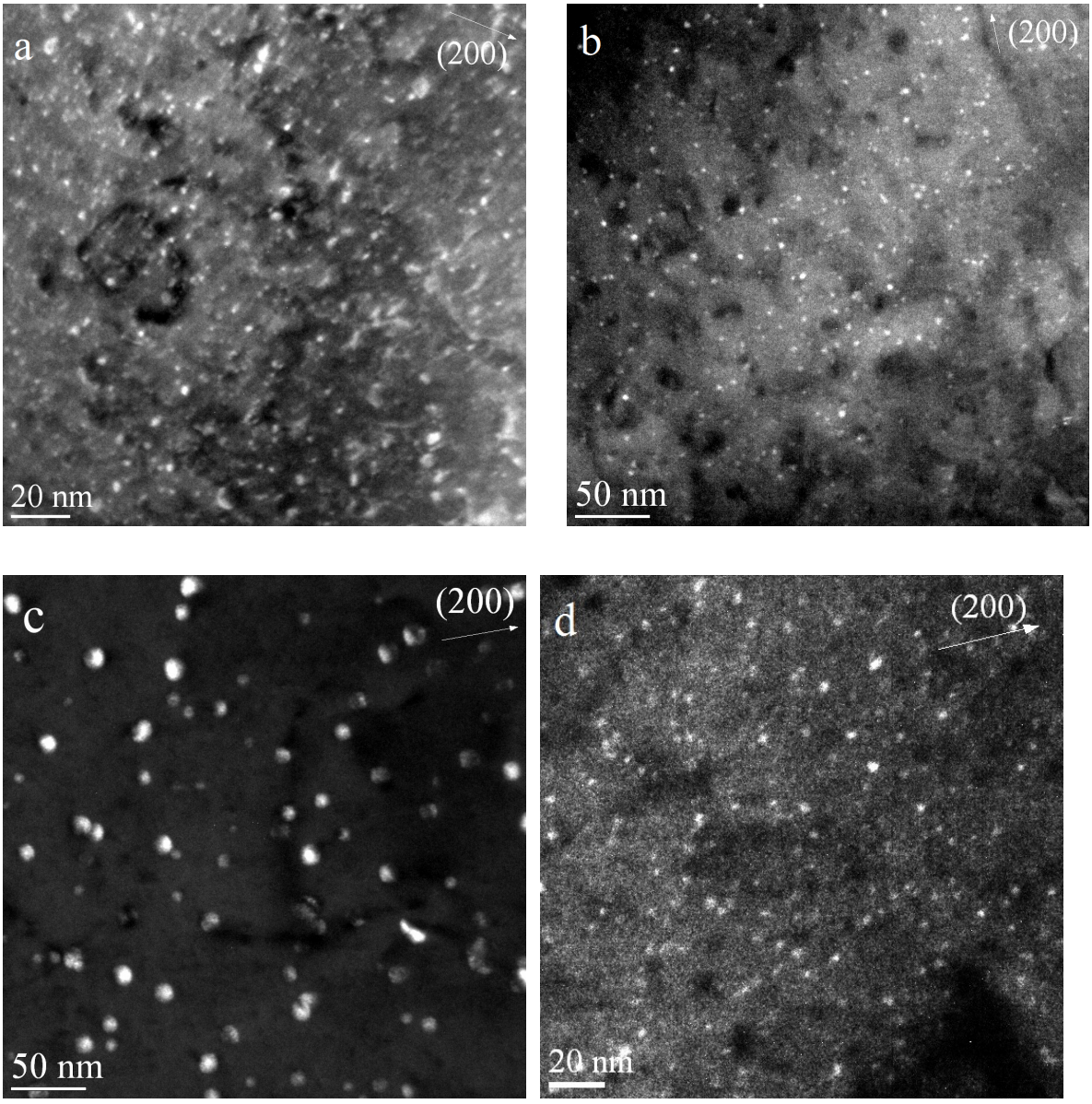

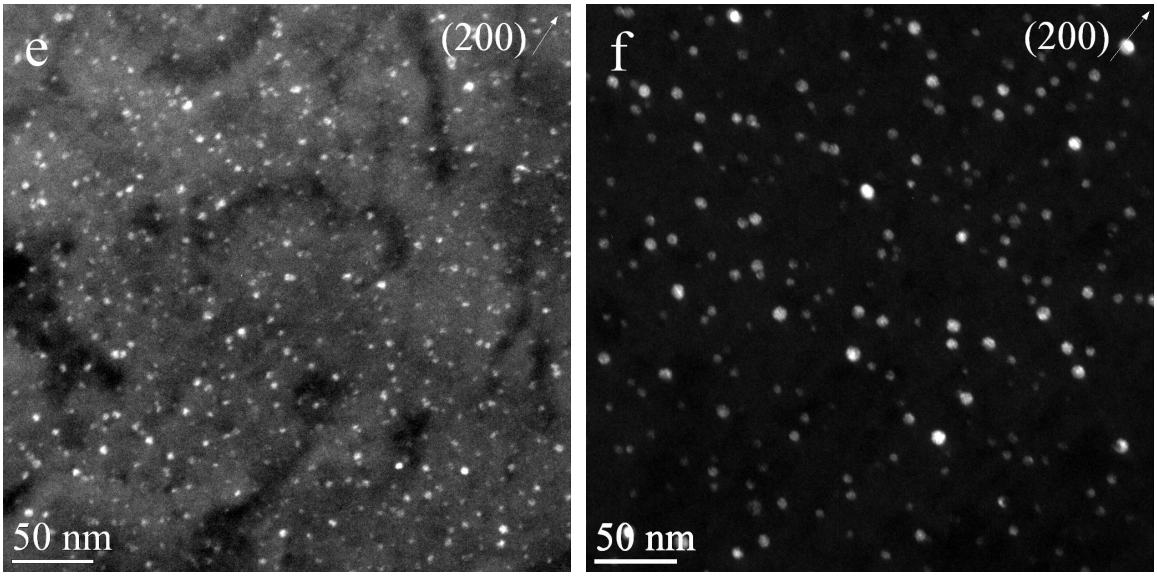

Fig. 4. 2. TEM dark field images showing precipitates: S40 on peak aging condition (a); 2000 h annealing at 250 °C (b); 2000 h annealing at 300 °C (c); SZ40 on peak aging condition (d); 2000 h annealing at 300 °C (e); and 2000 h annealing at 350 °C (f).

During the long-term annealing at high temperatures, precipitate coarsening can be observed. For the S40 composite, annealing at 250 °C for 2000 h yielded an average precipitate radius of only 2.1 ± 0.59 nm (Fig. 4.2b), whereas annealing at 300 °C for 2000 h yielded a precipitate radius of 6.1 ± 2.34 nm (Fig. 4.2c), which indicates that the precipitate coarsening in S40 only becomes obvious at 300 °C. Meanwhile, the average precipitate radius of the SZ40 composite is approximately 1.4 ± 0.32 nm after 2000 h at 300 °C (Fig.

4.2e), and it grows to 4.5 ± 1.48 nm after annealing at 350 °C for 2000 h (Fig. 4.2f). Fig. 4.3 shows the precipitate coarsening curves as a function of annealing time for both S40 and SZ40 composites. Compared to the Al_3Sc precipitates in S40, the $Al_3(Sc, Zr)$ precipitates in SZ40 exhibit a low coarsening rate even at higher temperatures. It is to notice that the standard deviation of Al_3Sc radius is larger than that of $Al_3(Sc, Zr)$ in Fig. 4.3, mainly due to high coarsening rate of Al_3Sc. The precipitate coarsening behaviors in both S40 and SZ40 composites can be described using Lifshitz-Slyozov-Wagner (LSW) equation [25-27]:

$$\overline{r}_t^3 - \overline{r}_0^3 = at \qquad \text{Eq. 4. 1}$$

where $\overline{r_o}$ is the mean initial precipitate radius, $\overline{r_t}$ is the precipitate radius at time *t*, and *a* is the coarsening rate constant, which is related to the temperature and material composition [16, 28, 29].

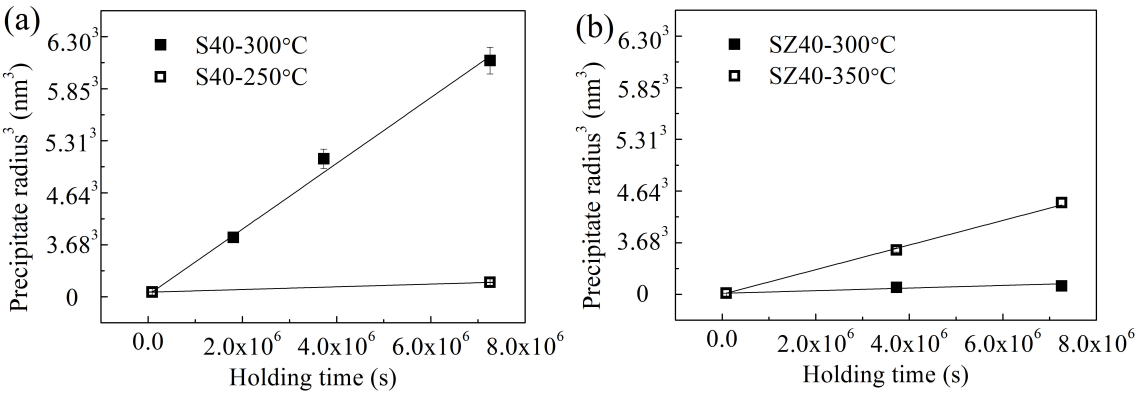

Fig. 4. 3. Precipitate coarsening as a function of annealing time at 250 °C and 300 °C for S40 (a) and at 300 °C and 350 °C for SZ40 (b).

The coarsening rate constants *a*, which are experimentally determined in Fig. 4.3, are 1.30×10^{-33} m^3s^{-1} at 250 °C and 3.16×10^{-32} m^3s^{-1} at 300 °C for the S40 composite. For the SZ40 composite, the constant values are 1.27×10^{-33} m^3s^{-1} at 300 °C and 1.19×10^{-32} m^3s^{-1} at 350 °C. The results imply that during prolonged exposure at elevated service temperatures, the Al_3(Sc,Zr) precipitates in SZ40 are more thermally stable and coarsening-resistant than the Al_3(Sc) precipitates in S40, which is confirmed by similar observations in other Sc– and Zr– containing aluminum materials [8, 21].

4.3.2 Mechanical properties as a function of temperature

The yield strengths of four different materials were evaluated at various temperatures, as showed in Fig. 4.4a. The true stress-train curves of three Al–15%B_4C MMCs obtained from compression tests are displayed in Figs. 4.4b–d, from which the 0.2% offset yield strengths are determined. All measured yield strengths are listed in Table 4.3. In general, the yield strength of aluminum, including the AA1100 alloy and the matrix of the base composite, decreases with the increase in test temperature mainly due to the decrease in aluminum shear modulus with increasing temperature [30]. The measured yield strength of the base Al-15%B_4C composite at ambient temperature is 46 MPa, which is approximately 12 MPa above that of the AA1100 alloy (commercially pure Al). With increased tested temperature, the increment of the yield strength of the base composite slightly decreases and remains about 10 MPa at 300 °C.

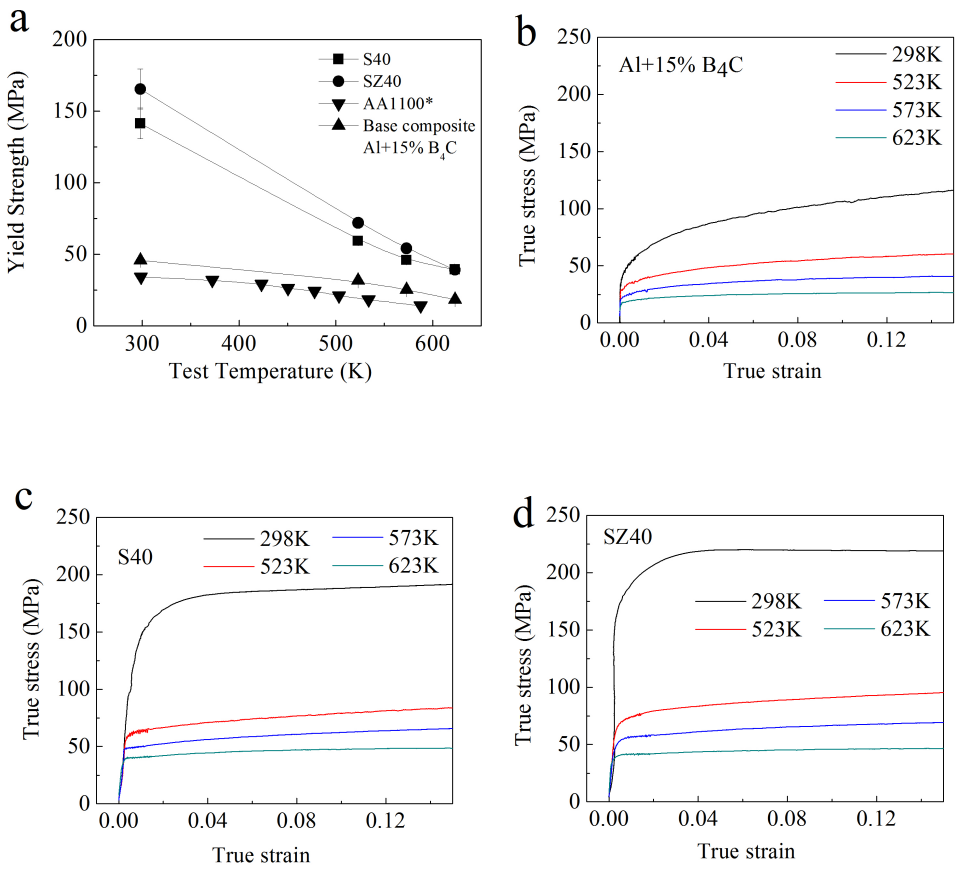

Fig. 4. 4. Yield strengths of S40, SZ40, the base composite (Al−15%B_4C) and AA1100 at various test temperatures. * The data of AA1100 are from the reference [4].

Table 4. 3. Yield strengths measured at different test temperatures

Test temperature (^{o}C)	Yield strength (MPa)		
	S40	SZ40	Base composite
25	141.3±10.8	165.4±13.9	45.8±1.1
250	59.3±1.6	71.9±2.6	31.6±0.9
300	46.0±1.9	54.0±1.6	25.2±2.0
350	39.3±1.1	39.2±1.6	18.4±0.5

Meanwhile, the composites alloyed with Sc (S40) and Sc and Zr (SZ40) have much higher strengths than the base composite, particularly at ambient temperature. The yield strengths of S40 and SZ40 are 141 MPa and 165 MPa, respectively, at ambient temperature. Precipitated during the aging treatment, the high number density of nanoscale precipitates Al_3Sc and $Al_3(Sc, Zr)$ effectively strengthens the composites at ambient temperature. At

elevated temperatures (250−350°C), the yield strength dramatically decreases with increasing temperature. For example, at 300 °C, the yield strengths of S40 and SZ40 are reduced to 46 and 54 MPa, respectively. SZ40 generally has higher yield strength than S40 mainly because of a higher volume fraction of precipitates.

It should be mentioned that even at high temperatures (250−350°C), the yield strengths of S40 and SZ40 are still much higher than that of the base Al–15%B_4C composite. It indicates that Al_3Sc and Al_3(Sc, Zr) precipitates in Al matrix provide the predominate contribution to the overall composite strength. The presence of large B_4C particles in the tens micrometers can only moderately contribute to the composite strength, which is mainly attributed to the load transfer from the soft matrix onto the hard reinforcement and dislocation accumulation around reinforce particles due to thermal expansion mismatch between the matrix and the reinforcement particles [31].

The overall strength σ_t of a material, which includes various characteristic strength increment $\Delta\sigma_i$, can be described by the empirical Eq. (2) with an exponent $1 \leq k \leq 2$ [32].

$$\sigma_t^k = \sum_t \Delta\sigma_i^k \qquad \text{Eq. 4. 2}$$

For Al–B_4C composites with Al_3Sc and $Al_3(Sc, Zr)$ precipitates, the precipitate strength increments can be calculated using Eq. 4.3:

$$\Delta\sigma_p = \left(\sigma_t^k - \sigma_{Al+15\%B_4C}^k\right)^{1/k} \qquad \text{Eq. 4. 3}$$

where σ_{Al+B_4C} is the strength contributed by the unalloyed Al−15%B_4C composite, and $\Delta\sigma_p$ is the strength increment attributed to the precipitates. It has been reported that k is equal to 1 for an Al−2 wt.% Mg alloy that was strengthened by nanoscale Al_3Sc precipitates [33]. In the present study, we adapted k=1 to calculate all yield strength increments contributed by precipitates.

4.3.3 Thermal stability during long-term thermal holding

The mechanical properties at ambient temperature after long-term thermal holding at various temperatures were evaluated using Vicker's hardness measurement (Fig. 4.5). The results in Fig. 4.5 show that the microhardness of two Sc– and Zr– containing composites

remains notably stable up to 2000 h at lower exposure temperatures (250 °C for S40 and 300 °C for SZ40), whereas the microhardness of both materials remarkably decreases with prolonged holding time at higher exposure temperatures (300 °C for S40 and 350 °C for SZ40). For example, the microhardness of the S40 composite at 300 °C decreases after 500 h of holding, and its value decreases from 65 HV at the beginning of holding to 54 HV after 2000 h of holding.

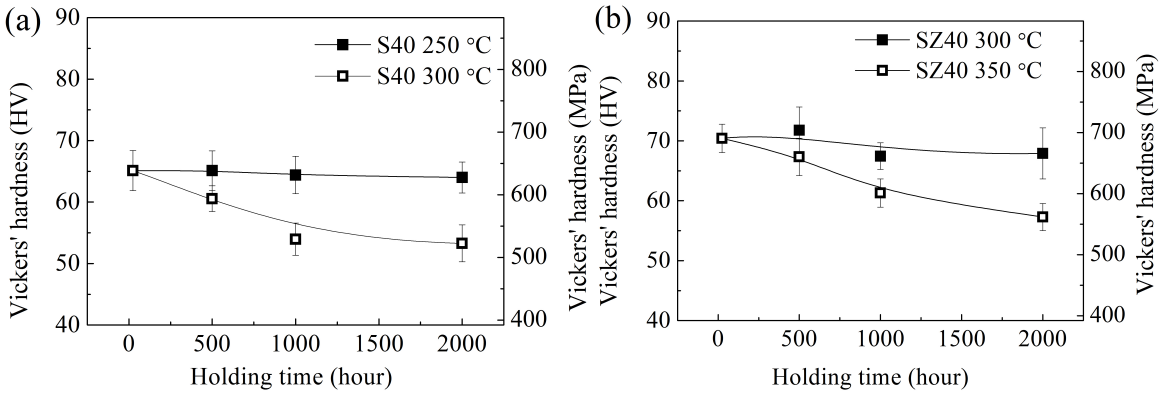

Fig. 4. 5. Vickers microhardness, measured at ambient temperature, after the composites annealed at elevated temperatures for different holding time: (a) S40 and (b) SZ40.

At lower exposure temperatures, the precipitates in both composites (Al_3Sc in S40 and $Al_3(Sc, Zr)$ in SZ40) exhibit notably limited coarsening (Fig. 4.3); thus, both composites

exhibit excellent softening resistance (up to 250 °C) for S40 and 300 °C for SZ40). At higher exposure temperatures, the Al_3Sc and $Al_3(Sc, Zr)$ precipitates slowly coarsen with time, which weakens the material strength and causes the progressive softening during the prolonged thermal holding. A similar tendency of the mechanical properties of Al–B_4C composites with Al_3Sc and $Al_3(Sc, Zr)$ precipitates at ambient temperature was also observed in the previous study [7]. It is also evident that the addition of Zr into the Sc–containing composite improves the softening resistance and delays the material softening towards higher temperature.

To evaluate the mechanical properties at elevated temperatures, compression tests were performed at the same temperatures as the sample-annealing temperatures. Fig. 4.6a shows the yield strength of S40 as a function of the holding time at two tested temperatures. At both temperatures (250 and 300 °C), the yield strength first increases in the initial 500 h and tends to stabilize up to 2000 h. The yield strength of SZ40 remains unchanged from the beginning of holding till 2000 h at 300 and 350 °C (Fig. 4.6b). At lower exposure

temperatures during annealing, both precipitates in S40 and SZ40 were practically stable against coarsening (Fig. 4.3). Thus, the yield strength at elevated temperatures remains stable during the entire annealing period (2000 h). However, at higher exposure temperatures (300 °C for S40 and 350 °C for SZ40), the Al_3Sc and $Al_3(Sc, Zr)$ precipitates in both composites coarsened with prolonged holding time. It is surprising to observe constant and stable yield strengths at such high temperatures. On the other hand, for long-term service as neutron absorber materials, the Al–B_4C composite with Sc (S40) can generally sustain stresses on the order of 50 MPa at $0.61T_m$ (300 °C), while the SZ40 composite can be further operated under stresses on the order of 40 MPa at $0.67T_m$ (350 °C).

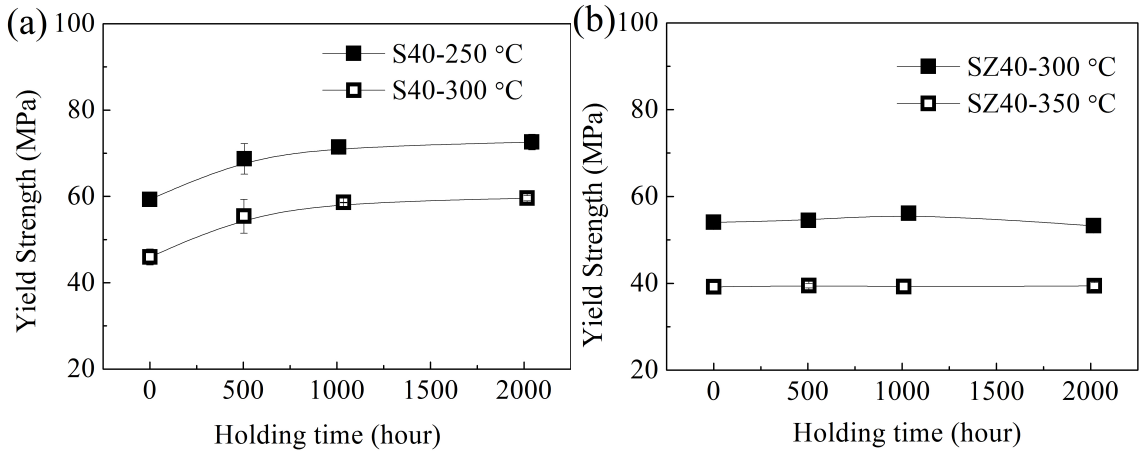

Fig. 4. 6. Yield strength, measured at the same elevated temperature as the annealing temperature, as a function of annealing time: (a) S40 and (b) SZ40.

Based on the results of mechanical properties at various temperatures and their evolution during long-term thermal holding, a few interesting phenomena are observed: (1) the yield strength increment of two composite materials dramatically decreases with increasing test temperature; (2) during the long-term holding at high temperatures (300 °C for S40 and 350 °C for SZ40), the mechanical properties at ambient temperature of the two composites gradually decrease with prolonged holding time because the Sc– and Zr–containing precipitates coarsen; (3) the mechanical properties at elevated temperatures remain thermally stable during 2000 h annealing and independent from the coarsening of

Sc– and Zr– containing precipitates, unlike those tested at ambient temperature. This information suggests that the strengthening mechanisms of the precipitates can be different at ambient and elevated temperatures. To understand the mechanical properties at various temperatures and their thermal stability at high temperature, the possible strengthening mechanisms are outlined and discussed below.

4.4 Discussion

4.4.1 Strengthening mechanisms

For precipitation-strengthened materials that are operated at elevated temperature, both the ambient-temperature strength and high-temperature strength are essential for the overall performance of materials. The ambient-temperature strength can be generally explained and predicted by classical precipitate shearing and Orowan bypassing mechanisms [10, 17, 21, 30, 32, 34]. It is known that for a precipitate, which has a size smaller than the critical radius and has coherent structure with matrix, the strength is controlled by precipitate

shearing, whereas for large precipitate sizes the Orowan dislocation bypass mechanism controls the strength. At elevated temperature, there is sufficient thermal energy to allow dislocation circumventing the precipitates by climbing. The dislocation climb mechanism may become active when deformed at elevated temperature with low strain rates because the vacancy diffusion becomes significant at temperature above $0.5T_m$ [35, 36]. Miura et al. [37] used the dislocation climb to explain the tensile deformation behavior of an Al-Sc alloy at temperatures between 25 °C and 250 °C. To explain the creep properties of Al-Sc alloys at elevated temperature, Marquis *et al.* [30, 35] introduced a dislocation climb mechanism and developed a model to predict the creep threshold stresses.

4.4.1.1 Dislocation climb mechanism

In precipitate-strengthened Al alloys, the interaction between the dislocation and the matrix mainly includes: (1) modulus mismatch; (2) lattice mismatch (coherency strengthening); and (3) order strengthening [10, 32, 34, 35]. For coherent precipitates, the repulse stress for dislocation climbing is caused by the elastic interaction between the

dislocations and the precipitates [35]. The components of the elastic reaction are due to lattice mismatch and modulus mismatch [34, 35]. Therefore, the strength increment caused by dislocation climb strengthening, $\Delta\sigma_C$, is the sum of $\Delta\sigma_{LMC}$ and $\Delta\sigma_{MMC}$, which are the strength increments of lattice mismatch and modulus mismatch, respectively.

To calculate $\Delta\sigma_{MMC}$, the force F that acts on the dislocation must be determined. Based on a model proposed by Marquis and Dunand for dislocation climbing over a coherent precipitate at elevated temperature [34, 35], a schematic of a dislocation at an initial location to climb over a precipitate is shown in Fig. 4.7. In fact, most of the Al_3Sc and $Al_3(Sc, Zr)$ precipitates exhibit a spherical morphology (Fig. 4.2). However, due to its complexity, there is no direct analytical solution for spherical morphology available in literature. A cylindrical form was selected [35, 38], because there is an analytical solution for a unit length of a straight dislocation to describe the interaction energy between a dislocation and an infinitely long cylinder, developed by Dundurs [39]. A cylinder-like particle with $2r$ in diameter and $2r$ in length (r is the cylinder radius) is taken as an

approximation of a spherical particle (Fig. 4.7). The edge dislocation is at a distance, r+nb, away from the precipitate center; where b is the magnitude of the matrix burgers vector and n is a variable number which should be larger than 0.5 [35]. The dislocation position is determined by $y=cos\theta(r+nb)$ and $z_0+h=sin\theta(r+nb)$; where h is the distance between the dislocation glide plane and precipitate center, z_0 is the height of the dislocation segment climbed above its glide plane as shown in Fig. 4.7b and θ is the angle between the coordinate origin plane and the plane composed of the climbed dislocation segment. Based on the interaction energy for a unit length of an edge dislocation, the force between particles and dislocations can be calculated using Eq. 4.4 [39]:

$$F=-r\left(\frac{\partial E}{\partial y}\right)=\frac{G_m b^2}{\pi\left(k_m+1\right)\left(1-\beta^2\right)}\left\{\begin{array}{l}2\left(\alpha+\beta^2\right)\dfrac{r^3\cos\theta}{\left(r+nb\right)\left[\left(r+nb\right)^2-r^2\right]\ln^{10}}\\-\left[\alpha+\beta^2-2\left(1+\alpha\right)\beta\right]\dfrac{2r^3\cos\theta\left(\cos^2\theta-\sin^2\theta\right)}{\left(r+nb\right)^3}\\-\left(1+\alpha\right)\left[1-\beta-\dfrac{\left(1-\alpha\right)\left(1+\beta\right)}{1+\alpha-2\beta}\right]\dfrac{2r^3\cos\theta\sin^2\theta}{\left(r+nb\right)^3}\end{array}\right\} \qquad \text{Eq. 4. 4}$$

E is the interaction energy for a unit length of an edge dislocation with precipitates [39]. According to Eq. 4.4, the force opposing dislocation glide is the greatest at $\theta=0$, i.e. $z_0+h=0$. Here, the initial position of a dislocation to climb a precipitate with a maximum repulsion force is at $\theta=0$ with a distance y=r+nb as shown in Fig. 4.7, and this dislocation initial position is applied for the prediction of mechanical properties in the study.

The dislocation is away from a precipitate with a distance y, and the expressions of α and β are as follows:

$$\alpha = \frac{\Gamma\left(k_m+1\right)-\left(k_p+1\right)}{\Gamma\left(k_m+1\right)+k_p+1} \qquad \text{Eq. 4. 5}$$

$$\beta = \frac{\Gamma\left(k_m-1\right)-\left(k_p-1\right)}{\Gamma\left(k_m+1\right)+k_p+1} \qquad \text{Eq. 4. 6}$$

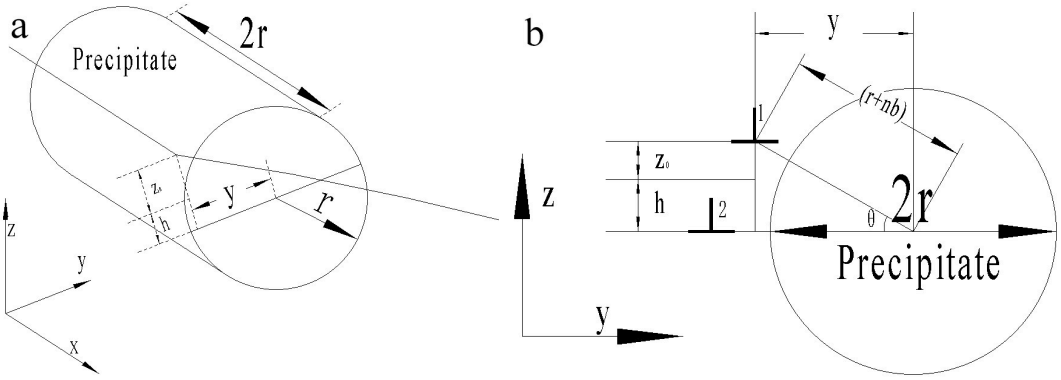

Fig. 4. 7. Three-dimensional schematic showing an edge dislocation to climb a particle (a) and the side view (b). The dislocation 1 is located at the position: $z=z_0+h$ and $y=cos\theta(r+nb)$, and the dislocation 2 is on the position with a maximum repulsion force.

G_m and G_p are the shear moduli of the matrix alloy and precipitates, respectively. The modulus mismatch parameter is defined as $\Gamma=G_m/G_p$; the Poisson parameters are: $k_m=3\text{-}4\nu_m$ and $k_p=3\text{-}4\nu_p$, where ν is Poisson's ratio, and the subscripts m and p refer to the matrix and the particle, respectively [35, 39].

The critical resolved shear stress (CRSS) is described as [27]:

$$\tau = \frac{F^{\frac{3}{2}}}{\left(\frac{G_m b^2 2\pi}{3f}\right)^{\frac{1}{2}} br} \qquad \text{Eq. 4. 7}$$

where f is the volume fraction of precipitates, then, the contribution of the modulus mismatch is [27]:

$$\Delta\sigma_{MMC} = M\tau = \frac{MF^{\frac{3}{2}}}{\left(\frac{G_m b^2 2\pi}{3f}\right)^{\frac{1}{2}} br} \quad \text{Eq. 4. 8}$$

Here, M is the mean matrix orientation factor, for aluminum, M=3.06 [40]. The contribution of the lattice mismatch is [27, 41]:

$$\Delta\sigma_{LMC} = \chi M\left(\varepsilon G_m\right)^{3/2}\sqrt{\left(2fbr/G_m b^2\right)} \quad \text{Eq. 4. 9}$$

where χ=2.6 is a constant [27], and ε is the constrained strain. Here ε is [30]:

$$\varepsilon \approx \frac{2}{3}|\delta| \quad \text{Eq. 4. 10}$$

and,

$$\delta = \frac{a_p - a}{a} \quad \text{Eq. 4. 11}$$

where δ is related to the difference between the lattice parameters a_p and a_m of precipitate and matrix, respectively. The lattice parameter at 25 °C is 0.4049 nm for Al and 0.4103 nm for Al_3Sc [16].

4.4.1.2 Orowan bypass mechanism

Orowan proposed the following strengthening mechanism: a dislocation loop appears around each particle when a dislocation bypasses precipitates [42]. This mechanism usually is operative for precipitates with larger sizes [21, 30]. The contribution in yield strength $\Delta\sigma_O$ due to this mechanism is determined by Eq. 4.12 [40]:

$$\Delta\sigma_O = \frac{0.4\,MG_m b \ln\left(\frac{2r}{b}\right)}{\pi\sqrt{1-\nu_m}\,\lambda} \qquad \text{Eq. 4. 12}$$

where λ is the inter-precipitate distance, which is [32]:

$$\lambda = \left[\left(\frac{3\pi}{4f}\right)^{1/2} - 1.64\right] r \qquad \text{Eq. 4. 13}$$

4.4.1.3 Shearing mechanism

For coherent precipitates with small sizes, the strength is controlled by the shearing mechanism, where a dislocation cuts and bypasses the precipitate. The precipitate strengthening has three main contributions: (i) modulus mismatch; (ii) lattice mismatch, and (iii) order strengthening. The strength increment $\Delta\sigma_s$, which is attributed to the shearing mechanism, is taken as the maximum value of modulus and lattice mismatches or the order strengthening [10]. Thus, they are described as follows [27]:

$$\Delta\sigma_{OS} = 0.81M\frac{\gamma_{apb}}{2b}\left(\frac{3\pi f}{8}\right)^{1/2} \quad \text{Eq. 4. 14}$$

where $\Delta\sigma_{os}$ is the strength increment from order strengthening. γ_{apb} is the antiphase boundary (APB) energy per unit area on the slip plane, and $\gamma_{apb}\approx 0.5J/m^2$ [43-45].

$$\Delta\sigma_{MMS} + \Delta\sigma_{LMS} = 0.0055M\Delta G^{3/2}\left(\frac{2f}{G_m b^2}\right)^{1/2} b\left(\frac{r}{b}\right)^{\frac{3m}{2}-1} + \chi M\left(\varepsilon G_m\right)^{3/2}\sqrt{\left(2fbr/G_m b^2\right)}$$

Eq. 4. 15

Here, $\Delta\sigma_{MMS}$, and $\Delta\sigma_{LMS}$ are the contributions of the modulus mismatch and lattice mismatch to the strength increment in the shearing mechanism, respectively; *m* is a constant value of 0.85 [27].

4.4.2 Strengthening at ambient temperature

Fig. 4.8 shows the theoretical yield stresses at ambient temperature as a function of the precipitate size for both S40 and SZ40 composites based on the precipitate shearing and Orowan bypass mechanisms. The parameters in the calculation are listed in Table 4.4. In the theoretical stress curves, the yield strength sharply increases with the increase in precipitate size, when the shearing mechanism controls the process for the precipitate that is smaller than the critical value (~2 nm), but the strength decreases with increasing precipitate size when the Orowan mechanism is dominant for the precipitate with radius larger than 2 nm.

Table 4. 4. Constants used in the calculations.

T (°C)	G_m[1*] (GPa)	G_p[2*] (GPa)	b[3*] (Å)	δ-S40[4*]	δ-SZ40[4*]	ν_m	ν_p
25	25.4 [16]	69 [46]	2.86[16]	1.34%[16]	1.07%[16]		
250	22.4	66.8	2.87	1.17%	0.90%		
						0.34[46]	0.2[43]
300	21.1 [16]	66.2	2.88	1.14%	0.87%		
350	21.0	65.7	2.88	1.10%	0.83%		

[1*] Temperature dependence of the shear modulus is given by −13.6 MPa·K^{-1} for Al [47].

[2*] Temperature dependence of the Young's modulus is given by −26 MPa·K^{-1} [48].

[3*] Thermal expansion coefficient value of Al is 24.7×10^{-6} K^{-1} [29].

[4*] Thermal expansion coefficient value of 16×10^{-6} K^{-1} for Al_3Sc [16].

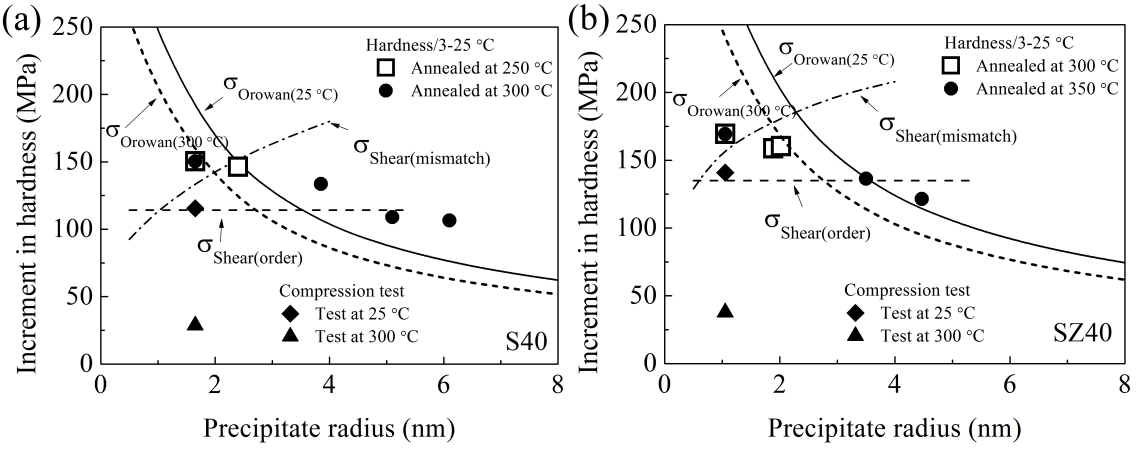

Fig. 4. 8. The calculated (shearing and Orowan mechanisms) and experimental strength data at 25 °C as a function of mean precipitates for S40 (a) and SZ40 (b). The measured values in strength increments at elevated temperatures (300 °C) are also included for comparison.

The measured increments in yield strength at ambient temperature are included in Fig. 4.8. The data points were obtained from the compression tests and microhardness measurements using the relationship $\Delta\sigma_p \approx HV/3$ [49]. For the S40 and SZ40 samples at the peak aging condition, the experimental stress values were fitted in the shearing mechanism zone because the precipitate size is notably small. For the samples that were annealed at elevated temperatures (250−350 °C) and tested at ambient temperature, the Orowan mechanism controlled the process when the precipitates grew above the critical radius. The experiment and theoretical prediction values are consistent for all samples tested at ambient temperature.

The measured yield strength increment at 300 °C is exemplary included in Fig. 4.8 for comparison. As anticipated, the yield stress is considerably lower at 300 °C than at ambient temperature. For both S40 and SZ40 samples at the peak aging condition and

tested at elevated temperatures, the precipitate sizes remain notably small (1−2 nm), but the measured yield stress values are at least one order of magnitude lower than the theoretical values. Therefore, the shearing mechanism can be excluded as an operative strengthening mechanism at elevated temperature. In the Orowan bypass mechanism (Eq. 4.12), the decrease in strength with increasing temperature may arise from the temperature dependence of the shear modulus G_m. Considering that G_m decreases from 25.4 GPa at ambient temperature to 21.1 GPa at 300 °C for aluminum matrix (Table 4.4), the modified Orowan stress curve at 300 °C as a function of the precipitate size is also included in Fig. 4.8. The Orowan stress at 300 °C is generally shifted to a lower value than that at ambient temperature. However, the measured yield strength at 300 °C remains much lower than the predicted ones, which indicates that the classical Orowan bypass mechanisms cannot predict the precipitate strengthening effect at elevated temperature, and another strengthening mechanism should be involved.

4.4.3 Strengthening at elevated temperatures

A dislocation climb mechanism is invoked to explain the deformation at elevated temperatures (> $0.5T_m$) [35, 36]. Fig. 4.9 shows the theoretical yield stresses as a function of precipitate size at 300 °C with S40 (0.24 vol.% Al_3Sc) as an example based on the dislocation climb and Orowan bypass mechanisms (Eqs. 4.8-4.13). The parameters in the calculation are listed in Table 4.4, and the climb stresses are calculated using the distance y from $r+2b$ and $r+5b$ as the upper and lower boundaries, respectively. At elevated temperatures, the dislocation climb mechanism operates at stresses lower than the Orowan ones for an alloy with small and intermediate-sized precipitates (1-8 nm in radius). The strength increases with increasing precipitate size, which shows a contrary tendency to the Orowan mechanism in this size range. The predicted critical value of the precipitate radius is approximately 8 nm for the $r+5b$ distance. For the large precipitate size (> 8 nm), the Orowan mechanism is dominant again.

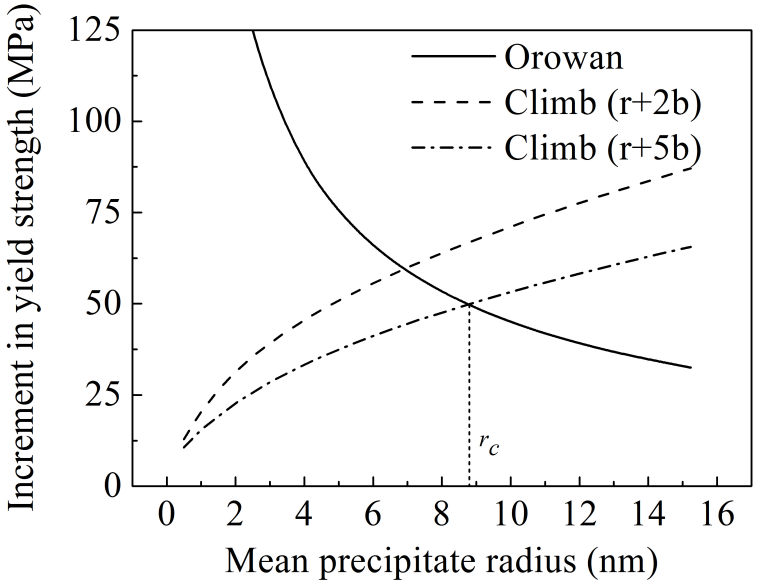

Fig. 4. 9. Theoretical calculation of yield stresses based on the models of dislocation climb and Orowan mechanisms for S40 (0.24 vol.% Al_3Sc) at 300 °C as a function of precipitate radius. The distance, y=*r*+2*b* or *r*+5*b*, are used in the dislocation climb model (see Fig. 4.7).

In the dislocation climb model, the distance *y* between a precipitate center and a dislocation (see Fig. 4.7 and Eq. 4.4) represents the initial point of a dislocation to climb a precipitate. In this study, the unit of the distance is considered the Burgers vector of aluminum matrix, *b*. In general, the distance required to climb a precipitate increases with the increasing temperature because the vacancy density in materials increases at higher temperature, which results in a lower energy required for the dislocation climb [42].

Moreover, the increase in precipitate size may lead to an increase in climb distance [38], which is related to the increased repulsive stress to a dislocation (Eqs. 4.4-4.9). However, the precipitates Al_3(Sc, Zr) have less lattice misfit (1.07%) with aluminum matrix than Al_3Sc (1.34%, see Table 4.4), which leads a lower strain field around the precipitate and consequently a lower y value. Thus, for S40, the distance y for the strength calculation is taken from r+2b to r+5b. For SZ40, considering the smaller precipitate size and less lattice misfit, the distance value is taken from r+b to r+2b when the precipitates are in the peak aging condition or limited coarsening (< 2 nm in radius), but the distances from r+2b to r+5b are used for the calculation to predict the strength at 350 °C, where the precipitate coarsening becomes obvious.

In fact, the size distribution of the precipitates varies over a wide range, particularly during the coarsening process. Fig. 4.10 shows an example of the precipitate size distribution of S40 after annealing at 300 °C for 2000 hours. The particle size ranges from 1 nm up to 14 nm. It is worth mentioning that the critical coherent radius of Al_3Sc

precipitates is around 15 nm [50] and the discussion below is based on the coherent precipitates. The increment of yield strength due to different precipitate sizes will be determined by the combination of dislocation climb and Orowan mechanisms at elevated temperature (see Fig. 4.10).

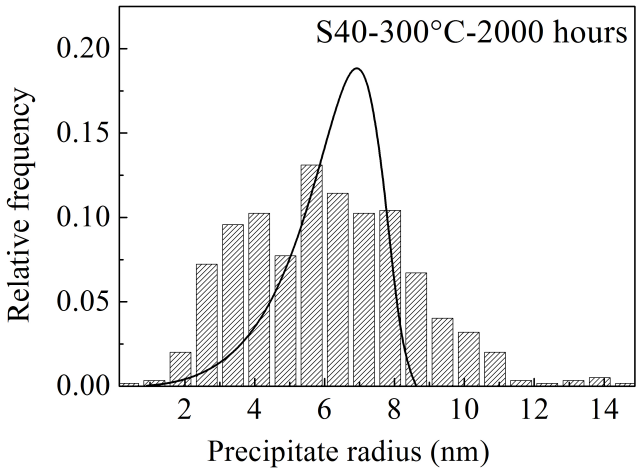

Fig. 4. 10. Precipitate size distribution and LSW simulation in S40 annealing at 300 °C for 2000 h.

Because the precipitate coarsening behaviour generally follows Lifshitz−Slyozov−Wagner **(**LSW) function (see Figs. 4.3 and 4.10), the density function of the particles in a material, $f\left(\frac{r}{\bar{r}}\right)$, can be expressed as [25, 26, 51]:

$$f\left(\frac{r}{\bar{r}}\right)=\frac{4}{9}\left(\frac{r}{\bar{r}}\right)^{2}\left(\frac{3}{3+\frac{r}{\bar{r}}}\right)^{7/3}\left(\frac{1.5}{1.5-\frac{r}{\bar{r}}}\right)^{11/3}e^{\left(\frac{\frac{r}{\bar{r}}}{\frac{r}{\bar{r}}-1.5}\right)};0<\frac{r}{\bar{r}}<1.5 \qquad \text{Eq. 4. 16}$$

$$f\left(\frac{r}{\bar{r}}\right)=0;\frac{r}{\bar{r}}\geq 1.5 \qquad \text{Eq. 4. 17}$$

where r is the actual precipitate radius, and $\bar{r}$ is the mean precipitate radius. Because the function of dislocation climbing and Orowan bypass mechanisms are in parallel, strengthening is given by the smaller one of these two strengthening models. Then, the precipitate strengthening contribution of the two mechanisms can be described as follows:

$$\Delta\sigma_{p}=\int_{0}^{r_{c}}\Delta\sigma_{c}(r)f\left(\frac{r}{\bar{r}}\right)dr+\int_{r_{c}}^{1.5\bar{r}}\Delta\sigma_{O}(r)f\left(\frac{r}{\bar{r}}\right)dr \quad \text{Eq. 4. 18}$$

Both calculated increments in yield stresses (Eq. 4.18) and experimental data of S40 and SZ40 at elevated temperatures are shown as a function of the precipitate size in Fig. 4.11. The yield strength increments of the S40 samples, which were annealed and tested at 250 ºC, are located in the calculated dislocation climbing zone using $y = r+2b$ (Fig. 4.11a). In this zone, the strength increases with increasing precipitate size. When the samples were

annealed for 2000 h and tested at 300 ºC, (0.61T_m), four experimental data points belonged to the dislocation climb zone with the r+2b and r+5b distance (Fig. 4.11b). At this temperature, the precipitates were coarsening. The mean Al_3Sc precipitate radius increases from 1.7 nm at the peak aging to 6.2 nm after 2000 h of annealing, which results in the shift of the dislocation climb distance from r+2b to r+5b. Thus, the yield strength of S40 at 300 ºC slightly increases in the first 500 h of annealing and subsequently remains more and less stable (Fig. 4.6a).

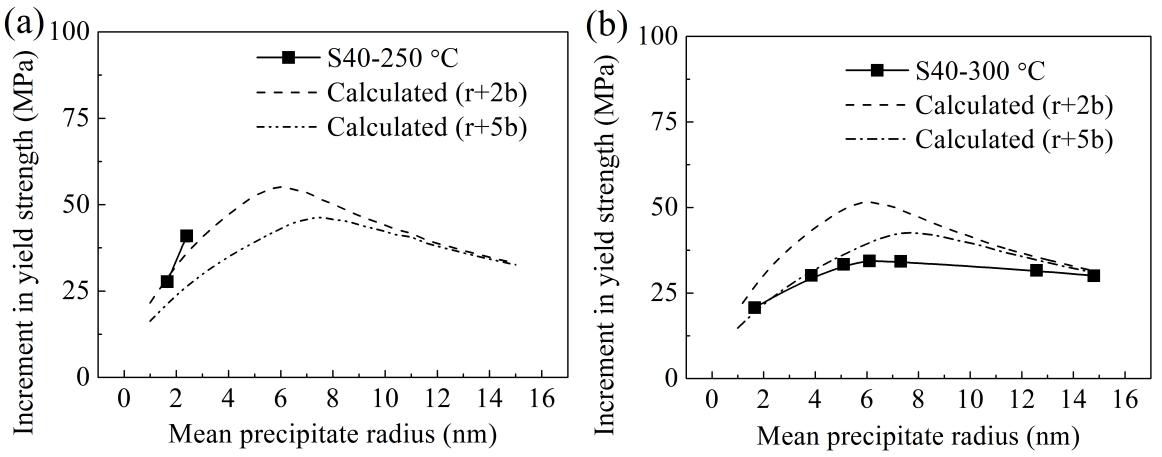

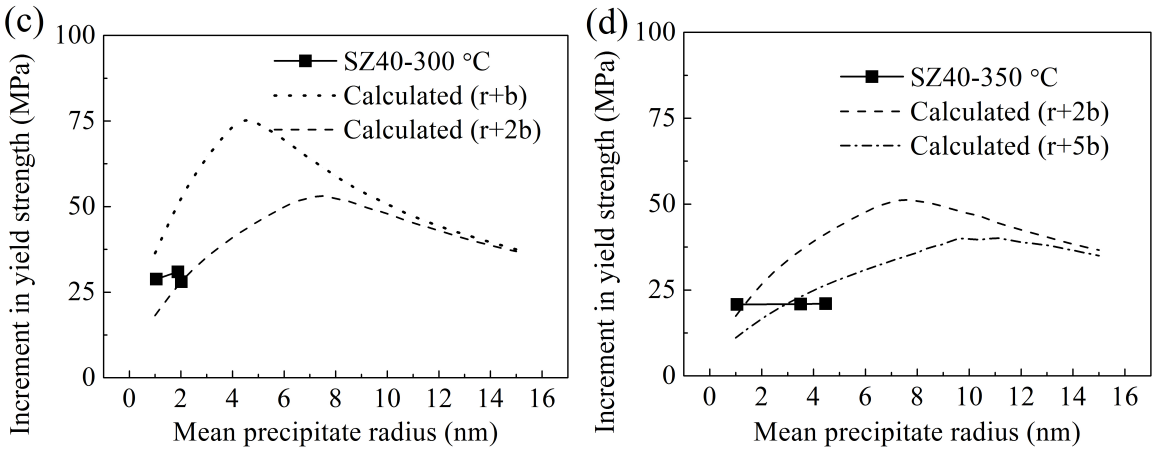

Fig. 4. 11. The calculated yield strength increments and experimental strength data as a function of the mean precipitate radius: for S40 at 250 °C (a) and 300 °C (b); for SZ40 at 300 °C (c) and 350 °C (d).

To evaluate the possible Orowan mechanism for larger precipitates, the S40 samples were maintained at 450 ºC for 45, 130 and 225 minutes to obtain large precipitate sizes of 7.5, 12.4, and 14.8 nm in mean radius, respectively; then, the samples were tested at 300 ºC, shown in Fig. 4.11b. It is interesting to observe that these experimental data fall into the Orowan operative zone, and the yield strengthen increment slightly decreases when the precipitate radius is larger than 7.5 nm, which indicates that the calculated and experimental data have consistent tendencies (Figs. 4.11a and 4.11b).

For the SZ40 samples that were tested at 300 ºC, four data points of the yield strength increment are located in the dislocation climb zone between the $r+b$ and $r+2b$ climb distances (Fig. 4.11c). The tested strength values do not significantly change, which is attributed to a similar precipitate size and no coarsening at 300 ºC. The experimental data at 350 ºC are located in the calculated dislocation climb zone between $r+2b$ to $r+5b$ (Fig. 4.11d). At 350 ºC, the Al_3(Sc, Zr) precipitates also become obviously coarsening, and the mean precipitate radius increases from 1.1 nm at peak aging to 5 nm after 2000 h of annealing. The increase in precipitate size increases the climb distance. In the dislocation climb zone (Fig. 4.11d), a larger precipitate size corresponds to higher strengthening effect, but a larger dislocation climb distance means a lower strengthening effect. Because of the synthesizing effect of precipitate coarsening and dislocation climb distance increase in the dislocation climb model, the yield strength of SZ40 at 350 ºC remains approximately stable after the long-term annealing (Fig. 4.6b).

As previously mentioned, the classical precipitate shearing and Orowan bypass models can hardly predict the high-temperature strength of precipitation-strengthened materials. Using the dislocation climb model, the predicted yield stresses of S40 and SZ40 after the peak aging condition, tested at 250−350 ºC, are notably close the experimental data. The calculated values of S40 are located in the zone of the climb distance from r+2b to r+5b, whereas they are in the zone from r+b to r+2b for SZ40, shown in Fig. 4.12. The strong decrease in yield strength of S40 and SZ40 at elevated temperatures (250−350 ºC) (Fig. 4.4) is attributed to a lower strengthening efficiency of dislocation climb compared to precipitate shearing at ambient temperature.

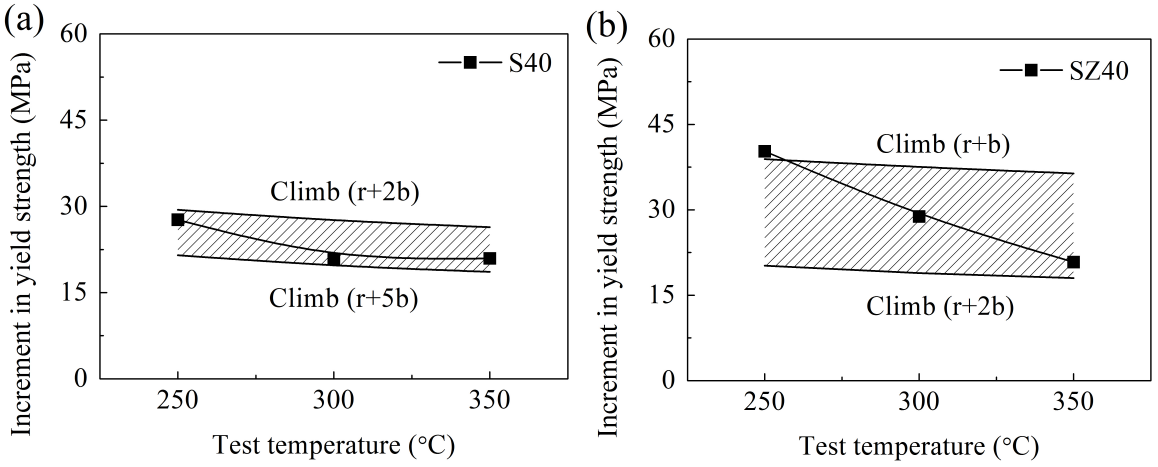

Fig. 4. 12. Calculated yield strength increments and experimental data after the peak aging tested at 250−350 ºC for S40 (a) and SZ40 (b).

It is evident that the dislocation climb model indeed predicts the trend of much lower yield stresses at high temperature for small and intermediate-sized precipitates (1-8 nm in radius) compared to ambient temperature. For larger precipitates (> 8-10 nm), the Orowan mechanism with modified G_m can predict the high-temperature yield strength. The high-temperature experimental data of S40 and SZ40 at peak aging and during the long-term annealing (precipitate coarsening) are fairly consistent with the theoretical prediction, which provides a conceptual understanding about the mechanical behavior at high temperature. However, there is no literature and experimental value for the dislocation distance y as a function of temperature and precipitate size in the dislocation climb model. With simplified assumptions in the model, the accuracy of the predictions is certainly affected to some extent.

4.4.4 Prospect of dislocation climb and Orowan mechanisms for high-temperature applications

For Al–based materials that are alloyed with Sc and Zr and exposed to high temperature (>0.6*Tm*), the coarsening of Al_3Sc and Al_3(Sc, Zr) precipitates are often inevitable. The strength variation with coarsening precipitates at high service temperature are major concerns for material design and application. Fortunately, the high-temperature strength of such materials is more tolerable for large precipitate size caused by the coarsening process. For the best strength at high temperatures (300−350 ºC), the optimal precipitate radius is approximately 7−9 nm for S40 and SZ40 (Figs. 4.11b and 4.11d). On the contrary, the highest strength at ambient temperature is achieved at the precipitate radius of approximately 2 nm (Fig. 4.8). At the intermediate size range (4–14 nm), the high-temperature strength only moderately changes with the precipitate size, which is predicted by the proposed dislocation climb and Orowan models (Fig. 4.11b and 4.11d). For example, the yield strength increment of S40 at 300 ºC (*r*+5b) changes from 44 MPa

with $\bar{r}$ = 4 nm to 33 MPa with $\bar{r}$=14 nm. Using the coarsening rate constant a = 3.16×10^{-32} m^3s^{-1} at 300 ºC (Fig. 4.3), it may take a total of 23 558 h as Al_3(Sc) precipitates grows up from 4 nm to 14 nm. SZ40 has a similar trend. The predicted strength increment (r+5b) at 350 ºC is approximately 39 MPa with $\bar{r}$ = 4 nm. When Al_3(Sc, Zr) precipitates coarsen to $\bar{r}$ = 14 nm, the strength increment only changes to 38 MPa. Using the coarsening rate a = 1.19×10^{-32} m^3s^{-1} at 350 ºC, it takes approximately 62 558 h to increase the precipitate radius from 4 nm to 14 nm. In addition, for coarser precipitates (>14 nm), the yield strength at high temperatures only slightly decreases according to the Orowan operative mechanism (Figs. 4.11b and 4.11d), which provides a good safety margin for materials with a slow coarsening rate at high temperature.

Previous studies [10, 30] found that the creep resistance of AlSc(Zr) alloys at elevated temperature (300 ºC) increased with increasing precipitate radius, and the optimal creep resistance occurred at the precipitate radii of 6 to 9 nm, which was explained using the dislocation climb mechanism. Similar to the creep resistance, the high-temperature strength

of Al_3Sc and $Al_3(Sc, Zr)$ with Al–B_4C composites is also less sensitive to coarse precipitates. With a low coarsening rate of Al_3Sc and $Al_3(Sc, Zr)$, Al–B_4C composites with Sc and Zr are expected to perform well during prolonged exposure at elevated service temperatures. The tolerance of the precipitate coarsening (maximum allowable precipitate radius) depends on the usage temperature and duration, because the overall performance of a material is a trade-off between both mechanical properties at ambient and high temperatures. The proposed dislocation climb and Orowan mechanisms in this work provide an insight of the precipitate strengthening at high temperature and a guide for further Al–B_4C composite design.

4.5 Summary

1. The presence of large B_4C particles (15 vol.% with average size 23 μm) has a moderate strengthening effect on Al–B_4C composites. The yield strength contribution of 15vol.% B_4C is approximately 12 MPa at ambient temperature and remains about 10 MPa at 300 °C. The precipitation of nanoscale Al_3Sc and $Al_3(Sc, Zr)$ in the

composite matrix provides a significant and predominate contribution to the composite strength at both ambient and elevated temperatures.

2. During long-term thermal annealing, the Al_3Sc precipitates in the Al-15 vol.%B_4C composite with 0.4 wt.%Sc (S40) remain coarsening-resistant at 250 °C, whereas the Al_3(Sc, Zr) precipitates in the Al-15 vol.%B_4C composite with 0.4 wt.%Sc plus 0.24 wt.%Zr (SZ40) are thermally stable at 300 °C. At higher annealing temperatures 300 °C for S40 and 350 °C for SZ40, both Al_3Sc and Al_3(Sc, Zr) precipitates coarsen with increasing annealing time. The yield strengths of S40 and SZ40 at ambient temperature decrease with increasing precipitate size, which can be explained by the classical precipitate shearing and Orowan bypass mechanisms.

3. The yield strengths of S40 at 250 °C and 300 °C slightly increase in the first 500 h of annealing and subsequently remain constant till 2000 hours, whereas the yield strengths of the SZ40 at 300 °C and 350 °C are always stable up to 2000 hours. At elevated temperatures, the yield strengths of S40 and SZ40 become approximately

independent of precipitate coarsening, which can be described and predicted by the dislocation climb mechanism.

4. The dislocation climb mechanism is invoked to explain the yield strength at elevated temperatures (> 0.5Tm). The dislocation climb and Orowan bypass mechanisms are proposed as the governing strengthening mechanisms for high-temperature mechanical properties. The combination of dislocation climb and Orowan models can explain the lower strengthening efficiency of coherent precipitates and the stable strength with coarse precipitates at high temperature compared to those at ambient temperature. The predicted yield strengths at elevated temperatures are consistent with the experimental data of S40 and SZ40 composites.

4.6 References

[1] Chen X-G. Application of Al-B_4C Metal Matrix Composites in the Nuclear Industry for Neutron Absorber Materials. In: Nikhil Gupta WHH, editor. Solidification Processing of Metal Matrix Composites: Rohatgi Honorary Symposium. USA: TMS, November 2006. p.343.

[2] Bonnet G, Rohr V, Chen X-G, Bernier J-L, Chiocca R, Issard H. Use of Alcan's Al-B4C metal matrix composites as neutron absorber material in TN International's transportation and storage casks. Packaging, Transport, Storage & Security of Radioactive Material 2009;20:98.

[3] Deng JX, Sun JL. Microstructure and mechanical properties of hot-pressed B4C/TiC/Mo ceramic composites. Ceramics International 2009;35:771.

[4] Kaufman JG. Properties of aluminum alloys: tensile, creep, and fatigue data at high and low temperatures. USA, 1999.

[5] Hyland RW. Homogeneous nucleation kinetics of Al3Sc in a dilute Al-Sc alloy. Metallurgical Transactions A 1992;23:1947.

[6] Royset J, Ryum N. Scandium in aluminium alloys. International Materials Reviews 2005;50:19.

[7] Lai J, Zhang Z, Chen XG. The thermal stability of mechanical properties of Al-B4C composites alloyed with Sc and Zr at elevated temperatures. Materials Science and Engineering a-Structural Materials Properties Microstructure and Processing 2012;532:462.

[8] Fuller CB, Seldman DN. Temporal evolution of the nanostructure of Al(Sc,Zr) alloys: Part II-coarsening of $Al_3(Sc_{1-x}Zr_x)$ precipitates. Acta Materialia 2005;53:5415.

[9] Elagin VIZ, V V; Pavlenko, S G; Rostova, T D Influence of Zirconium Additions on Aging of Aluminum--Scandium Alloys. (Translation) Physics of Metals and Metallography 1985;60:88.

[10] Fuller CB, Seidman DN, Dunand DC. Mechanical properties of Al(Sc,Zr) alloys at ambient and elevated temperatures. Acta Materialia 2003;51:4803.

[11] Riddle YW, Sanders TH. A study of coarsening, recrystallization, and morphology of microstructure in Al-Sc-(Zr)-(Mg) alloys. METALLURGICAL AND MATERIALS TRANSACTIONS A 2004;35A:341.

[12] Belov NA, Alabin AN, Eskin DG, Istomin-Kastrovskii VV. Optimization of hardening of Al-Zr-Sc cast alloys. Journal of Materials Science 2006;41:5890.

[13] Clouet E, Barbu A, Lae L, Martin G. Precipitation kinetics of Al_3 Zr and Al_3 Sc in aluminum alloys modeled with cluster dynamics. Acta Materialia 2005;53:2313.

[14] Tolley A, Radmilovic V, Dahmen U. Segregation in Al_3 (Sc,Zr) precipitates in Al-Sc-Zr alloys. Scripta Materialia 2005;52:621.

[15] Forbord B, Lefebvre W, Danoix F, Hallem H, Marthinsen K. Three dimensional atom probe investigation on the formation of Al_3 (Sc,Zr)-dispersoids in aluminium alloys. Scripta Materialia 2004;51:333.

[16] Harada Y, Dunand DC. Microstructure of Al(3)Sc with ternary transition-metal additions. Materials Science and Engineering a-Structural Materials Properties Microstructure and Processing 2002;329:686.

[17] Knipling KE, Dunand DC, Seidman DN. Criteria for developing castable, creep-resisitant aluminum-based alloys-A review. Zeitschrift Fur Metallkunde 2006;97:246.

[18] Chen XG, St-Georges L, Roux M. Mechanical Behavior of High Boron Content Al-B4C Metal Matrix Composites at Elevated Temperatures. Materials Science Forum, vol. 706: Trans Tech Publ, 2012. p.631.

[19] Lai J, Zhang Z, Chen X. Effect of Sc and Zr alloying on microstructure and precipitation evolution of as cast Al-B4C metal matrix composites. Materials Science and Technology 2012;28:1276.

[20] Chawla N, Shen YL. Mechanical behavior of particle reinforced metal matrix composites. Advanced Engineering Materials 2001;3:357.

[21] Lai J, Zhang Z, Chen XG. Precipitation strengthening of Al–B4C metal matrix composites alloyed with Sc and Zr. Journal of Alloys and Compounds 2013;552:227.

[22] Zhang Z, Fortin K, Charette A, Chen XG. Effect of titanium on microstructure and fluidity of Al-B_4C composites. Journal of Materials Science 2011;46:3176.

[23] Lai J, Zhang Z, Chen XG. Effect of Sc, Zr, and Ti on the interfacial reactions of the B_4C/Al system. Journal of Materials Science 2011;46:451.

[24] Kelly PM. Quantitative electron microscopy. Metals Forum 1982;5:13~23.

[25] Lifshitz IM, Slyozov VV. THE KINETICS OF PRECIPITATION FROM SUPERSATURATED SOLID SOLUTIONS. Journal of Physics and Chemistry of Solids 1961;19:35.

[26] Wagner C. THEORIE DER ALTERUNG VON NIEDERSCHLAGEN DURCH UMLOSEN (OSTWALD-REIFUNG). Zeitschrift Fur Elektrochemie 1961;65:581.

[27] Ardell AJ. Precipitation hardening. Metallurgical Transactions A 1985;16:2131.

[28] Harada Y, Dunand DC. Thermal expansion of Al3Sc and Al-3(Sc0.75X0.25). Scripta Materialia 2003;48:219.

[29] Touloukian Y. Thermophysical Properties of High Temperature Solid Materials: Vol. 1: Elements: Macmillan, 1967.

[30] Marquis EA, Seidman DN, Dunand DC. Precipitation strengthening at ambient and elevated temperatures of heat-treatable Al(Sc) alloys. Acta Materialia 2002;50:4021.

[31] Rosler J. Particle strengthened alloys for high temperature applications: strengthening mechanisms and fundamentals of design. International Journal of Materials and Product Technology 2003;18:70.

[32] Nembach E. Particle strengthening of metals and alloys: Wiley-VCH; 1 edition December 6, 1996.

[33] Marquis EA, Seidman DN, Dunand DC. Effect of Mg addition on the creep and yield behavior of an Al-Sc alloy. Acta Materialia 2003;51:4751.

[34] Karnesky RA, Meng L, Dunand DC. Strengthening mechanisms in aluminum containing coherent Al3Sc precipitates and incoherent Al2O3 dispersoids. Acta Materialia 2007;55:1299.

[35] Marquis EA, Dunand DC. Model for creep threshold stress in precipitation-strengthened alloys with coherent particles. Scripta Materialia 2002;47:503.

[36] Cahn R, Haasen P. Physical Metallurgy Vol. III. vol. III: Elsevier Science BV, Amsterdam, The Netherlands, 1996. p.1883.

[37] Miura Y NM, Furuta A. In: Hosoi Y YH, Oikawa H, Maruyama K, editors., editor. 7th JIM Int. Symp. on Aspects of High Temperature Deformation and Fracture in Crystalline Materials. Nagoya: The Japan Institute of Metals. p.25.

[38] Krug ME, Dunand DC. Modeling the creep threshold stress due to climb of a dislocation in the stress field of a misfitting precipitate. Acta Materialia 2011;59:5125.

[39] Dundurs J. Elastic interaction of dislocations with inhomogeneities. Mathematical theory of dislocations 1969:70.

[40] Meyers MA, Chawla KK. Mechanical metallurgy: principles and applications: Prentice-Hall, 1984.

[41] Jansson B, Melander A. On the critical resolved shear stress from misfitting particles. Scripta Metallurgica 1978;12:497.

[42] Dieter GE, Bacon D. Mechanical metallurgy. London: McGraw-Hill, 1988.

[43] Fu C. Electronic, elastic, and fracture properties of trialuminide alloys: Al3Sc and Al3Ti. Journal of Materials Research 1990;5:971.

[44] Fukunaga K, Shouji T, Miura Y. Temperature dependence of dislocation structure of L12–Al3Sc. Materials Science and Engineering: A 1997;239–240:202.

[45] George EP, Pope DP, Fu CL, Schneibel JH. Deformation and Fracture of L1$_2$ Trialuminides. ISIJ International 1991;31:1063.

[46] Hyland Jr R, Stiffler R. Determination of the elastic constants of polycrystalline Al< sub> 3</sub> Sc. Scripta metallurgica et materialia 1991;25:473.

[47] Frost HJ, M. F. Ashby Deformation-mechanism maps: the plasticity and creep of metals and ceramics. New York: Pergamon Press, 1982.

[48] Drits ME, Toropova LS, Bykov YG, Gushchina FL, Elagin VI, Filatov YA. Metastable State Diagram of the Al-Sc System in the Range Rich in Aluminum. Russian Metallurgy 1984:83.

[49] Tabor D. The hardness and strength of metals. Journal of the Institute of Metals 1951;79:1.

[50] Iwamura S, Miura Y. Loss in coherency and coarsening behavior of Al 3 Sc precipitates. Acta Materialia 2004;52:591.

[51] Tiryakioğlu M, Ökten G, Hudak D. Statistics for estimating the population average of a Lifshitz–Slyozov–Wagner (LSW) distribution. Journal of Materials Science 2009;44:5754.

CHAPTER 5

MECHANICAL PROPERITES AND THEIR THERMAL STABILITY OF HOT-ROLLED Al–15%B_4C COMPOSITE SHEETS CONTAINING SC AND ZR AT ELEVATED TEMPERATURE

Chapter 5

Mechanical properties and their thermal stability of hot-rolled Al–15%B_4C composite sheets containing Sc and Zr at elevated temperature

5.1 Introduction

Aluminum-based metal matrix composites (MMCs) have been widely used in automotive, aerospace and military industries as either structural or functional materials because of their light weight, high specific modulus, low coefficient of thermal expansion and other special properties [1]. As a neutron absorption material, Al–B_4C composites are applied to fabricate the transport and storage containers of spent nuclear fuels because of the special capacity for capturing neutrons [2, 3]. In service, Al–B_4C composites absorb the neutrons and generate heat and hence it can expose to elevated temperatures (250-350 °C)

for an extended period [4, 5]. It demands that the material can maintain its mechanical properties and thermally stability at such temperatures. Sc was introduced to aluminum alloys to enhance the mechanical properties by forming fine coherent Al_3Sc precipitates with a low coarsening rate (stable up to 300 °C) [6]. The addition of Zr can further reduce the coarsening rate of the precipitates [7, 8], improve the thermal stability of precipitates (stable up to 350 °C) [7] and increase the strength and recrystallization resistance [9-11]. Therefore, the Al–Sc and Al–Sc–Zr matrix are promising candidates to develop advanced Al–B_4C composites that are applicable at elevated temperatures.

In recent years, several researchers put great efforts into understanding the strengthening behavior and creep properties of Al–Sc and Al–Sc–Zr cast alloys [11-13]. The mechanical properties at room and elevated temperatures of Al–B_4C cast composites that contain Sc and Zr were investigated in our previous works [14-16]. Al_3Sc and $Al_3(ScZr)$ precipitates could strengthen Al–B_4C cast composites and were thermally stable up to 300ºC. To manufacture useful engineering final products, Al–B_4C cast composites need to

undergo the hot-working processes such as rolling, extrusion and forging. It was reported that Al_3Sc precipitation hardening in deformed materials was difficult because of severe limits on the solution treatment, hot deformation and post heat treatment [17]. In our previous work [18], we found that the strengthening solute atoms (Sc) in an Al–B_4C composite would be consumed during the post-rolling solution heat treatment, and the consumption of Sc increased with the increase in deformation ratio. In general, the public information about the hot deformation process, post-deformation heat treatment, and microstructure evolution for Al–Sc and Al–Sc–Zr alloys is notably scarce. Furthermore, notably few papers address the mechanical properties at elevated temperature of final deformed Al–Sc alloys and deformed Al–B_4C composites that contain Sc and Zr.

The damage and failure modes of composite materials are important aspects for an engineering product. The failure mechanism of particulate-reinforced MMCs can be classified into three types: reinforcement fracture when the matrix is stronger than the reinforcement [19, 20]; interfacial decohesion when the bonding force is lower than the

matrix and reinforcement [21, 22]; ductile failure because of the void coalescence of the matrix [23, 24]. However, the fracture behavior at elevated temperature for Al–B_4C composites is little known.

In the present work, the mechanical properties as a function of temperature and the evolution of mechanical properties during long-term annealing at 300 °C for two hot-rolled Al–15 vol.% B_4C composite sheets containing Sc and Zr were investigated. The effect of the post-rolling heat treatment on the Al_3Sc and $Al_3(Sc,Zr)$ precipitation hardening was studied. The evolution of Al_3Sc and $Al_3(ScZr)$ precipitates in rolled sheets during long-term annealing was observed. In addition, the effect of the testing temperatures on the fracture behavior of two hot-rolled Al–B_4C composite sheets was studied.

5.2 Experimental procedure

In the present work, two experimental Al 1100–15 vol. % B_4C composites were prepared in an electric resistance furnace to obtain the desirable chemical composition: S40

with 0.4 wt.% Sc and SZ40 with 0.4 wt.% Sc plus 0.24 wt.% Zr. The average size of the B_4C particles was 23 μm. Their nominal chemical compositions are listed in Table 3.1. Under mechanical stirring using an impeller, the composite melt was held at 740 °C for 30 min. and subsequently poured into a rectangular permanent steel mold that measured 30×40×80 mm. The cast ingots of two composites were homogenized at 640 °C for 24 hours (S40) and 96 hours (SZ40), respectively, and quenched in water at room temperature. Then, the cast ingots were hot-rolled on a laboratory scale rolling mill (STANAT CX-100) with multi-passes in a temperature range of 400 to 500 °C. The rolling began from the 30 mm thick original ingot and ended at the 4 mm sheets with a total reduction ratio of 87%. After hot rolling, the composite sheets were solution-treated at 640 °C for different time lengths, quenched with water at room temperature, and aged at 300 °C for 24 hours. To assess the long-term thermal stability of the mechanical properties, the heat-treated sheets were annealed at 300 °C for up to 2000 hours.

The tensile properties were measured with an Instron machine according to the ASTM E8M-04 standard for room temperature and ASTM E21 standard for elevated temperature. The ultimate tensile strength (UTS), 0.2% yield strength (YS) and elongation at fracture (EL) were averaged over three tests for each condition. The tensile samples with an overall length of 100 mm and the gage gauge length of 25 mm and width of 6 mm were machined from the rolled sheets based on ASTM E8M-04 standard.

The microstructure of the composites was observed using an optical and scanning electronic microscope (SEM, JSM-6480LV), which was equipped with an electron backscatter diffraction system (EBSD) and an energy dispersive spectrometer (EDS). The fracture surfaces of the tensile samples were examined using SEM. A transmission electron microscope (TEM, JEM-2100) that operated at 200 kV was used to observe the precipitates Al_3Sc and Al_3(Sc Zr). Centered dark-field images of the precipitates were recorded using the {100} super-lattice reflections near the <011> direction. Two-beam diffraction

conditions were applied for the precipitate observation. The precipitate equivalent diameters were determined using image analysis on the TEM images.

5.3 Results and discussion

5.3.1 Microstructure of as-cast and as-rolled composites

The as-cast microstructure of the composites in an example S40 is shown in Fig. 5.1. B_4C particles were generally uniformly distributed in the aluminum matrix, and some small interfacial reaction particles [25] were also visible, attached or surrounded on the B_4C particles (Fig. 5.1a). After etching, the aluminum matrix of composites evidently consisted of coarse and equiaxed grains with an average size of 100 to 130 μm.

During the multi-pass hot rolling, the composite materials experienced repeated work hardening, dynamic recovery and dynamic recrystallization. The EBSD mapping images (Fig. 5.2) show the as-rolled grain structures at the 87% deformation ratio (4 mm sheets). The grains were arranged along the rolling direction, and the grain sizes were much smaller

than the as-cast grains. In addition, a large amount of sub-grains and dislocation bands with a misorientation less than 15° were created in both S40 and SZ40 samples.

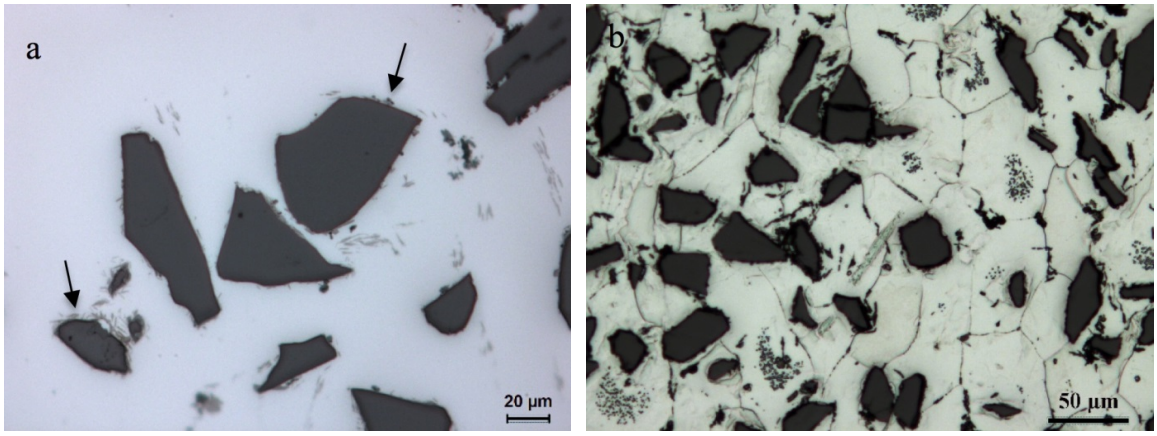

Fig. 5. 1. Optical microstructure of the as-cast S40 composite (a) with arrows pointing to the small interfacial reaction particles that surrounded the B_4C particles, and the etched sample shows equiaxed grains of the Al matrix (b).

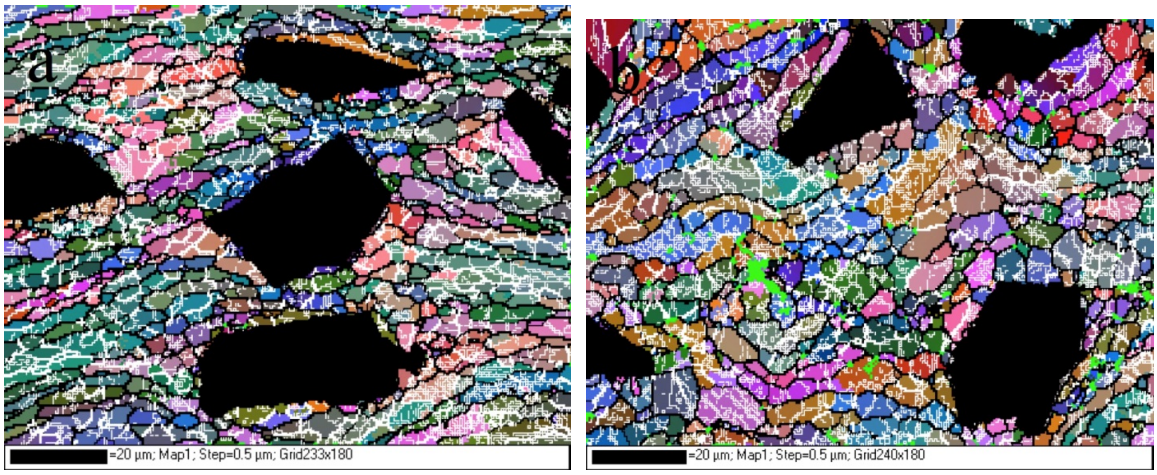

Fig. 5. 2. EBSD mapping shows the grains and subgrain structures in the 4 mm as-rolled S40 sheet (a) and SZ40 sheet (b). The black regions are B_4C

particles. The other colors indicate the grains or subgrains with misorientations: thin white lines: 1~5°; white lines: 5~15°; black lines: >15°.

5.3.2 Post-rolling heat treatment

After hot rolling, the as-rolled sheets were notably soft. To gain the appropriate mechanical properties as useful engineering materials, the as-rolled materials experienced a post-rolling heat treatment, which involved both solution and aging for precipitation hardening. To find the optimal heat treatment, the solution treatment was performed at 640 ºC with different holding time lengths and a subsequent fixed aging treatment at 300 ºC for 24 hours, which was identified as the peak aging condition for Al-Sc-B_4C and Al-Sc-Zr-B_4C composites [14]. The Vickers' hardness of the aluminum matrix of both composite sheets as a function of the solution time is shown in Fig. 5.3. The hardness values of the S40 and SZ40 composites in the as-rolled condition were 39 and 42 HV, respectively, which showed a low strength of the materials after hot rolling. After only one hour of solution treatment, the hardness increased to 62 HV for S40 and 70 HV for SZ40. These peak values were maintained for approximately three and six hours for S40 and

SZ40, respectively. After the peak aging plateau, the hardness gradually decreased with increasing solution time.

During the multi-pass hot rolling, the homogenized composite ingots experienced a repeated thermomechanical annealing process at 400-500 °C. The solutes of Sc and Zr precipitated from the supersaturated aluminum matrix in the forms of Al_3Sc or Al_3(Sc Zr) precipitates. However, because of the high precipitation temperature, those precipitates were notably coarse: their diameters were tens to hundred nanometers (Fig. 5.4a). In addition, many of them were on the grain or sub-grain boundaries, which resulted in the loss of most of their hardening effect. The results in Fig. 5.3 suggest that the solution treatment of rolled composite sheets in a relatively short time (~ one hour) can dissolve these coarse precipitates back to the aluminum matrix, which ensures the re-precipitation of much fine precipitates during subsequent aging and regains the strength of the rolled composite sheets. Fig. 5.5 shows the precipitates in S40 and SZ40 that were solution-treated at 640 ºC for three hours and aged at 300 ºC for 24 hours. The fine

nanoscale precipitates uniformly distributed in the aluminum matrix. The average diameters of the precipitates were 2.8 nm (Al_3Sc in S40, Fig. 5.5a) and 3 nm ($Al_3(Sc,Zr)$ in SZ40, Fig. 5.5b), which resulted in a much higher strength after the post-rolling treatment than that in the as-rolled condition (Fig. 5.3).

After the post-rolling heat treatment, the sub-grain structure that formed during rolling (Fig. 5.2) was completely eliminated, and all grains were fully recrystallized (Fig. not showing here). Because of the high solution temperature, the grain structure became notably coarse, and the average grain sizes of S40 and SZ40 were 94 and 42 μm, respectively.

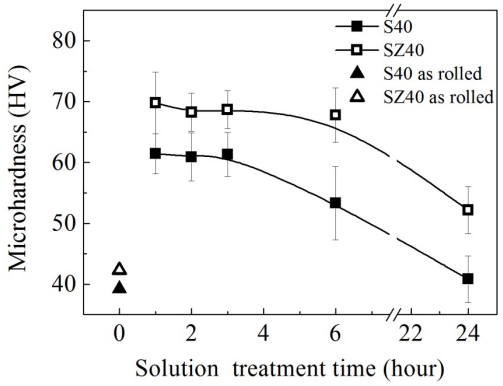

Fig. 5. 3. Vickers' hardness of both composite sheets as a function of the solution time (solution at 640 ºC and aging at 300 ºC/24 h).

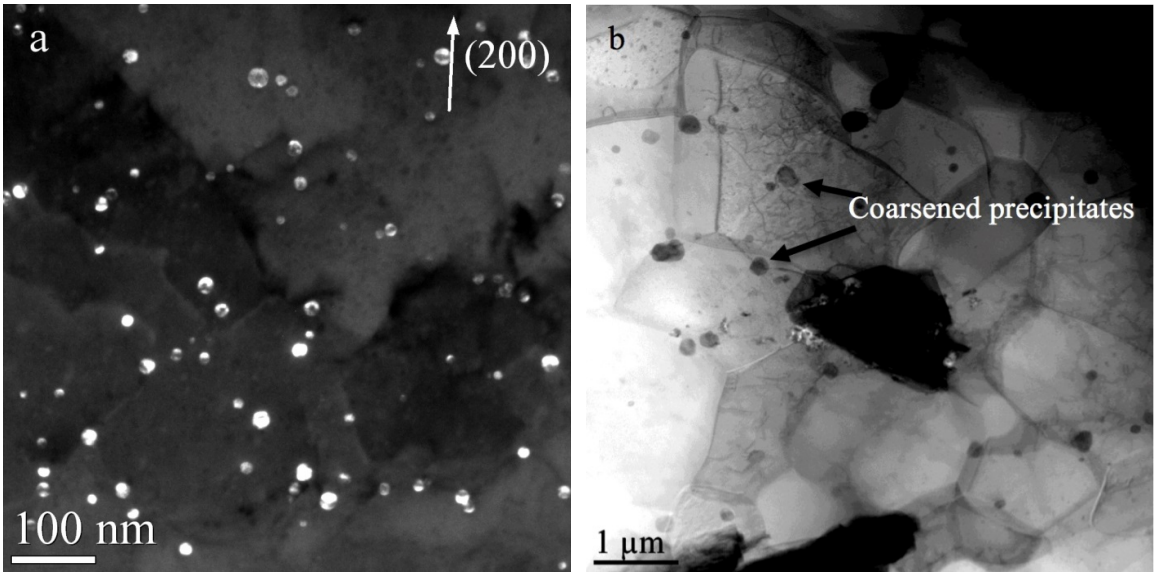

Fig. 5. 4. Dark-field TEM images of the coarse precipitates in SZ40 (a) and STEM image of many coarse precipitates on the grain and subgrain boundaries (b).

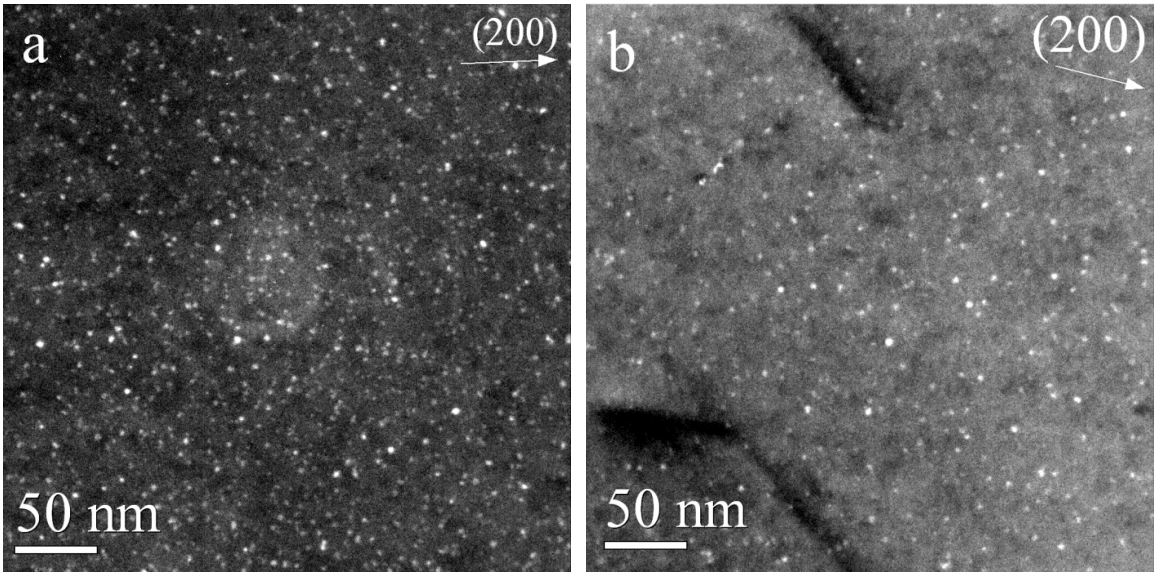

Fig. 5. 5. Fine precipitates in the aluminum matrix of S40 (a) and SZ40 (b) after the peak aging of the rolled sheets (solution-treated at 640 °C/3 h and aged at 300 ºC/24 h).

5.3.3 Mechanical properties and their thermal stability

5.3.3.1 Tensile properties at different temperatures

The tensile properties of the rolled S40 and SZ40 composite sheets after peak aging were tested at 25 °C, 250 °C and 300 °C. Fig. 5.6 shows the ultimate tensile strength (UTS), 0.2% offset yield strength (YS) and elongation (EL) of both composite sheets at different test temperatures.

In general, the UTS and YS of both materials decrease, and the EL increases with increasing test temperatures. For example, the UTS and YS of S40 were 197 MPa and 152 MPa at ambient temperature but became 65 MPa and 55 MPa at 300 ºC, respectively. The EL of S40 was approximately 9% at ambient temperature and increased to 30% at 300 ºC. The strength of S40 at 300 ºC was approximately 35% of the strength at ambient temperature whereas the elongation at 300 ºC was approximately 3.3 times of that at

ambient temperature. For the SZ40 composite, the UTS and YS at ambient temperature were 210 MPa and 166 MPa, respectively, which were slightly higher than that of S40 at ambient temperature. However, at elevated temperatures (250−300 ºC), the tensile strengths of both composites became close, and the values remained almost constant.

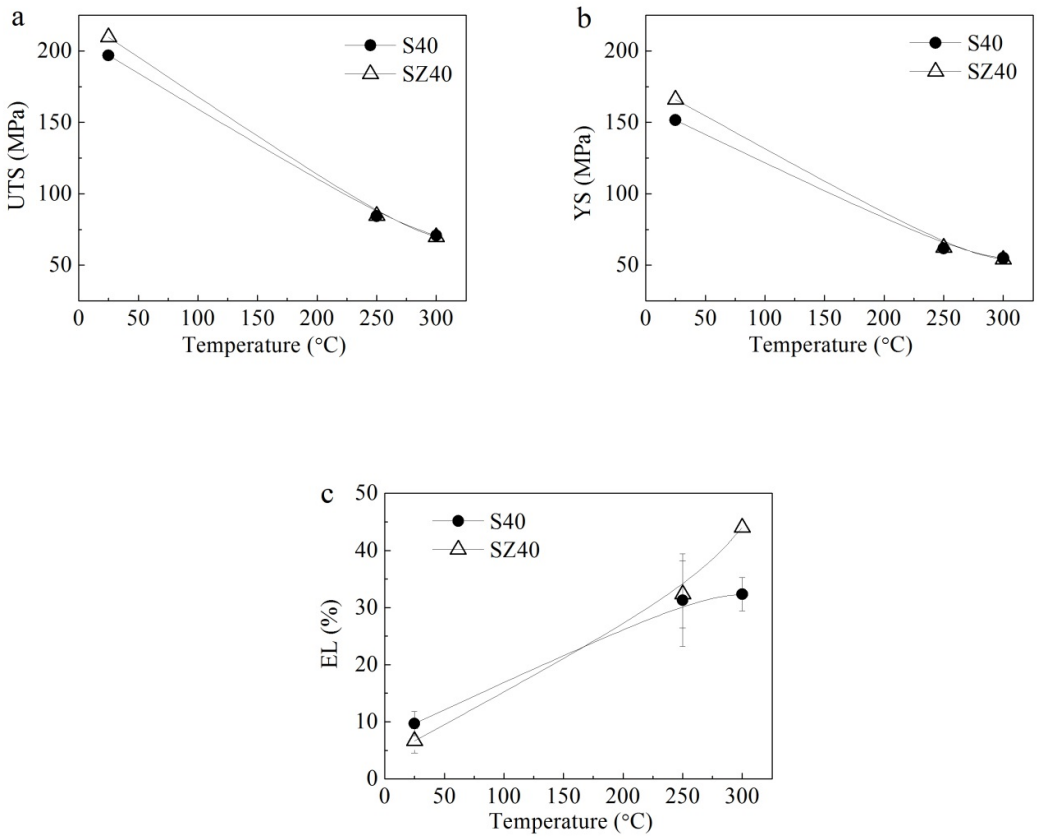

Fig. 5. 6. Tensile properties of the S40 and SZ40 sheets after peak aging as a function of temperature: UTS (a), YS (b) and El (c).

5.3.3.2 Evolution of tensile properties during long-term annealing

After the peak aging, the S40 and SZ40 composites were annealed at 300 °C for up to 2000 hours to assess the long-term thermal stability of the materials. Fig. 5.7 shows the mechanical properties of the S40 and SZ40 samples as a function of the annealing time, which were tested at both ambient temperature and 300 °C. The strengths (UTS and YS) at the ambient temperature slowly decreased with increasing annealing time. The UTS of S40 slightly decreased from 197 MPa to 190 MPa, whereas the YS slightly decreased from 152 MPa to 148 MPa after 2000 h of annealing (Figs. 5.7a and 5.7c). SZ40 generally has higher strengths than S40 (~15 MPa above) but the strengths exhibit the identical decreasing tendency as S40 during 2000 h of annealing. The EL of both composites did not significantly change during the entire annealing process (Fig. 5.7e).

At 300 ºC, the UTS and YS and their evolution during annealing for both composites are almost identical (Figs. 5.7b and 5.7d). The UTS only slightly decreased from 70 to 65 MPa in the first 500 h of annealing and subsequently stabilized in the remaining annealing

period. The YS was approximately 55 MPa and remained unchanged during the entire annealing process. The elongation of both composites moderately decreased in the first 500 h of annealing and stabilized at approximately ~26% (Fig. 5.7f). The independence of the UTS and YS from the annealing time at 300 ºC for up to 2000 h indicates the excellent long-term thermal stability of both S40 and SZ40 composite sheets at elevated temperature.

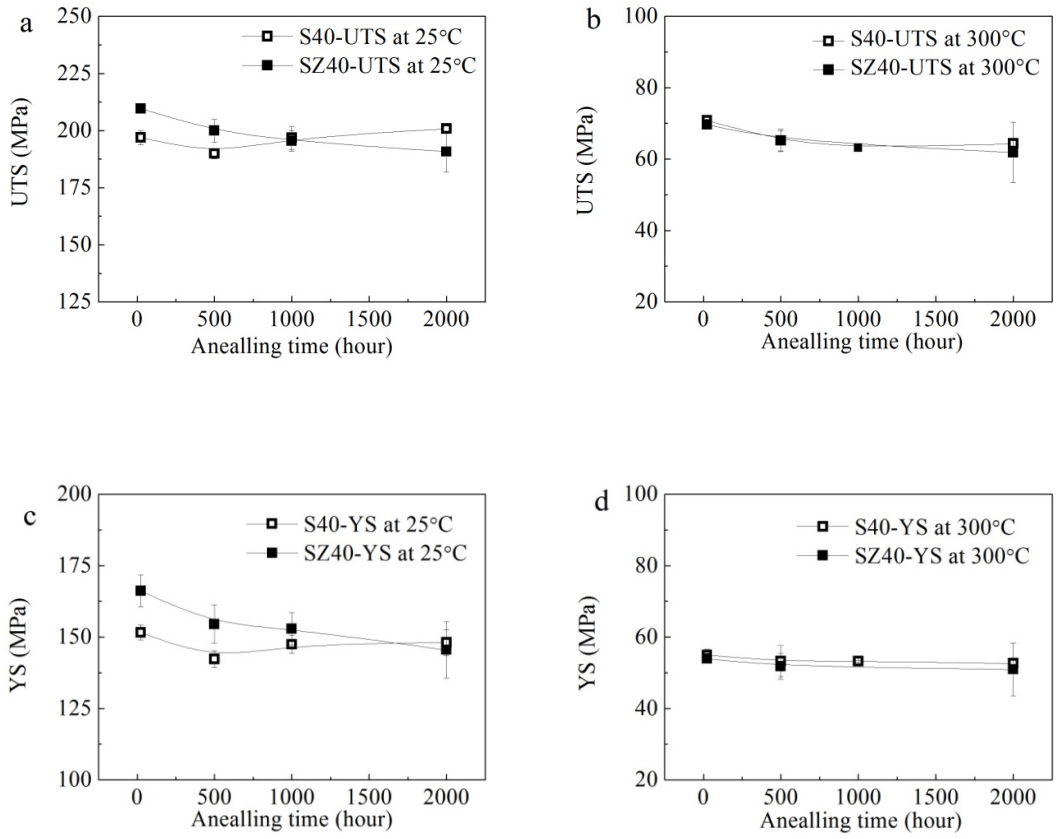

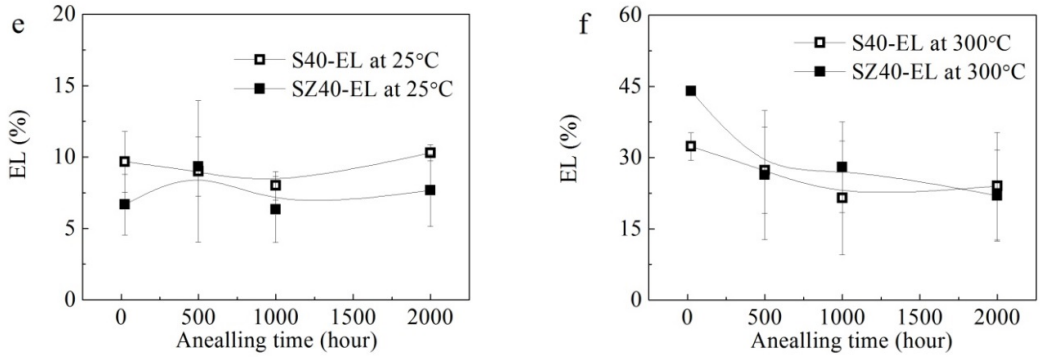

Fig. 5. 7. Evolution of the mechanical properties of both S40 and SZ40 composite sheets during long-term annealing at 300 °C: (a) UTS, (c) YS and (e) EL at 25 °C; (b) UTS, (d) YS and (f) EL at 300 °C.

It is well-known that the AA1100 matrix is a non-heat-treatable material, the strength of which is mainly gained by strain hardening during deformation. After annealing, the AA1100−O matrix is notably soft, and the YS is only 38 MPa at ambient temperature [26], which cannot provide much support to strengthen the Al−B_4C composites. After the alloying with Sc and Zr and the peak aging, the strengths of S40 and SZ40 largely increase because of the precipitation strengthening of nanoscale Al_3Sc and Al_3(Sc Zr) precipitates. The YS at ambient temperature can reach 150 MPa and 165 MPa for S40 and SZ40, respectively. Fig. 5.8 shows the TEM images of the precipitates after 2000 h of annealing at

300 °C. During long-term annealing, a slow coarsening process occurred for both Al_3Sc and Al_3(Sc Zr) precipitates. Compared to Fig. 5.5, the average size of Al_3Sc in S40 increased from 2.8 nm to 14 nm (in the diameter), whereas the size of Al_3(Sc Zr) in SZ40 increased from 3 nm to 4.6 nm (in diameter) after 2000 h of annealing. The slow decrease in strengths (UTS and YS) at ambient temperature during long-term annealing is mainly because of the precipitate coarsening. In general, the classical precipitate shearing and Orowan dislocation bypassing mechanisms can explain the ambient temperature strength in precipitate-strengthening materials [12, 13, 16]. In the case of coarsening during annealing, the precipitates become too large for shearing, and Orowan dislocation bypassing begins to be active. Therefore, the strength decreases with increasing precipitate size under the Orowan dislocation bypassing mechanism.

In certain applications, the mechanical properties and thermal stability of Al–B_4C composites at elevated temperature are highly important [14, 16], which is the main reason for alloying with Sc and Zr. It was reported that, in the absence of precipitate strengthening,

the YS at 300 °C was only approximately 14 MPa for the AA1100 matrix [26] and 23 MPa for an AA1100−25% B_4C composite [27], which could not serve as a useful structural material at elevated temperature. In the present study, the YS at 300 °C of both S40 and SZ40 rolled sheets approaches 55 MPa. This improvement is significant for elevated-temperature applications. More importantly, the strength at 300 °C of both S40 and SZ40 sheets are notably stable for at least 2000 h. It brings a highly interesting property for structural applications, which may experience an extended period of exposure to high service temperatures (250−350 °C). In contrast to the strengths at ambient temperature, the strengths (both UTS and YS) at 300 °C are less sensitive to the annealing time and more tolerable for precipitate coarsening. In our recent study [15], a dislocation climb mechanism was proposed to explain the precipitate strengthening at elevated temperatures (> 0.5 T_m), where the elevated temperature strength was much less sensitive to coarse precipitates in a certain range of precipitate sizes. Detailed discussions of precipitate strengthening mechanisms of this composites at elevated temperature can be found in [15]. The

experiment results in the present study are consistent with the predication of the dislocation climb mechanism.

It is worthwhile to mention that the Al_3Sc precipitates in S40 have a higher coarsening rate than the $Al_3(Sc,Zr)$ precipitates in SZ40 (Fig. 5.5 vs. Fig. 5.8). Results demonstrated that, within 2000 h of annealing, the coarsening of Al_3Sc precipitates in S40 did not affect the tensile strength at 300 °C yet. However, with further prolonged annealing, the coarsening of Al_3Sc certainly continues, and up to some point, the strength of S40 is expected to decrease because of the weaker strengthening effect of coarsened precipitates. However, it is anticipated that the strength of SZ40 at 300 °C is more stable for the annealing much beyond 2000 h because of the low coarsening rate of $Al_3(Sc,Zr)$ precipitates. Thus, the SZ40 composite is more suitable for applications with exposure to high service temperatures for extended periods of time.

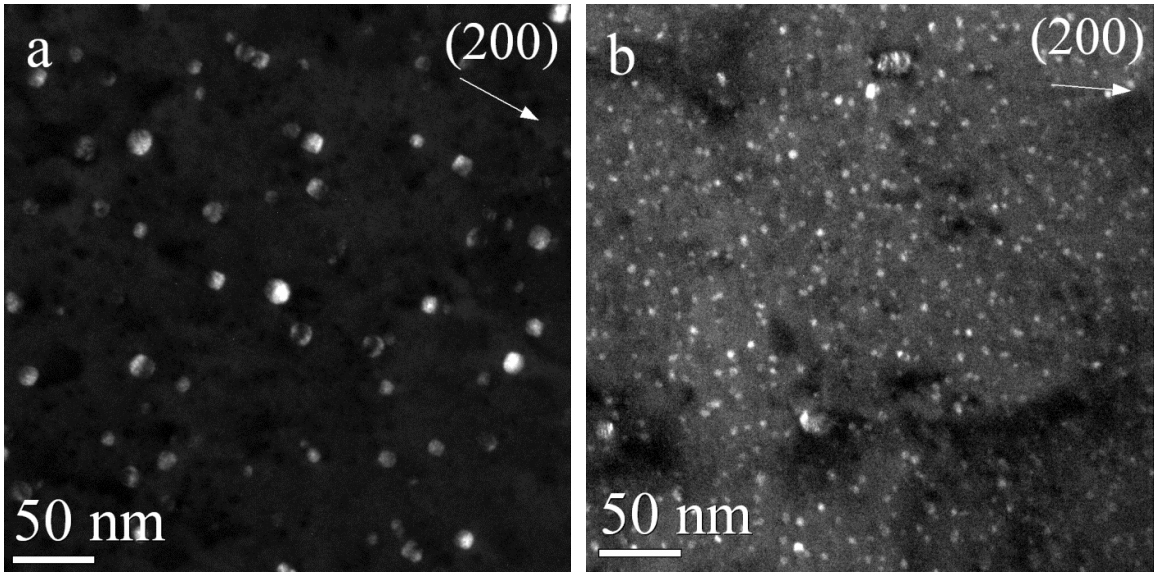

Fig. 5. 8. TEM dark-field images of the coarsened precipitates after 2000 h of annealing in S40 (a) and SZ40 (b).

5.3.4 Fractography

The fracture surfaces of the tensile samples, which were tested at 25, 250 and 300 ºC, were examined by SEM to study the fracture mechanisms during the tensile deformation. Fig. 5.9 shows the typical SEM micrographs of the fracture surfaces of the tested S40 sample at 25 °C. Many ductile dimples in the aluminum matrix and brittle fracture in B_4C particles evidently appeared on the fracture surface (Fig. 5.9a). The deep dimples in the matrix indicate that plastic deformation occurred before the final failure [28, 29]. The B_4C

particle fractures had a cleavage and facet plane (Fig. 5.9b). In a cross section of the fracture surface, a large crack throughout the B_4C particle was clearly observed (Fig. 5.9c). When the test temperature increased to 250 °C, two types of dimples were observed in the fracture (Fig. 5.10): the small and ductile dimples in the matrix, which were several micrometers in size, and the larger dimples that were tens of micrometers in size, which was similar to the B_4C particle size. Small particles appeared at the bottom of the large dimples (Fig. 5.10b). Ti and Sc were detected in the small particles (Fig. 5.10c), which indicated that the large dimples were the interface layers between B_4C particles and the aluminum matrix, where the B_4C particles were debonded during the tensile deformation. The interfacial decohesion of B_4C particles was observed in most parts of the fracture surface. However, few B_4C particle fractures were found in the fracture surface (arrow in Fig. 5.10a), but the amount of broken B_4C particles was less than 10% of B_4C particles. When tested at a higher temperature (300 °C), the fracture surface was only dominated by the interfacial decohesion of B_4C particles and ductile dimples in the matrix (Fig. 5.11). In

the cross section of the fracture surface, the interfacial decohesion of B_4C particle was more evident (Fig. 5.11c); no more fracture of B_4C particles was found.

The fracture observation of the tested SZ40 samples at different temperatures indicates a similar tendency to that of the S40 samples: the brittle particle fracture and ductile matrix fracture at ambient temperature and the interfacial decohesion and ductile matrix rupture at 300 ºC. Moreover, for both S40 and SZ40 samples after long-term annealing (300ºC/2000h), the observation of the fracture surface showed that the long-term annealing did not change the fracture behavior because the B_4C ceramic particles and their interfaces with solid aluminum were notably stable at such temperature.

The fracture types of particulate-reinforced MMCs under tensile stress can be classified into three cases [30]: (1) particle fracture, which occurs when the matrix is strong and the local stress exceeds the fracture strength of the reinforcement particle; (2) interfacial decohesion, which is related to the characteristic that the local stress is lower than the particle fracture but higher than the interfacial strength; (3) matrix fracture because of the

void coalescence, when both interface and reinforcement are stronger than the matrix. During the tensile deformation of the Al–B_4C composites, the aluminum matrix begins to plastically deform, which is associated with dislocation pile-up near the particle/matrix interfaces. The increase in shear stress at the head of the pile-up can be transferred to the B_4C particles through the interface. With the precipitation of nanoscale Al_3Sc and $Al_3(Sc,Zr)$ precipitates, the UTS of the S40 and SZ40 samples at ambient temperature is notably strong and approximately 200 MPa. During the tensile deformation, the applied local stress appears to exceed the fracture strength of B_4C particles. Cracks can nucleate on the particle surface under the action of the shear stress and easily propagate through the entire particles. After the failure of the B_4C particles, the increase in stress on the matrix causes void growth and coalescence, and the composite sample is finally ruptured with the ductile dimple morphology in the matrix fracture surface. Therefore, the fracture at ambient temperature is dominated by the brittle B_4C particle fracture.

When tested at high temperature (250 °C), the tensile strength of the S40 and SZ40 composites significantly decreased (Fig. 5.6), and the applied stress was not sufficient to fracture most particles but exceeded the interface strength. The interfacial decohesion with partial particle fracture became the dominant feature for the material failure at 250 ºC. With further increase in test temperature (300 °C), the UTS of the composites decreased again (to approximately 65 MPa). The applied local stress was much lower than the particle strength but remained higher than the interface strength. The main characteristic of the fracture became purely interfacial decohesion. The rupture of the composite at 300 ºC is mainly controlled by the interfacial separation between B_4C particles and the matrix.

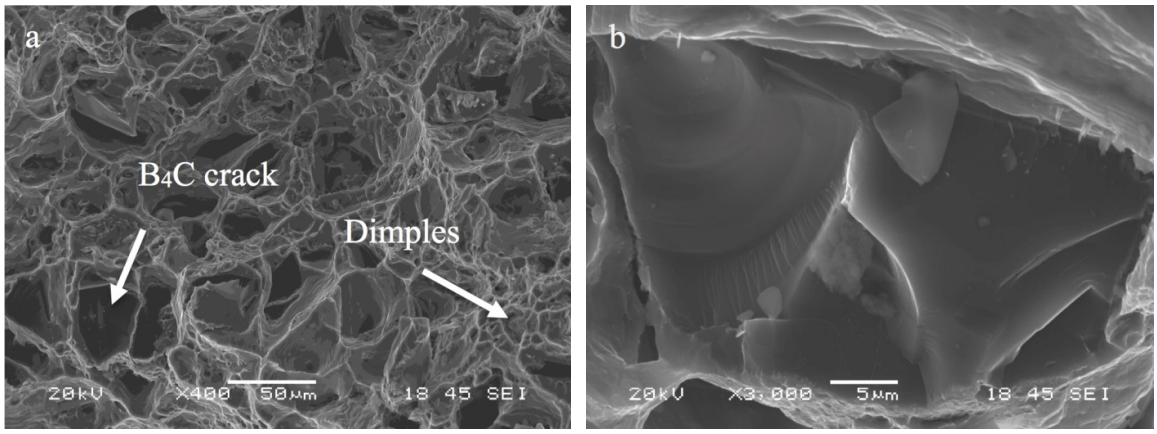

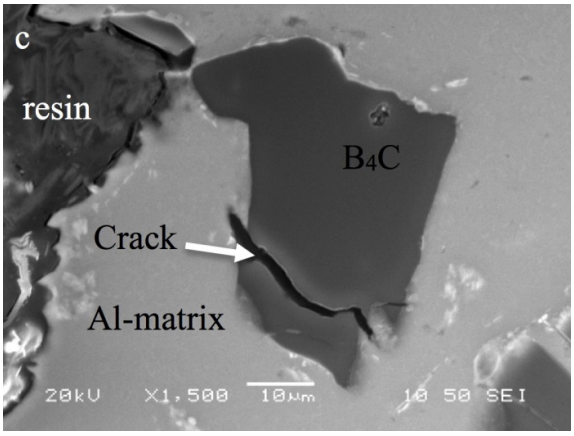

Fig. 5. 9. SEM images of the tensile fracture surface of the tested S40 sample at 25°C: (a) general view; (b) enlarged fracture surface of a B_4C particle; (c) cross-section of the fracture.

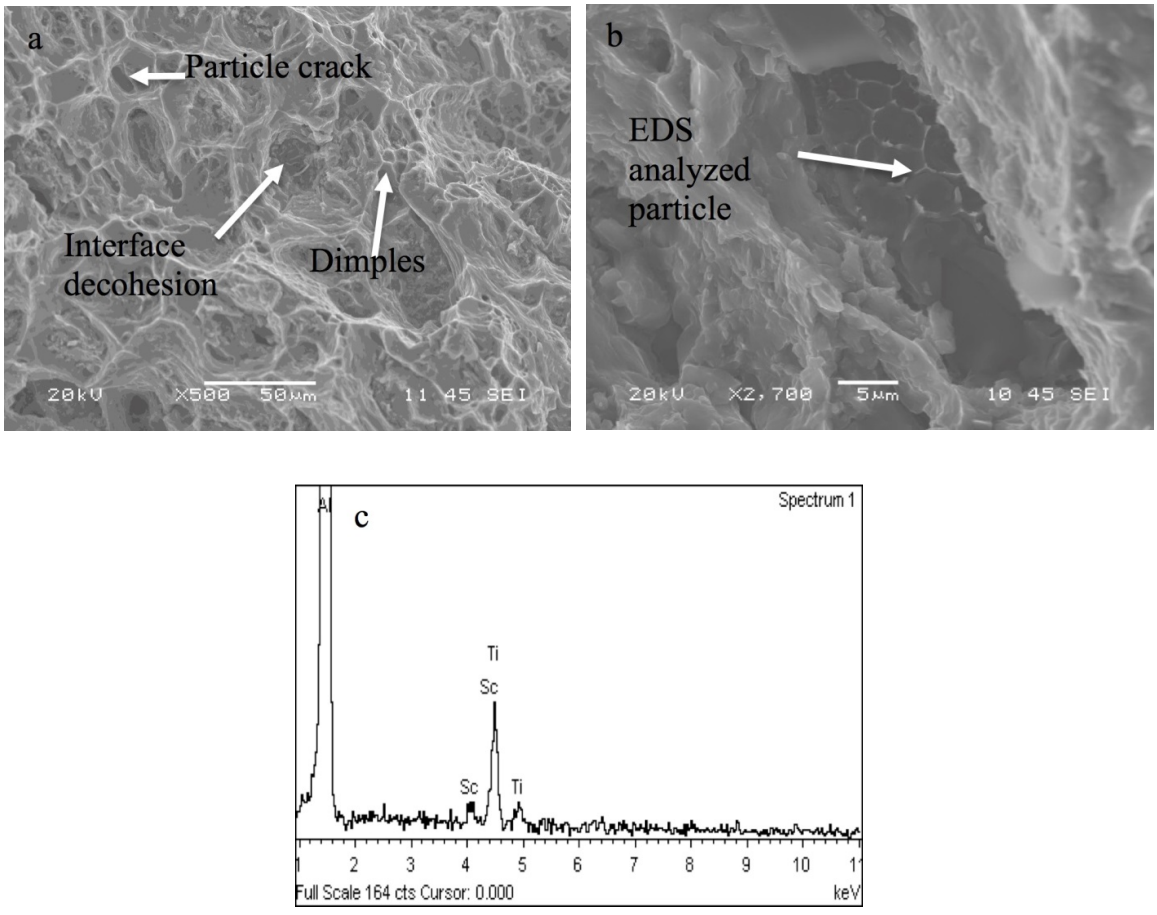

Fig. 5. 10. SEM images of the tensile fracture surfaces of the tested S40 at 250 °C: (a) general view; (b) enlarged view of the interfacial decohesion, where the B_4C particle was out of the matrix; (c) EDS spectrum of a small particle in the interfacial layer.

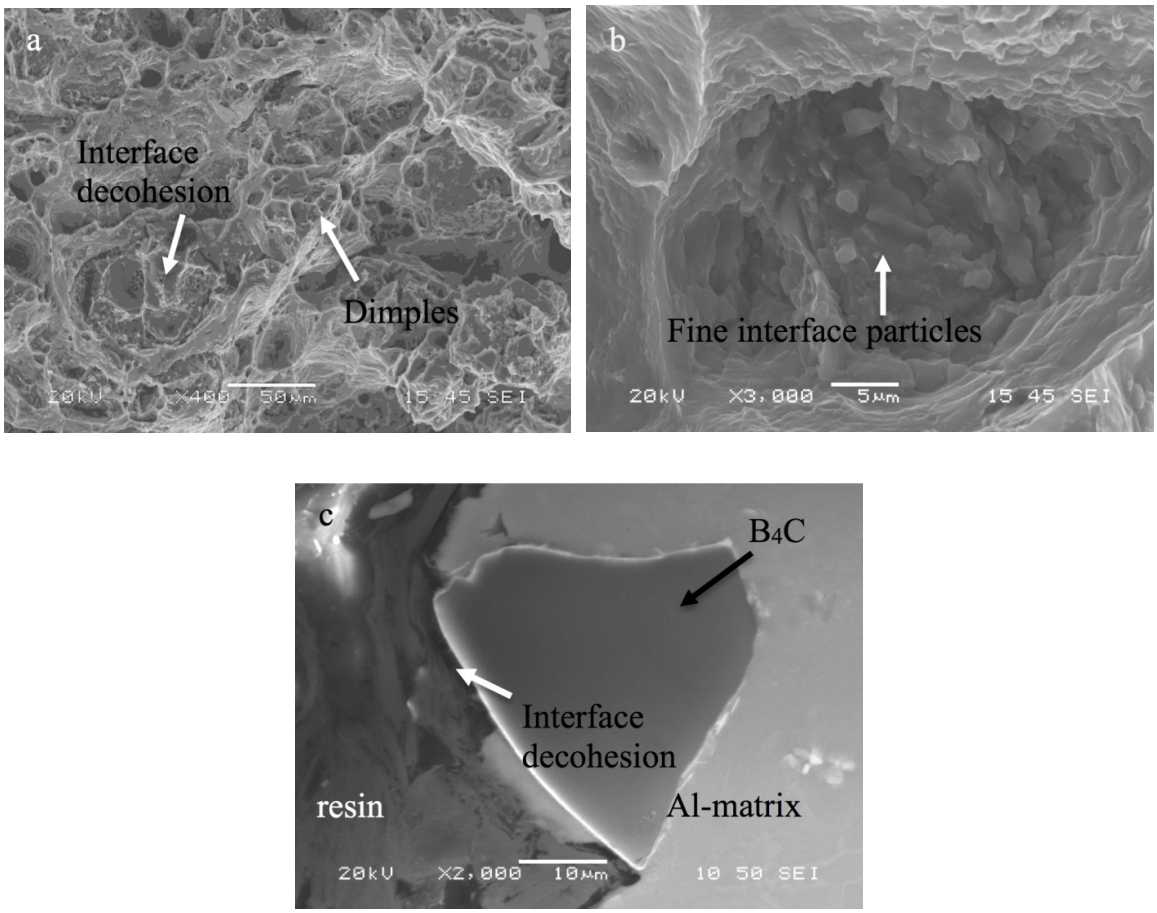

Fig. 5. 11. SEM images of the tensile fracture surfaces of tested S40 at 300 °C: (a) general view; (b) enlarged view of the interfacial decohesion, where the B_4C particle was out of the matrix; (c) cross-section of the fracture.

5.4 Conclusions

1. With the alloying of Sc and Zr, the hot-rolled Al–15 vol.%B_4C composite sheets can regain a significant precipitation hardening in an appropriate post-rolling heat treatment because of the precipitation of nanoscale Al_3Sc and $Al_3(Sc,Zr)$, which uniformly distribute in the aluminum matrix. After the peak aging, the UTS at ambient temperature of the S40 (Al–15 vol.%B_4C-0.4 wt.%Sc) and SZ40 (Al–15 vol.%B_4C-0.4 wt.%Sc-0.24 wt.%Zr) sheets can reach 197 MPa and 210 MPa, respectively. The tensile strength of both materials decreases with increasing test temperature. The UTSs at 300 ºC of S40 and SZ40 become close and remain at approximately 65 MPa.

2. During 2000 h of annealing at 300 ºC, a slow coarsening process occurs for Al_3Sc (S40) and $Al_3(Sc,Zr)$ (SZ40) precipitates. The strengths at ambient temperature of both S40 and SZ40 composite sheets slightly decrease with increasing annealing time. The UTS at ambient temperature of S40 changes from 197 to 190 MPa, whereas the UTS of SZ40 decreases from 210 to 191 MPa after 2000 h of annealing.

3. The UTS and YS at 300 ºC of both S40 and SZ40 composite sheets remain almost unchanged during 2000 h of annealing, and they are less sensitive to the annealing time and more tolerable for precipitate coarsening, which shows an excellent long-term thermal stability of both materials at elevated temperature.

4. The tensile fracture mechanism of both S40 and SZ40 composite sheets is temperature-dependent. The fracture at ambient temperature is dominated by the brittle B_4C particle fracture, whereas the interfacial decohesion of B_4C particles becomes the prominent characteristic of the fracture at 300 ºC

5.5 References

1. Ibrahim IA, Mohamed FA, Lavernia EJ. Particulate reinforced metal matrix composites - a review. J Mater Sci 1991; 26: 1137-56.

2. Chen XG. Application of Al-B_4C Metal Matrix Composites in The Nuclear Industry for Neutron Absorber Materials. In: Nikhil G, Warren H, editor. Proceedings of Proceedings of solidification processing of metal matrix composites. San Antonio, USA, Conference 2006. p. 343-50.

3. Bonnet G, Rohr V, Chen X-G, Bernier J-L, Chiocca R, Issard H. Use of Alcan's Al-B_4C Metal Matrix Composites As Neutron Absorber Material in TN

International's Transportation and Storage Casks. Packag Transp Stor Secur Radioact Mater 2009; 20: 98-102.

4. Yamazaki T, Sanada K, Nishiyama T, Ishii H. Development of Neutron Absorber (Maxus^{Tm}) for High Burn-Up Spent Nuclear Fuel. In: Proceedings of 15th International Symposium on the Packaging and Transportation of Radioactive Materials (PATRAM 2007). Miami, Florida, USA, Conference 2007. p.1149-54.

5. Maeguchi T, Kamiwaki Y, Ishiko D, Yamamoto T. Development and reliability verification of aluminum alloys for basket of transport and storage cask for spent nuclear fuel. In: Proceedings of 15th International Symposium on the Packaging and Transportation of Radioactive Materials (PATRAM 2007). Miami, Florida, USA, Conference 2007. p.1171-76.

6. Hyland RW. Homogeneous nucleation kinetics of Al_3Sc in a dilute Al-Sc alloy. Metall Mater Trans A 1992; 23: 1947-55.

7. Fuller CB, Seidman DN. Temporal evolution of the nanostructure of Al(Sc,Zr) alloys: Part II-coarsening of $Al_3(Sc_{1-x}Zr_x)$ precipitates. Acta Mater 2005; 53: 5415-28.

8. Yelagin VI, Zakharov VV, Pavlenko SG, Rostova TD. Influence of Zirconium Additions on Aging of Aluminum-Scandium Alloys(Translation). Phys Met Metallogr 1985; 60: 88-92.

9. Riddle YW, Sanders TH. A study of coarsening, recrystallization, and morphology of microstructure in Al-Sc-(Zr)-(Mg) alloys. Metall Mater Trans A 2004; 35: 341-50.

10. Belov NA, Alabin AN, Eskin DG, Istomin-Kastrovskii VV. Optimization of hardening of Al-Zr-Sc cast alloys. J Mater Sci 2006; 41: 5890-9.

11. Fuller CB, Seidman DN, Dunand DC. Creep properties of coarse-grained Al(Sc) alloys at 300°C. Scripta Mater 1999; 40: 691-6.

12. Fuller CB, Seidman DN, Dunand DC. Mechanical properties of Al(Sc,Zr) alloys at ambient and elevated temperatures. Acta Mater 2003; 51: 4803-14.

13. Marquis EA, Seidman DN, Dunand DC. Precipitation strengthening at ambient and elevated temperatures of heat-treatable Al(Sc) alloys. Acta Mater 2002; 50: 4021-35.

14. Lai J, Zhang Z, Chen XG. Precipitation strengthening of Al–B_4C metal matrix composites alloyed with Sc and Zr. J Alloys Compd 2013; 552: 227-35.

15. Qin J, Zhang Z, Chen XG. Mechanical Properties and Strengthening Mechanisms of Al-15 Pct B_4C Composites with Sc and Zr at Elevated Temperatures. Metall Mater Trans A. 2016; 47: 4694-708.

16. Lai J, Zhang Z, Chen XG. The thermal stability of mechanical properties of Al-B_4C composites alloyed with Sc and Zr at elevated temperatures. Mater Sci Eng A 2012; 532: 462-70.

17. Toropova LSED, Kharakterova ML, Dobatkina, TV. Advanced aluminum alloys containing scandium: structure and properties. Moscow, Russia: Gordon and Breach Science Publishers; 1998.

18. Qin J, Zhang Z, Chen XG. Effect of Hot Deformation on Microstructure and Mechanical Properties of Al-B_4C Composite Containing Sc. Mater Sci Forum 2014; 794-796: 821-826.

19. Lloyd D. Aspects of fracture in particulate reinforced metal matrix composites. Acta Mater 1991; 39 :59-71.

20. Llorca J, Martin A, Ruiz J, Elices M. Particulate fracture during deformation. Metall Trans A 1993; 24: 1575-88.

21. Mummery P, Derby B, Scruby C. Acoustic emission from particulate-reinforced metal matrix composites. Acta Mater 1993; 41: 1431-45.

22. Nutt S, Duva J. A failure mechanism in AlSiC composites. Scripta Mater 1986; 20: 1055-8.

23. Kamat S, Hirth J, Mehrabian R. Mechanical properties of particulate-reinforced aluminum-matrix composites. Acta Mater 1989; 37: 2395-402.

24. Whitehouse A, Clyne T. Cavity formation during tensile straining of particulate and short fibre metal matrix composites. Acta Mater 1993; 41: 1701-11.

25. Lai J, Zhang Z, Chen XG. Effect of Sc, Zr, and Ti on the interfacial reactions of the B_4C/Al system. J Mate Sci 2011; 46: 451-9.

26. Kaufman JG. Properties of aluminum alloys: tensile, creep, and fatigue data at high and low temperatures. USA: ASM International 1999.

27. Chen XG, St-Georges L, Roux M. Mechanical Behavior of High Boron Content Al-B_4C Metal Matrix Composites at Elevated Temperatures. Mater Sci Forum 2012; 706-709: 631-7.

28. Tahamtan S, Emamy M, Halvaee A. Effects of reinforcing particle size and interface bonding strength on tensile properties and fracture behavior of Al-A206/alumina micro/nanocomposites. J Compos Mater 2014; 48: 3331-46.

29. Davidson DL. Tensile deformation and fracture toughness of 2014+15vol Pct SiC particulate composite. Metall Mater Trans A 1991; 22: 113-23.

30. Bhanuprasad V, Staley M, Ramakrishnan P, Mahajan Y. Fractography of metal matrix composites. Key Eng Mater 1995; 104: 495-506.

CHAPTER 6

HOT DEFORMATION AND PROCESSING MAPS OF Al–15%B_4C COMPOSITES WITH SC AND ZR

CHAPTER 6

Hot deformation and processing maps of Al–15%B_4C composites with Sc and Zr

6.1 Introduction

Aluminum-based metal matrix composites (MMCs) have gained popularity in industries due to their lightweight, high strength and specific modulus, low coefficient of thermal expansion and good wear resistance compared to aluminum alloys [1]. The development of Al–B_4C composites has recently attracted a great attention, which can serve as neutron absorber material in transportation and storage of spent nuclear fuels in the nuclear industry as boron carbide (B_4C) has high cross-section for neutron absorption [2,3]. The introduction of Sc and Zr into Al–B_4C composites can increase the composite strength at elevated temperature by forming stable precipitates [4-6]. To manufacture a useful

engineering product, most Al-based metal matrix composites are subjected to hot forming processes such as rolling, extrusion and forging. The mechanical properties of those composites are affected by their chemical composition and resultant microstructure from thermomechanical processing.

Several investigations found that dynamic precipitation (DPN) occurred during hot deformation in 2xxx, 6xxx and 7xxx series Al alloys [7-13]. The precipitation and subsequent coarsening can affect the flow curve and increase the flow stress level [14]. The precipitates formed during hot deformation were reported to restrain dynamic recrystallization (DRX) and increase the activation energy for hot deformation [7]. It was reported that Sc and Zr could increase recrystallization resistance by forming $L1_2$ structure precipitates [15-19]. The fine precipitates of Al_3Sc could inhibit the migration of grain and sub-grain boundaries and the dislocation movement, thereby, restraining the recrystallization and resulting in a high work hardening stress [20-25]. On the other hand, the hot deformation behaviors of Al-based MMCs were also influenced by reinforcement

particles, thermal residual stress [29], flow localization [30] and deformation incompatibility between matrix and enforcement particles [31].

Constitutive equations are generally employed to predict the flow behavior of materials [32] and to calculate their activation energies [33]. The hot deformation activation energy Q is an important physical parameter that represents the difficulty level during hot deformation. The activation energy for hot deformation of pure Al was reported to be 144 kJ/mol [34]. The activation energy for an Al–5 wt.% B_4C composite was found to be 200.1 kJ/mol [35], which was higher than pure Al due to the presence of enforcement particles. In addition, the processing maps based on dynamic material model (DMM) have been widely employed to gain the optimum flow stability region and avoid the instability region [36]. Li *et al*. [37] studied the processing maps of a 6061 Al–B_4C composite in a wide range of temperatures and strain rates. Gangolu *et al*. [35] reported the hot workability of an Al-B_4C composite and proposed the optimum processing conditions in the form of processing map.

The mechanical properties and microstructure evolution of Al–B_4C composites containing Sc and Zr have been studied in our previous works [38-43]. The present work focused on the thermomechanical processing aspect of Al–B_4C composites containing Sc and Zr. The hot deformation behavior of three Al–B_4C composites, namely the base composite (Al-15vol.%B_4C), S40 (Al-15vol.%B_4C-0.4wt.%Sc) and SZ40 (Al-15vol.%B_4C-0.4wt.%Sc-0.24wt.%Zr), was investigated by hot compression tests performed at various temperatures and strain rates. The constitutive equations and activation energies related to the peak flow stress, deformation temperature and strain rate were analyzed.. The processing maps of three Al–B_4C composites were established to optimize the hot working processing. The deformation mechanisms were determined for both the flow stability and instability regions based on the microstructure observation using optical and scanning electron microscopies.

6.2 Experimental procedure

Three Al-B_4C composites, namely the base composite, S40 and SZ40, were investigated in the present study. Their nominal chemical compositions are listed in Table 3.1. In the composite preparation process, commercially pure aluminum (99.7 %) was first melted in a graphite-chamotte crucible in an electric resistance furnace. Master alloys Al-2 wt.% Sc, Al-15 wt.% Zr and Al-10 wt.% Ti were later added into the molten aluminum and the melt was held at 800 °C for 40 minutes to dissolve the master alloys. The prefabricated Al−25 vol.%B_4C with 2.0 wt.% Ti cast ingots, supplied by Rio Tinto Aluminum, was then put into the alloyed melt. The average size of the B_4C particles (F360) was 23 μm. Under mechanical stirring using an impeller, the composite melts were held at 740 °C for 30 minutes and then cast into a rectangular permanent steel mold. The dimensions of the cast ingots are 30×40×80 mm.

The cast ingots of S40 and SZ40 composites were heat treated at 640°C for 24 hours and 96 hours, respectively, followed by direct water quenching. The base composite was

not heat-treated because of its non-heat-treatable 1100 matrix. The ingots were machined to cylindrical specimens, 10 mm in diameter and 15 mm in length, for compression tests. The compression tests were carried out using a Gleeble-3800 thermo-mechanical simulation unit at strain rates of 0.001, 0.01, 0.1 and 1 s^{-1} and deformation temperatures of 300, 350, 400, 450 and 500 ºC, respectively. During the compression tests, all specimens were heated to the desirable deformation temperature at a heating rate of 10 °C/s and held for 3 minutes to ensure the uniform temperature in the specimen. The specimens were deformed to a total true strain of 0.8.

For microstructure characterization, the deformed samples were cut parallel to the compression direction along the centerline. The samples were metallographically prepared and then etched by 2% HF solution for 2 minutes for optical microstructure observation. Moreover, some deformed samples were analyzed using the electron back-scattered diffraction (EBSD) under a scanning electron microscope (SEM, JEOL JSM-6480LV) to understand the softening mechanisms of the composites in hot deformation process.

6.3 Results and Discussion

6.3.1 Flow stress behaviors

A series of typical true stress-strain curves of the base composite, S40 and SZ40 at various deformation temperatures and the strain rates are presented in Fig. 6.1. Under all the test conditions, the flow stress had a rapid increasing stage at the beginning of the deformation, which is due to the predominate effect of work hardening. In this stage, multiplied dislocations and reactions among dislocations, defects and particles result in a large increase of dislocation migration resistance with increasing the strain. With further increasing the strain, the increase rate of flow stress gradually decreased and the flow stresses either remained fairly constant or attain a maximum stress value before the flow stress decreased when the deformation were performed at 350, 400, 450 and 500 ºC. During this stage, dynamic softening processes become operative and both dynamic softening and work hardening contribute more and less equally to the flow stress. However, at the low compression temperature of 300 ºC, the flow stresses slowly but continuously increase after

the beginning stage (Fig. 6.1). In the present study, the peak stress is defined at the constant stress value for the case that the flow stresses remained constant after a rapid increasing stage. For other cases, the maximum flow stress values in the flow curves is considered as the peak stress in the following discussion. Generally, the flow stress and peak stress of three composites decreased with increasing deformation temperature and with decreasing strain rate. The same tendencies were observed in the previous research works on Al metal matrix composites [7,33,44-47].

With the increase of deformation temperature, the bonding between atoms in the composite matrix decreases and the load transfer from the matrix to ceramic particles becomes weak [48], which directly weakens the flow stress. In addition, the high deformation temperature promotes atom diffusion and accelerating dislocation and grain boundary migrations, which results in a weaker work hardening and a stronger of dynamic softening. On the other hand, a low strain rate is favor to the atom diffusion and dislocation migration, encouraging dynamic softening (DRX and DRV) [49]. Thus, on the effect of

both high temperature and low strain rate, a lower flow stress and an earlier arrival of the steady state are reflected in the flow stress curves.

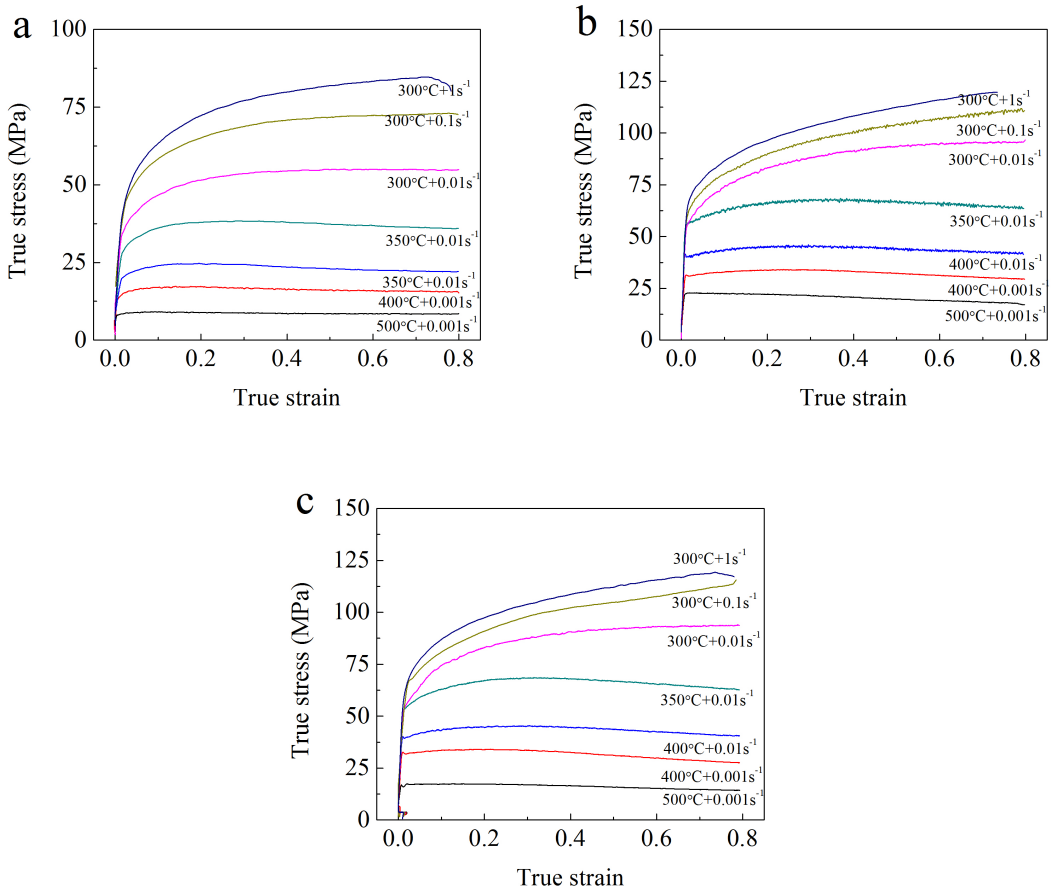

Fig. 6. 1. Typical true stress–strain curves during hot deformation: (a) the base composite, (b) S40 and (c) SZ40 composites.

Fig. 6.2 illustrates the evolution of the peak stresses of the three composites at various deformation temperatures as a function of strain rate. In general, the peak stresses of the

base material are obviously lower than that of S40 and SZ40 composites, while both peak stresses of S40 and SZ40 composites are close in all experimental conditions tested. For example, at 300 ºC with 0.001 s-1 strain rate, the peak stress of the base composite was 46 MPa, but the peak stresses of S40 and SZ40 were 76 MPa and 78 MPa, respectively. When the strain rate increased to 1 s-1 at the same temperature (300 ºC), the peak stress of the base composite was 82 MPa, but it reached 119 MPa for S40 and 120 MPa for SZ40. The same tendency of the peak stress evolution is observed in all deformation temperatures tested (Fig. 6.2). The experimental data indicate that the addition of Sc and Zr can remarkably enhance the deformation resistance during hot deformation at the temperatures from 300 to 500ºC.

At the low deformation temperature (300ºC), the peak stresses of S40 were slightly lower than that of SZ40, and the stress differences were around 1 to 6 MPa with various strain rates (Fig. 6.2a). However, at the high deformation temperature (500ºC), the peak stresses of S40 were moderately higher than those of SZ40 (Fig. 6.2e). On the other hand,

when the deformation temperatures were at 350-450 ºC, the difference of the peak flow stresses between the two composites were almost negligible (Fig. 6.2b-d).

After the solution treatment of S40 and SZ40 samples before hot deformation, most Sc and Zr were dissolved in the composite matrix. At the deformation temperature below 400 ºC, there is no any precipitate (Al_3Sc and $Al_3(Sc,Zr)$ found in deformation microstructure of S40 and SZ40, which means that Sc and Zr solute atoms act as the barriers of dislocation movement at low deformation temperatures. At high deformation temperatures (450-500 ºC), Al_3Sc and $Al_3(Sc, Zr)$ precipitates were observed in deformed microstructure of S40 and SZ40 samples, indicating that dynamic precipitation occurred during preheating and hot deformation. Similar phenomenon was reported in other precipitation strengthening aluminum alloys [10,11]. This results in that the flow stresses of S40 and SZ40 are always higher than that of the base composite at all deformation conditions, because the addition of Sc and Zr hinder the dislocation migration either as solute atoms at low temperatures or as precipitates at high temperatures.

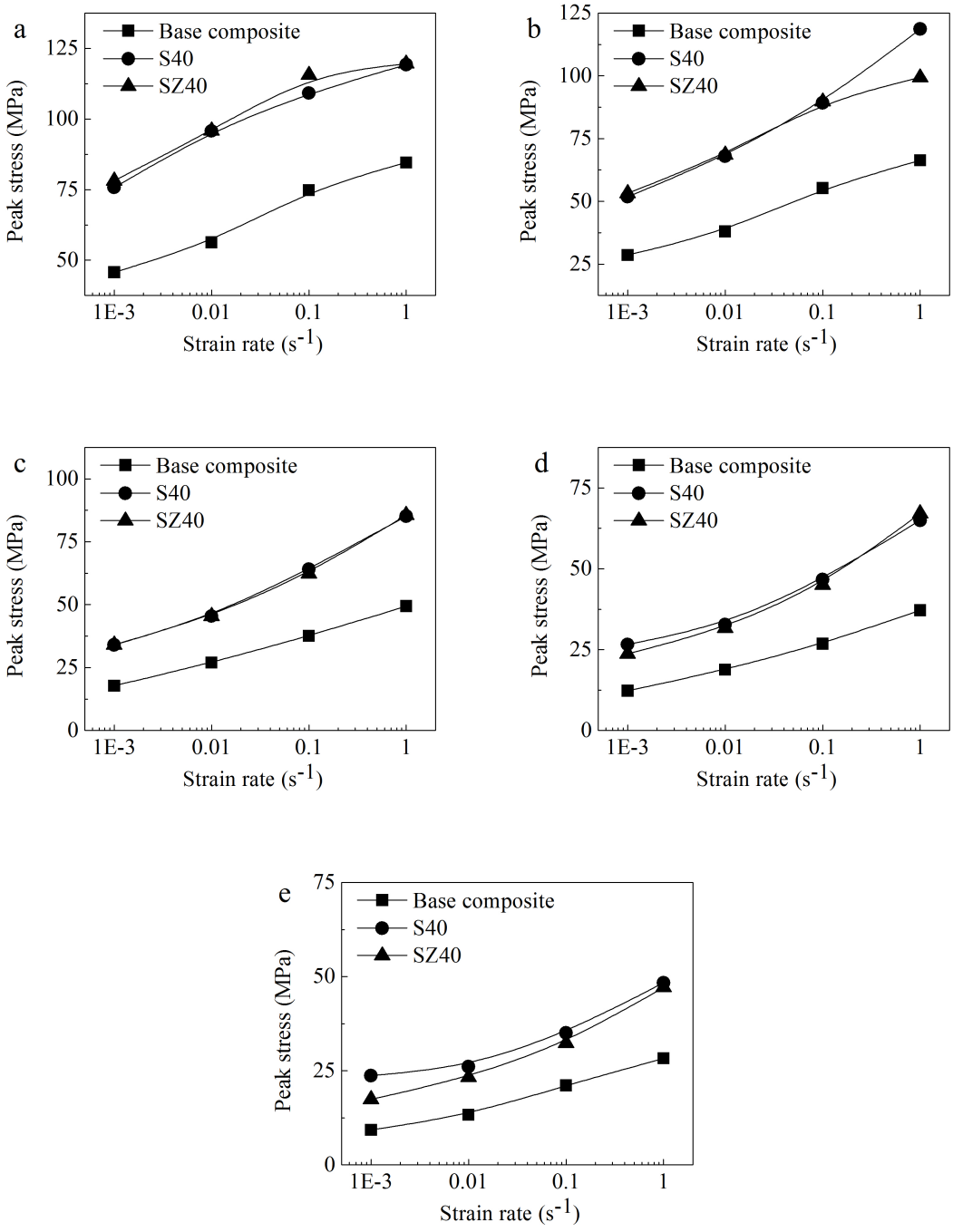

Fig. 6. 2. The evolution of peak stress of Al−B_4C composites at various temperatures as a function of strain rate: (a) 300 ºC, (b) 350 ºC, (c) 400 ºC, (d) 450 ºC and (e) 500 ºC.

6.3.2 Constitutive analyses

The hyperbolic-sine equation is usually applied to describes the relationship between strain rate, flow stress and deformation temperature for a large range of strain rate and stress levels [32].

$$\dot{\varepsilon} = A\left[\sinh(\alpha\sigma)\right]^{n} \exp\left(-Q/RT\right) \qquad \text{Eq. 6. 1}$$

Where, $\dot{\varepsilon}$ is the strain rate (s^{-1}); σ is the flow stress (MPa); T is the absolute temperature (K); R is the universal gas constant (8.314 $J \cdot mol^{-1}K^{-1}$); and Q is the activation energy for hot deformation ($kJ \bullet mol^{-1}$), which implies the levels of deformation resistance during plastic deformation. Where *A*, *n* and α are material constants.

To obtain the materials constants and hot deformation activation energy, Eq. 6.2 is inducted by taking nature logarithm and differentiating Eq. 6.1:

$$Q = R\left[\frac{\partial \ln \dot{\varepsilon}}{\partial \ln\left[\sinh(\alpha\sigma)\right]}\right]_{T}\left[\frac{\partial \ln\left[\sinh(\alpha\sigma)\right]}{\partial(1/T)}\right]_{\dot{\varepsilon}} = RnS \qquad \text{Eq. 6. 2}$$

The experimental data from the base composite, as an example, are shown in Fig. 6.3 to demonstrate the derivation of materials constants and the calculation of activation energy for hot deformation. The peak stress σ_p is used here for σ, which represents the equilibrium condition between the work hardening and dynamic softening. Then α can be deduced by the division result of β and n_1, which are the materials constants related to hot deformation [32]. The values of n_1 and β for the composites can be obtained from the mean slopes of the lines in the $\ln\dot{\varepsilon}$ vs. lnσ (Fig. 6.3a) and $\ln\dot{\varepsilon}$ vs. σ (Fig. 6.3b), respectively. Here n is the mean slop of plots of $\ln\dot{\varepsilon}$ vs. $\ln\left[\sinh(\alpha\sigma)\right]$ at different temperatures (Fig. 6.3c). S is the mean slopes of $\ln\left[\sinh(\alpha\sigma)\right]$ vs. 1/T at various strain rates (Fig. 6.3d). Where the A can be obtained from the intercept of $\ln\left[\dot{\varepsilon}\exp(Q/RT)\right]$ vs. $\ln\left[\sinh(\alpha\sigma)\right]$ (Fig. 6.3e) [32].

Based on the above description and Eqs. 6.1 and 6.2, the calculated material constants A, n, α and the activity energy Q of the three composites are presented in Table 6.1. It is known that when the n is greater than 5, it indicates a climb-controlled dislocation deformation [50]. The n of three composites ranges from 5.17 to 6.70, which implies that

the dislocation climb is the operative mechanism for three experimental composites during hot deformation. It is in good agreement with the previous work [38].

The activation energy for hot deformation Q is an important physical parameter that represents the difficulty level in hot deformation. The activation energy of the base composites is calculated to be 186.4 kJ/mol (Table 6.1). With addition of Sc and Zr (0.4% Sc in S40 and 0.4% Sc plus 0.24%Zr in SZ40), the values of the activation energy increase to 196.1 kJ/mol for S40 and 206.6 kJ/mol for SZ40, respectively, indicating that Sc and Zr in Al-B_4C composites considerably increase the hot deformation resistance. This is most likely associated with the high solute level and dynamic precipitation of Z40 and SZ40. It is well known that the activation energy for hot deformation of materials increases with increasing solute level [10,51]. Solute atoms can diffuse to dislocations act as pins to either restrict dislocation migration or drag a dislocation during slipping. On the other hand, the precipitates also increase the activation energy due to the precipitate strengthening effect

[10,11,52]. Compared to S40, SZ40 has more solute atoms and more change to dynamic precipitation, resulting a higher activation energy value than S40.

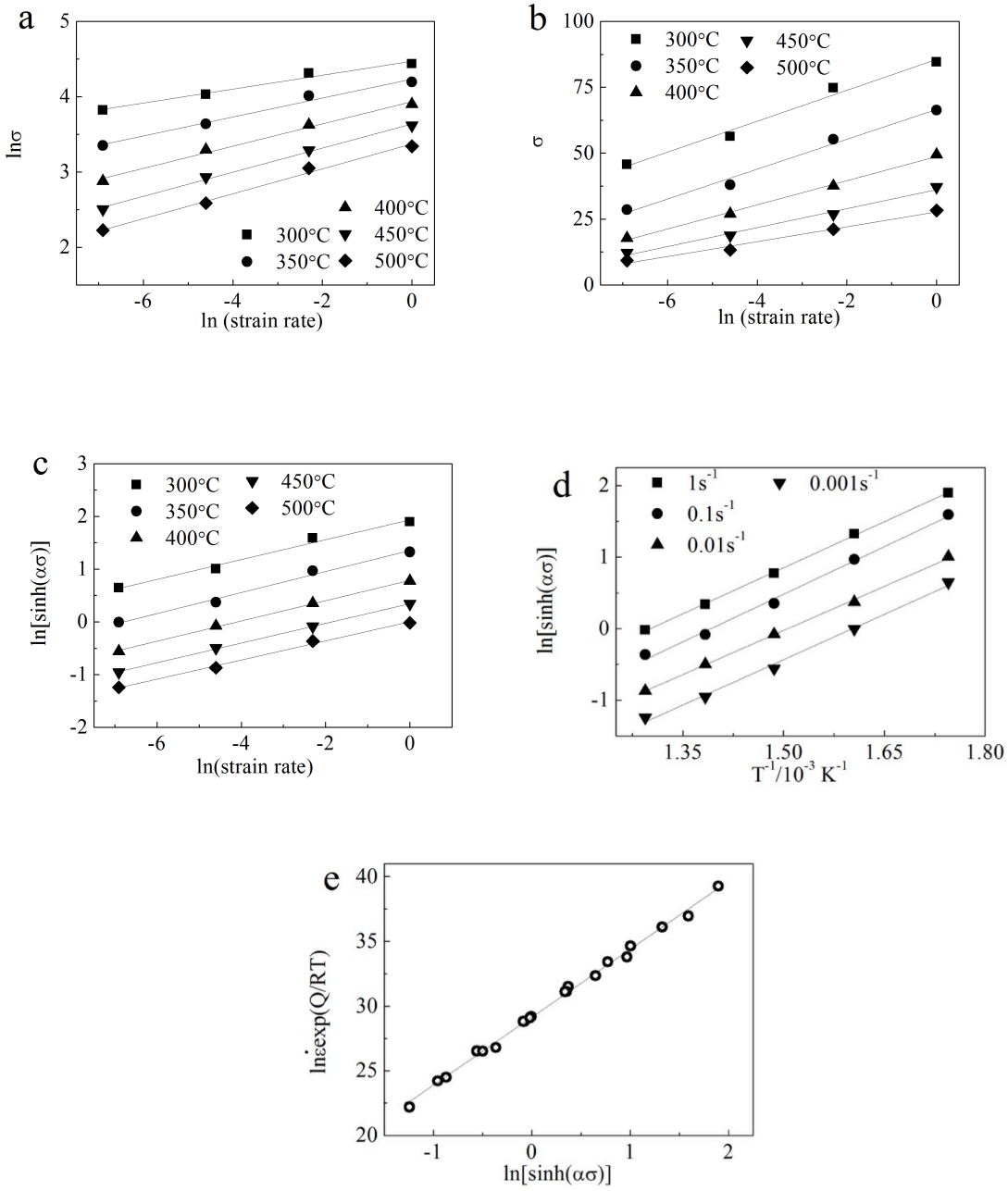

Fig. 6. 3. Relationships between flow stress and strain rate for the base composite, (a) $\ln \dot{\varepsilon}$ vs. lnσ, (b) $\ln \dot{\varepsilon}$ vs. σ, (c) $\ln \dot{\varepsilon}$ vs. $\ln\left[\sinh(\alpha\sigma)\right]$, (d) T^{-1} vs. $\ln\left[\sinh(\alpha\sigma)\right]$ and (e) $\ln\left[\dot{\varepsilon}\exp(Q/RT)\right]$ vs. $\ln\left[\sinh(\alpha\sigma)\right]$.

Table 6. 1. Values of the material constants and activation energy for the composites studied.

Composites	α (MPa^{-1})	n	A (s^{-1})	Q ($kj \cdot mol^{-1}$)
Base	0.032	5.17	0.45×10^{13}	186.4
S40	0.017	6.70	1.30×10^{13}	196.1
SZ40	0.017	6.51	3.89×10^{13}	206.6

The effect of deformation temperature and strain rate on hot deformation behavior can be expressed by Zener-Holloman parameter, Z, as shown in Eq. 6.3 [53].

$$Z = \dot{\varepsilon}\exp\left(Q/RT\right) = A\left[\sinh(\alpha\sigma)\right]^{n} \qquad \text{Eq. 6. 3}$$

Then, the flow stress σ can be described as a function of Z parameter based on the definition of hyperbolic sine function:

$$\sigma = \frac{1}{\alpha}\ln\left\{\left(\frac{Z}{A}\right)^{1/n} + \sqrt{\left[\left(\frac{Z}{A}\right)^{2/n} + 1\right]}\right\} \qquad \text{Eq. 6. 4}$$

Hence, the relationship between flow stress, strain rate, and deformation temperature of the three composites can be expressed in Eqs. 6.5 to 6.7 based on Eq. 6.4 and the materials constants listed in Table 6.1:

$$\sigma_{base} = 31.25\ln\left\{\left(\frac{\dot{\varepsilon}\exp\left(186.4/RT\right)}{0.45\times10^{13}}\right)^{0.19} + \sqrt{\left[\left(\frac{\dot{\varepsilon}\exp\left(186.4/RT\right)}{0.45\times10^{13}}\right)^{0.39} + 1\right]}\right\} \qquad \text{Eq. 6. 5}$$

$$\sigma_{S40} = 58.8\ln\left\{\left(\frac{\dot{\varepsilon}\exp\left(196.1/RT\right)}{1.3\times10^{13}}\right)^{0.15} + \sqrt{\left[\left(\frac{\dot{\varepsilon}\exp\left(196.1/RT\right)}{1.3\times10^{13}}\right)^{0.30} + 1\right]}\right\} \qquad \text{Eq. 6. 6}$$

$$\sigma_{SZ40} = 58.8\ln\left\{\left(\frac{\dot{\varepsilon}\exp\left(206.6/RT\right)}{3.89\times10^{13}}\right)^{0.15} + \sqrt{\left[\left(\frac{\dot{\varepsilon}\exp\left(206.6/RT\right)}{3.89\times10^{13}}\right)^{0.31} + 1\right]}\right\} \qquad \text{Eq. 6. 7}$$

Using the established constitutive equations (Eqs. 6.5−6.7), the predicted peak flow stresses vs. the experimental data for three composites are plotted in Fig. 6.4. The predicted

peak stresses show a good agreement with the experimental peak stresses and the correlation coefficient is 99.6%, 97.3% and 98.3% for the base composite, S40 and SZ40, respectively, which indicate that the established constitutive equations (Eqs. 6.5−6.7) can give an accurate estimation of peak stress values for the three composites.

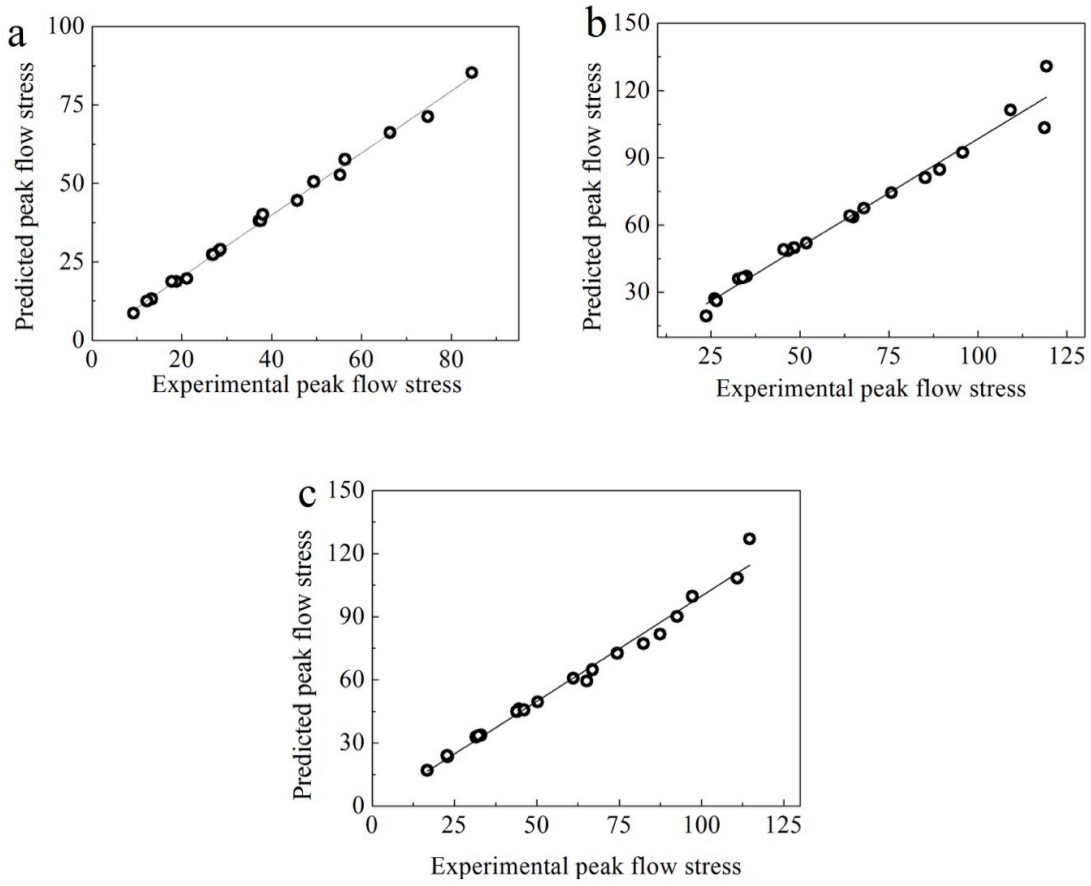

Fig. 6. 4. Predicted peak flow stress vs. experimental peak flow stress from the established constitutive equations: (a) the base composite, (b) S40 and (c) SZ40.

6.3.3 Processing maps

The hot workability on plastic deformation can be characterized base on dynamic material model (DMM) [54]. In this model, the power dissipation is applied to describe the hot deformation behaviors of materials. The efficiency of power dissipation η presents the energy dissipated through the evolution of metallurgical mechanisms during the hot deformation, which is given by Eq. 6.8.

$$\eta = \frac{2m}{2m+1} \qquad \text{Eq. 6. 8}$$

Where m is strain rate sensitivity of the materials determined by Eq. 6.9, which is varied with temperature and strain rate for composites [55]

$$m = \left(\frac{\partial \ln \sigma}{\partial \ln \dot{\varepsilon}} \right)_{T,\varepsilon} \qquad \text{Eq. 6. 9}$$

In generally, the higher efficiency of power dissipation, the more power is considered to be dissipated by microstructure evolution, which implies a better hot workability. On the other hand, flow instability such as flow localization, shear bands, microcracks etc. could occur under certain deformation conditions during the deformation. Flow instability could be predicted according to the continuum instability criterion shown as Eq. 6.10 [56]:

$$\xi(\dot{\varepsilon}) = \frac{\partial \ln\left(m/m+1\right)}{\partial \ln \dot{\varepsilon}} + m \leq 0 \qquad \text{Eq. 6. 10}$$

Therefore, the deformation parameters have to select the ones where the ξ is larger than zero during the plastic deformation.

To describe the relationship between hot workability and flow instability, the contour plots of the iso-efficiency of power dissipation η and the iso-flow instability ξ as a function of temperature and strain rates can be plotted together to construct the processing map. Fig. 6.5 shows the processing maps developed for three composites at the true strain of 0.8. The values of the power dissipation efficiency η are shown as contour numbers, while the shaded area denotes the instability regions. A safe domain should have higher dissipation efficiency and avoid instability regions in the process map. The recommended safe domains based on power dissipation efficiency and flow instability are shown in Fig. 6.5 and the corresponded values are listed Table 6.2. For the base composite, the processing map exhibits three safe domains (Fig. 6.5a). Domain I with the power dissipation efficiency of 0.27-0.30 is located at the temperatures of 475-500 °C and the strain rates of 0.1-1 s^{-1}. Domain II with the power dissipation efficiency of 0.27-0.28 is on the region with lower

temperatures and lower strain rates (330-400 °C/0.007-0.001 s^{-1}), while Domain III has the same power dissipation efficiency as Domain II but its working region is toward higher temperatures (420-470 °C). For S40, there are two safe domains (Fig. 6.5b): one with the power dissipation efficiency of 0.26-0.28 at the zone having higher temperatures (400-500 ºC) and higher strain rates (0.11-1 s^{-1}) and another one with the efficiency of 0.26 with lower temperatures (340-380 ºC) and lower strain rates (0.01-0.001 s^{-1}). The two safe domains in SZ40 are similar to those in S40 (Fig. 6.5c). Compared three processing maps in Fig. 6.5, the domains I of S40 and SZ40 are situated at the similar zone as the domain I of the base composite, but they expand toward lower temperate with lower efficiency. The processing ranges of the domains II of S40 and SZ40 are also similar to the domain II of the base composite. However, the base composite possesses another additional safe domain (III) at the low strain rates, indicating a better hot workability than S40 and SZ40 composites.

The flow instability region of the base composite covered from 300 to 350 °C at high strain rates of 0.04 to 1 s^{-1} (Fig. 6.5a). With the addition of Sc, the flow instability region of S40 expanded toward lower strain rate, which was situated from 300 to 350 °C at low strain rates of 0.002 to 1 s^{-1} (Fig. 6.5b). Moreover, with addition of Sc and Zr, the flow instability region of SZ40 even became larger than that of S40 and it extended up to the temperature of 380 °C (Fig. 6.5c). This indicates that the addition of Sr and Zr remarkably decreases the processing window of hot deformation. It is evident that the flow instability regions in all three composites present lower values of power dissipation efficiencies, compared with the adjacent stable regions. Therefore, the processing parameters should not be chosen in the instability region of those composites to obtain good hot workability and to prevent the occurrence of deformation defects.

Table 6.2. Safe processing domains of three composites.

Composites	High strain rate domains (I)		Low strain rate domains (II & III)	
Base	475−500 °C	0.05−1 s^{-1}	330−400 °C	0.007−0.001 s^{-1}

			420−470 °C	0.008−0.001 s^{-1}
S40	400−500 °C	0.11−1 s^{-1}	340−380 °C	0.010−0.001 s^{-1}
SZ40	400−500 °C	0.11−1 s^{-1}	327−390 °C	0.007−0.001 s^{-1}

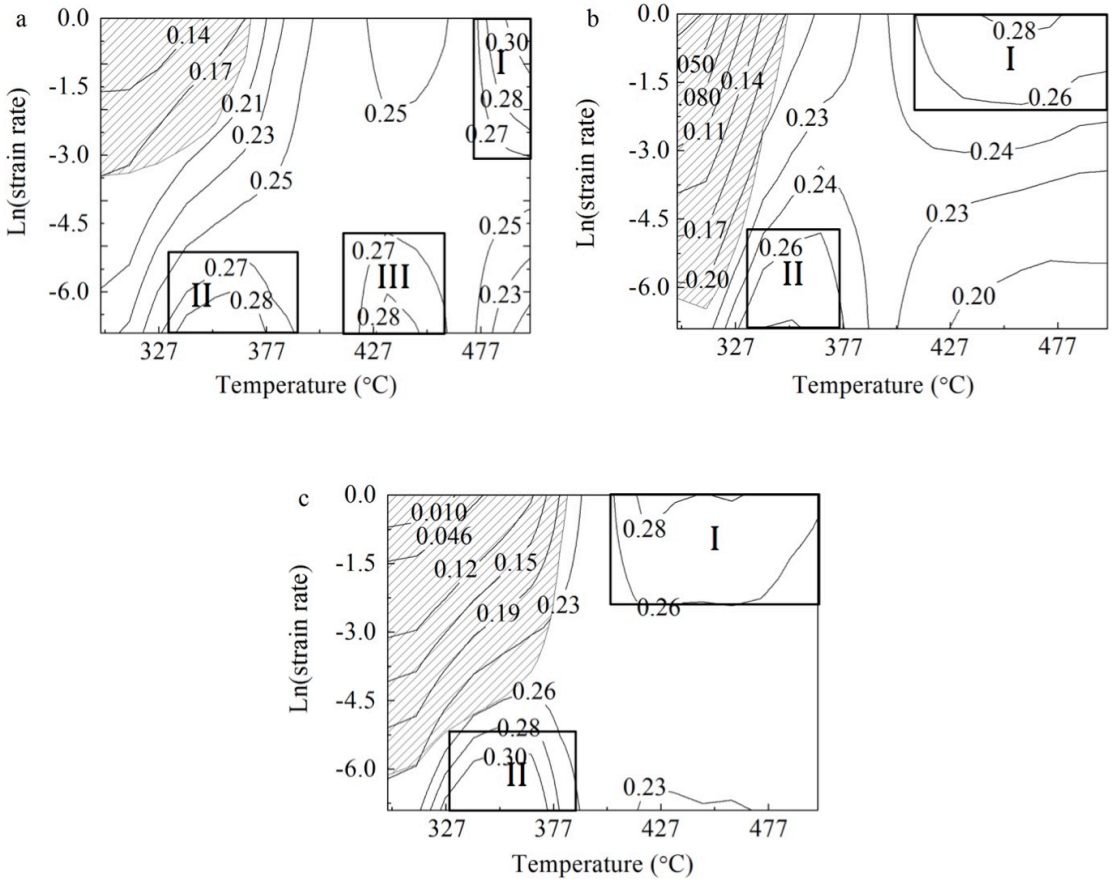

Fig. 6. 5. Processing maps of three composites developed at the true strain of 0.8: (a) the base composite, (b) S40 and (c) SZ40.

6.3.4 Microstructure evolution

6.3.4.1 Deformed microstructures at various deformation conditions

Fig. 6.6 shows the optical micro images of three composites deformed at 300ºC and 1 s^{-1}. The original as-cast equiaxed grains [32] were greatly elongated and severe deformation bands (the arrows in Fig. 6.6) were present. Those deformation bands did not distribute uniformly and more deformation bands concentrated near B_4C particles, which indicated that B_4C particles cause the local stress concentration. EBSD orientation maps were used to understand the dynamic softening mechanisms during hot deformation. The orientation maps of the base composite and SZ40, as examples, are shown in Fig. 6.7. A large amount of dislocation cells and subgrains with low-angle boundaries of 1-15º appeared in the base and SZ40 composites, which were typically recovered microstructure. There was a small amount of recrystallized grains with a small size of 1-3μm along the grain boundaries in the matrix of the base composite (Fig. 6.7a). In SZ40, the recrystallized grains were hardly

found in the matrix. In overall, the predominate softening mechanism is dynamic recovery for the three composites deformed at the low temperature of 300 ºC.

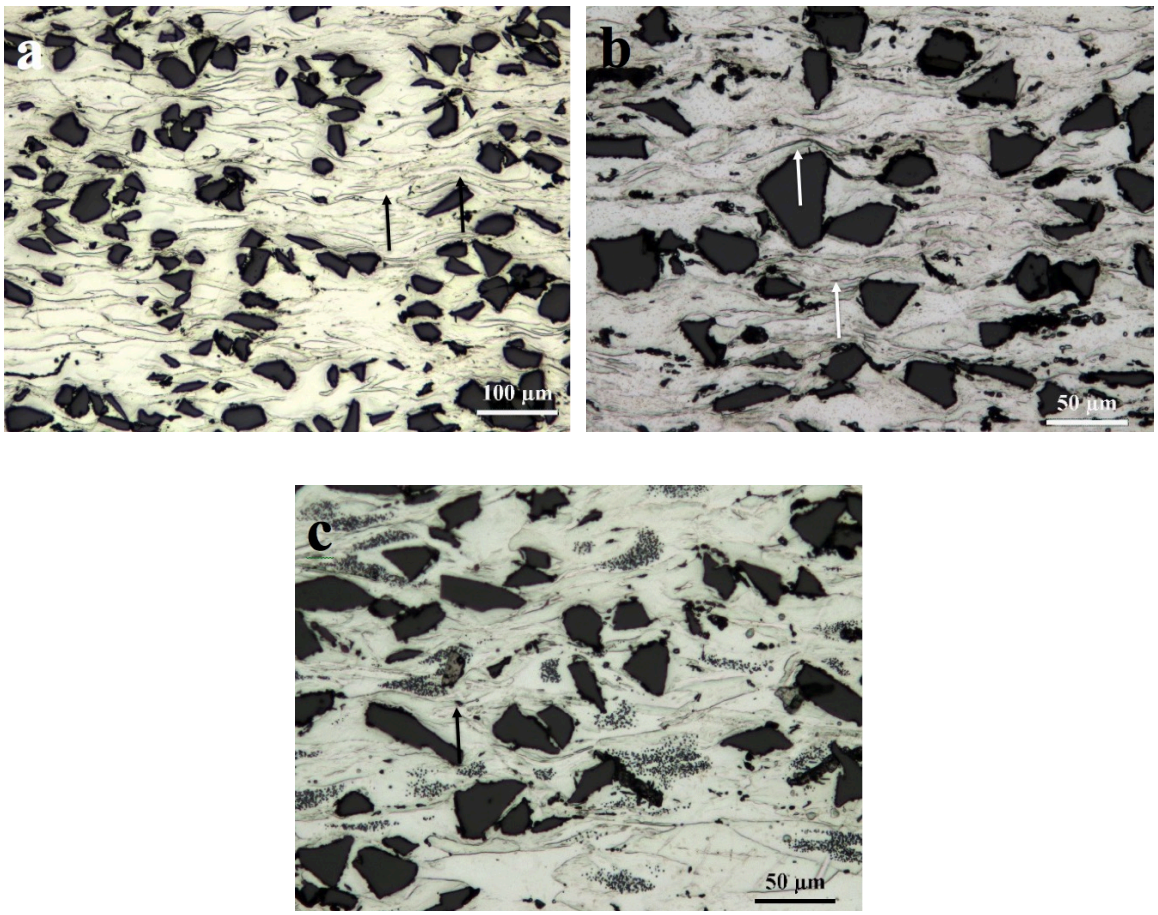

Fig. 6. 6. Optical microstructures deformed at 300 ºC and 1 s^{-1} with a true strain of 0.8: (a) base composite, (b) S40 and (c) SZ40 composites.

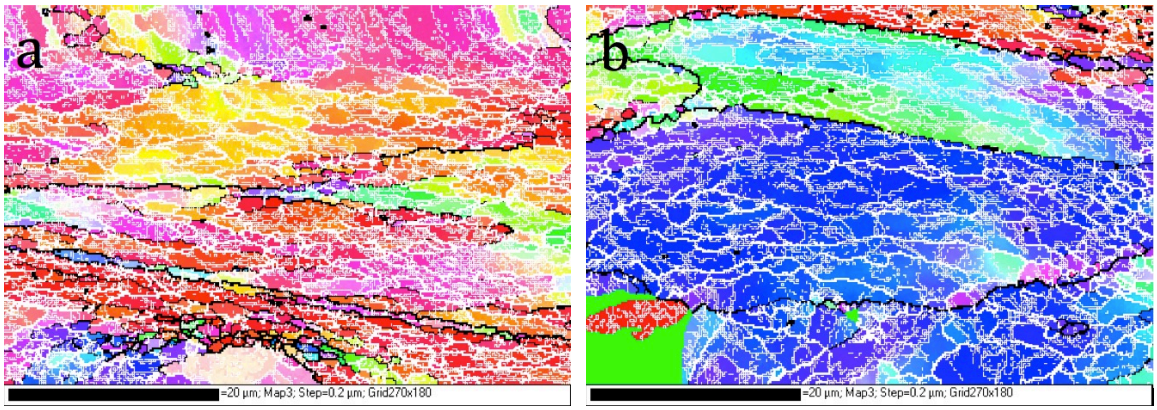

Fig. 6. 7. EBSD orientation maps deformed at 300ºC and 1 s^{-1}: (a) the base composite, (b) SZ40 composite Boundary misorientation as indicated: thin white lines: 1~5°; thick white lines: 5~15°; black lines: >15°.

When deformed at higher temperature (500ºC and 1 s^{-1}), a number of recrystallized grains with a size range of 5-50 µm appeared in the base composite samples (arrows in Fig. 6.8a), while only a few recrystallized grains with a small size of 1-3 µm presented in S40 and SZ40 samples (Fig. 6.8b). EBSD orientation maps confirmed that the deformed microstructure in S40 and SZ40 primarily were recovered structure (Fig. 6.9), indicating that the addition of Sc and Zr impeded the recrystallization in the Al-B_4C composites. In addition, when deformed at 500 ºC with a lower strain rate of 0.001 s^{-1}, the microstructure of the base composite remained the recrystallized structure but the recrystallized grains had

larger size than those deformed at 500 ºC and 1 s^{-1}. For S40 and SZ40, the deformed microstructure primarily remained as dynamically recovered structure but a small amount of fine recrystallized grains inhomogeneously distributed along the deformation bands under the deformation condition at 500 ºC with a lower strain rate 0.001 s^{-1}. Therefore, it can be concluded that dynamic recrystallization (DRX) is the main softening mechanism for the base composite deformed at 500 ºC, while the predominant softening mechanism was dynamic recovery (DRV) for S40 and SZ40 at 500 ºC.

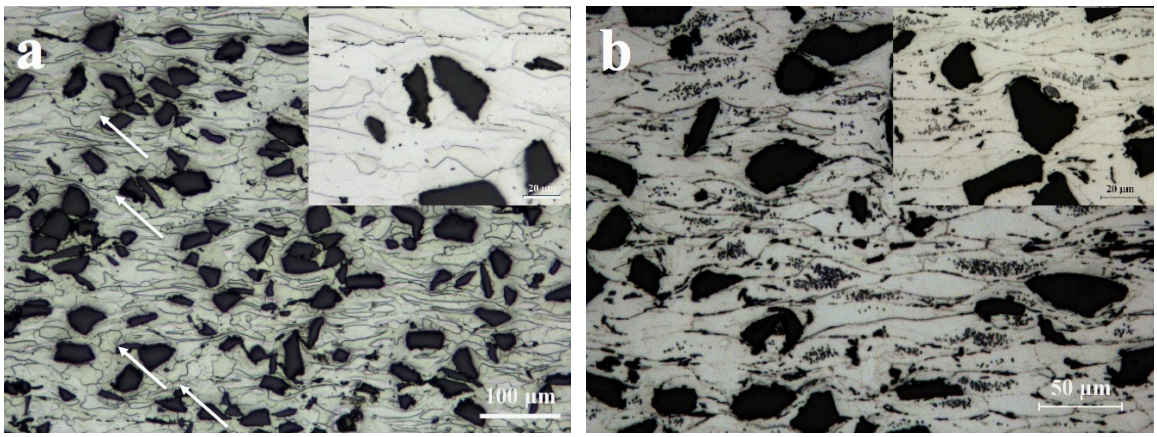

Fig. 6. 8. Optical microstructures deformed at 500 ºC and 1 s^{-1} with a true strain of 0.8: (a) the base composite and (b) SZ40 composite.

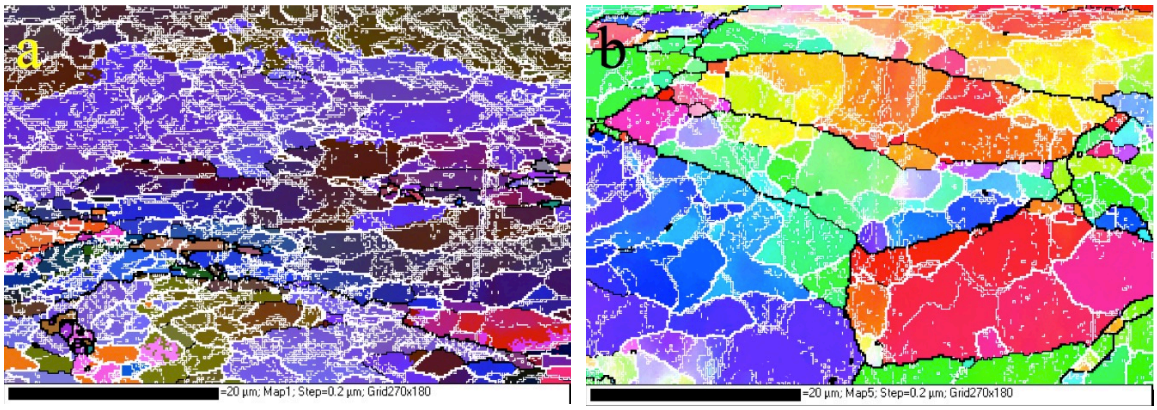

Fig. 6. 9. EBSD orientation maps deformed at 500 ºC and 1 s^{-1} with a true strain of 0.8: (a) S40 and (b) SZ40 composites.

6.3.4.2 Microstructure features in flow stability and instability domains

The safe domains I in the processing maps of three composites (Fig. 6.5) were all located in the zone with high temperature (400-500 ºC) and high strain rate (0.1-1 s^{-1}). The typical microstructures of the domains I were the same shown in Figs. 6.8 and 6.9. It is evident that in the domain I, DRX was the main softening mechanism for the base composite and DRV was the predominant softening mechanism for S40 and SZ40.

The typical microstructures in the safe domains II of three composites are shown in Fig. 6.10. Deformed at 350ºC and 0.001 s^{-1} (Fig. 6.10a), the microstructure of the base composite consisted of a large amount of dislocation cells and subgrains with low-angle boundaries of 1-15° and a few of recrystallized grains, which indicated that DRV mainly

controls the softening process. The microstructures of the base composite in the domain III is similar to that in the domain II, but the size of recrystallized grains in the domain III is slightly larger than that in domain II. The deformed microstructures of S40 and SZ40 in the domains II were primarily recovered structure. For example, the microstructure of SZ 40 deformed at 350ºC and 0.001 s^{-1} exhibited mainly elongated grains with a number of cells and subgrains (Fig. 6.10b). Hence, the main softening mechanism in the safe domains II and III of the base material as we as the safe domains II of S40 and SZ40 composites was DRV.

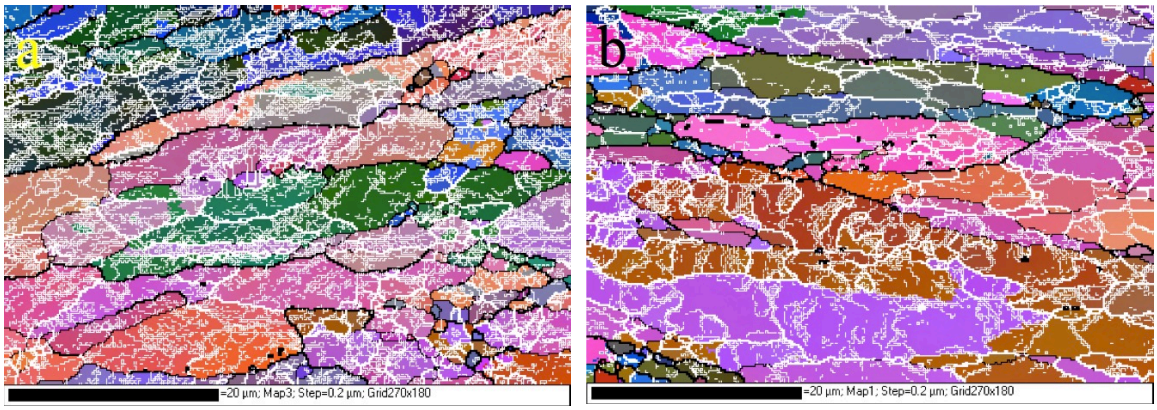

Fig. 6. 10. Typical EBSD orientation maps in the safe domain II under the deformation condition at 350 ºC and 0.001 s^{-1}: (a) the bas composite and (b) SZ40**.**

The flow instability region of the base composite was located at low temperature (300-350 ºC) with high strain rate of 0.04-1 s^{-1} and the instability regions of S40 and SZ40 extended toward the higher temperature up to 380 ºC and the lower strain rate up to 0.002-1 s^{-1} (Fig. 6.5). The deformation defects such as voids and cracks were observed in the flow instability zones of deformed samples. Fig. 6.11 shows some examples of deformed microstructures with the deformation condition at 300 ºC and 1 s^{-1} for the base composite and SZ40 (Fig. 6.11a and c) and at 300 ºC and 0.01 s^{-1} for S40 (Fig. 6.11b), located in the flow instability regions. Except for the deformation bands and elongated grains in the matrix, the deformation defects such as voids, cracks and flow localization were often observed around B_4C particles (arrows in Figs. 6.11a, b and c). It is suggested that the defect formation is the major cause for the flow instability during hot deformation of Al-B_4C composites.

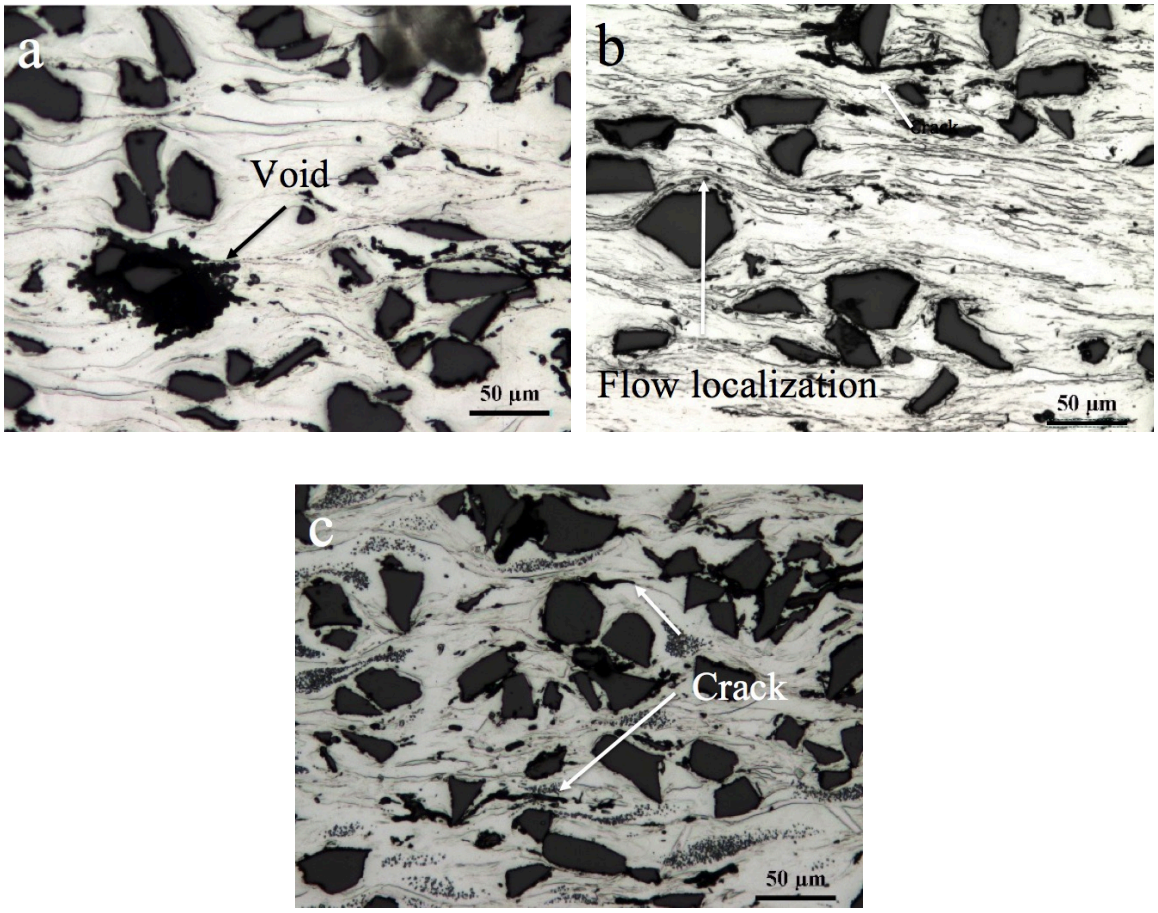

Fig. 6. 11. Microstructures of (a) the base composite deformed at 300 ºC and 1 s^{-1}, (b) S40 deformed at 300 ºC and 0.01 s^{-1} and (c) SZ40 deformed at 300 ºC and 1 s^{-1}.

6.4 Conclusions

1. The flow stress increased with the increase of the strain rate and the decrease of the deformation temperature during hot deformation. The addition of Sc and Zr

in Al-15%B_4C composites increased the flow stress, which was attributed to the synthetic effect of solute atoms and dynamic precipitation.

2. With addition of Sc and Zr, the activation energy for hot deformation increases from 186.4 kJ/mol for the base composite (Al-15%B_4C) to 196.1 kJ/mol for S40 composite containing 0.4% Sc, and further to 206.6 kJ/mol for SZ40 composite containing 0.4% Sc and 0.24%Zr.

3. The predominant softening mechanism was dynamic recovery for three composites at low deformation temperature (300 ºC). When increasing the deformation temperature to 500 ºC, dynamic recrystallization became the main softening mechanism for the base composite, while dynamic recovery still controlled the softening process for S40 and SZ40.

4. Constitutive equations of three composites were established based on the hyperbolic-sine equation and the experimental compression data. The predicted

peak flow stresses on various deformation conditions were in good agreement with the experimental data for the three composites.

5. The processing maps of three composites were constructed at the 0.8 strain based on the dynamic materials model. The safe domains with optimal deformation conditions were identified and the hot workabilities of three composites were compared.

6. The flow instability zone of the base composite was located at low deformation temperatures (300-350 ºC) and high strain rates (0.04 to $1s^{-1}$). The addition of Sc and Zr extended the instability zones toward the higher temperature up to 380 ºC and the lower strain rate up to 0.002 s^{-1} for S40 and SZ40 composites. The defects generated during hot deformation, such as voids, cracking and flow localization around B_4C particles, were the major cause for the flow instability.

6.5 References

1. I.A. Ibrahim, F.A. Mohamed, and E.J. Lavernia, Particulate reinforced metal

matrix composites — a review, *J. Mater. Sci.*, 1991, **26**(5), p 1137-1156

2. J.X. Deng and J.L. Sun, Microstructure and mechanical properties of hot-pressed B4C/TiC/Mo ceramic composites, *Ceram. Int.*, 2009, **35**(2), p 771-778
3. T.K. Roy, C. Subramanian, and A.K. Suri, Pressureless sintering of boron carbide, *Ceram. Int.*, 2006, **32**(3), p 227-233
4. C.B. Fuller, D.N. Seidman, and D.C. Dunand, Mechanical properties of Al(Sc,Zr) alloys at ambient and elevated temperatures, *Acta Mater.*, 2003, **51**(16), p 4803-4814
5. Y.W. Riddle and T.H. Sanders, A study of coarsening, recrystallization, and morphology of microstructure in Al-Sc-(Zr)-(Mg) alloys, *Metall. Mater. Trans. A*, 2004, **35A**(1), p 341-350
6. N.A. Belov, A.N. Alabin, D.G. Eskin, and V.V. Istomin-Kastrovskii, Optimization of hardening of Al-Zr-Sc cast alloys, *J. Mater. Sci.*, 2006, **41**, p 5890-5899
7. Y. Li, Z. Liu, L. Lin, J. Peng, and A. Ning, Deformation behavior of an Al-Cu-Mg-Mn-Zr alloy during hot compression, *J. Mater. Sci.*, 2011, **46**(11), p 3708-3715
8. P. Cavaliere, Hot and warm forming of 2618 aluminium alloy, *J. Light Met.*, 2002, **2**(4), p 247-252
9. G. Ebrahimi, A. Zarei-Hanzaki, M. Haghshenas, and H. Arabshahi, The effect of heat treatment on hot deformation behaviour of Al 2024, *J. Mater. Process. Tech.*, 2008, **206**(1), p 25-29
10. X. Huang, H. Zhang, Y. Han, W. Wu, and J. Chen, Hot deformation behavior of 2026 aluminum alloy during compression at elevated temperature, *Mater. Sci. Eng., A*, 2010, **527**(3), p 485-490
11. H. Zhang, L. Li, D. Yuan, and D. Peng, Hot deformation behavior of the new Al-Mg-Si-Cu aluminum alloy during compression at elevated temperatures,

Mater. Charact., 2007, **58**(2), p 168-173

12. E. Cerri, E. Evangelista, A. Forcellese, and H. McQueen, Comparative hot workability of 7012 and 7075 alloys after different pretreatments, *Mater. Sci. Eng., A*, 1995, **197**(2), p 181-198
13. S. Chen, K. Chen, G. Peng, X. Chen, and Q. Ceng, Effect of heat treatment on hot deformation behavior and microstructure evolution of 7085 aluminum alloy, *J. Alloy. Compd.*, 2012, **537**, p 338-345
14. N. Jin, H. Zhang, Y. Han, W. Wu, and J. Chen, Hot deformation behavior of 7150 aluminum alloy during compression at elevated temperature, *Mater. Charact.*, 2009, **60**(6), p 530-536
15. J.N. Fridlyander, N.I. Kolobnev, O.E. Grushko, L.M. Sheveleva, L.B. Khokhlatova, W.S. Miller, and P.D. Couch, Alloying components optimization of weldable Ag-Li-Mg alloy, *Mater. Sci. Forum*, 1996, **217**, p 1847-1852
16. Y. Miura, T. Shioyama, and D. Hara, Recrystallization of Al-3Mg and Al-3Mg-0.2Sc alloys, *Mater. Sci. Forum*, 1996, **271**, p 505-510
17. O. Roder, O. Schauerte, G. Lutjering, and A. Gysler, Correlation between microstructure and mechanical properties of Al-Mg alloys without and with scandium, *Mater. Sci. Forum*, 1996, **271**, p 1835-1840
18. V.G. Davydov, V.I. Yelagin, V.V. Zakharov, Y.A. Filatov, On prospects of application of new 01570 high-strength weldable Al-Mg-Sc alloy in aircraft industry, *Mater. Sci. Forum*, 1996, **271**, p 1841-1846
19. M.E. Drits, L.S. Toropova, Y.G. Bykov, F.L. Gushchina, V.I. Elagin, and Y.A. Filatov, Metastable state diagram of the Al-Sc system in the range rich in aluminum, *Russ. Metall.*, 1983, (1), 150-153
20. W.S. Lee and T.H. Chen, Strain rate and temperature effects on dynamic properties of high-strength weldable aluminum-scandium alloy, *J. Mater. Res.*, 2009, **24**(1), 198-211

21. T.G. Nieh, L.M. Hsiung, J. Wadsworth, and R. Kaibyshev, High strain rate superplasticity in a continuously recrystallized Al-6%Mg-0.3%Sc alloy, *Acta Mater.*, 1998, **46**(8), 2789-2800
22. R. Kaibyshev, O. Sitdikov, and S. Olenyov, Ultrafine grain formation during equal channel angular extrusion in an Al-Mg-Sc alloy, *Ultrafine Grained Mater. II*, 2013, p 65-74
23. O. Sitdikov, T. Sakai, E. Avtokratova, R. Kaibyshev, Y. Kimura, and K. Tsuzaki, Grain refinement in a commercial Al-Mg-Sc alloy under hot ECAP conditions, *Mater. Sci. Eng., A,* 2007, **444**(1-2), p 18-30
24. C.B. Fuller, A.R. Krause, D.C. Dunand, and D.N. Seidman, Microstructure and mechanical properties of a 5754 aluminum alloy modified by Sc and Zr additions, *Mater. Sci. Eng., A*, 2002, **338**(1-2), p 8-16
25. M. Ferry, N.E. Hamilton, and F.J. Humphreys, Continuous and discontinuous grain coarsening in a fine-grained particle-containing Al-Sc alloy, *Acta Mater.*, 2005, **53**(4), 1097-1109
26. T. Srivatsan and J. Mattingly, Influence of heat treatment on the tensile properties and fracture behaviour of an aluminium alloy-ceramic particle composite, *J. Mater. Sci.*, 1993, **28**(3), p 611-620
27. T. Christman, A. Needleman, and S. Suresh, An experimental and numerical study of deformation in metal-ceramic composites, *Acta Metall.*, 1989, **37**(11), p 3029-3050
28. V. Srivastava, V. Jindal, V. Uhlenwinkel, and K. Bauckhage, Hot-deformation behaviour of spray-formed 2014 Al+SiC_P metal matrix composites, *Mater. Sci. Eng., A*, 2008, **477**(1), p 86-95
29. I. Dutta, J. Sims, and D. Seigenthaler, An analytical study of residual stress effects on uniaxial deformation of whisker reinforced metal-matrix composites, *Acta Metall. Mater.*, 1993, **41**(3), p 885-908
30. V. Senthilkumar, A. Balaji, and R. Narayanasamy, Analysis of hot

deformation behavior of Al 5083–TiC nanocomposite using constitutive and dynamic material models, *Mater. Design*, 2012, **37**, p 102-110

31. C. Chen, S. Qin, S. Li, J. Wen, Finite element analysis about effects of particle morphology on mechanical response of composites, *Mater. Sci. Eng., A*, 2000, **278**(1), 96-105
32. C. Sellars and W.M.G. Tegart, Relation between flow stress and structure in hot deformation, *Mem. Etud. Sci. Rev. Met.*, 1966, **67**(9), p 731-746
33. C.J. Shi, W.M. Mao, and X.G. Chen, Evolution of activation energy during hot deformation of AA7150 aluminum alloy, *Mater. Sci. Eng., A*, 2013, **571**, p 83-91
34. W.F. Gale and T.C. Totemeier, *Smithells metals reference book*, Butterworth-Heinemann, Oxford, 2003
35. S. Gangolu, A. Rao, N. Prabhu, V. Deshmukh, and B. Kashyap, Hot workability and flow characteristics of aluminum-5 wt.% B4C composite, *J. Mater. Eng. Perform.*, 2014, **23**(4), p 1366-1373
36. Y.V.R.K. Prasad, K.P. Rao, and S. Sasidhara, *Hot working guide: a compendium of processing maps*, ASM international, Ohio, 1997
37. H. Li, H. Wang, M. Zeng, X. Liang, and H. Liu, Forming behavior and workability of 6061/B4CP composite during hot deformation, *Compos. Sci. Technol.*, 2011, **71**(6), p 925-930
38. J. Qin, Z. Zhang, and X.-G. Chen, Mechanical Properties and Strengthening Mechanisms of Al-15 Pct B4C Composites with Sc and Zr at Elevated Temperatures, *Metall. Mater. Trans. A*, 2016, p 1-15
39. J. Qin, Z. Zhang, and X. Chen, Effect of hot deformation on microstructure and mechanical properties of Al-B4C composite containing Sc, *Mater. Sci. Forum*, 2014
40. J. QIN, Z. Zhang, and X-Grant CHEN, Mechanical properties and thermal stability of hot-rolled Al–15%B4C composite sheets containing Sc and Zr at

elevated temperature, *J. Comp. Mater.* (in press)

41. J. Lai, Z. Zhang, and X.G. Chen, The thermal stability of mechanical properties of Al-B4C composites alloyed with Sc and Zr at elevated temperatures, *Mater. Sci. Eng., A*, 2012, **532**, p 462-470
42. J. Lai, Z. Zhang, and X.G. Chen, Effect of Sc, Zr, and Ti on the interfacial reactions of the B_4C/Al system, *J. Mater. Sci.*, 2011, **46**(2), p 451-459
43. J. Lai, Z. Zhang, and X.G. Chen, Precipitation strengthening of Al–B4C metal matrix composites alloyed with Sc and Zr, *J. Alloy. Compd.*, 2013, **552**, p 227-235
44. C. Shi and X.G. Chen, Effect of Zr addition on hot deformation behavior and microstructural evolution of AA7150 aluminum alloy, *Mater. Sci. Eng., A*, 2014, **596**, p 183-193
45. S.S. Zhou, K.K. Deng, J.C. Li, K.B. Nie, F.J. Xu, H.F. Zhou, and J.F. Fan, Hot deformation behavior and workability characteristics of bimodal size SiCp/AZ91 magnesium matrix composite with processing map, *Mater. Design*, 2014, **64**, p 177-184
46. S. Spigarelli, E. Evangelista, E. Cerri, T.G. Langdon, Constitutive equations for hot deformation of an Al-6061/20%Al2O3 composite, *Mater. Sci. Eng., A*, 2001, **319–321**, p 721-725
47. Z.-Y. Zhang, Q.-L. Pan, J. Zhou, X.-Y. Liu, Q. Chen, Hot deformation behavior and microstructural evolution of Al–Zn–Mg–0.25Sc–Zr alloy during compression at elevated temperatures, *T. Nonferr. Metal. Soc.*, 2012, **22**(7), p 1556-1562
48. Z. Ma and S. Tjong, Creep deformation characteristics of discontinuously reinforced aluminium-matrix composites, *Compos. Sci. Technol.*, 2001, **61**(5), p 771-786
49. X. Wang, K. Wu, W. Huang, H. Zhang, M. Zheng, and D. Peng, Study on fracture behavior of particulate reinforced magnesium matrix composite

using in situ SEM, *Compos. Sci. Technol.*, 2007, **67**(11), p 2253-2260

50. H. Lüthy, R.A. White, and O.D. Sherby, Grain boundary sliding and deformation mechanism maps, *Mater. Sci. Eng.*, 1979, **39**(2), p 211-216
51. H.J. McQueen, S. Spigarelli, M.E. Kassner, and E. Evangelista, *Hot deformation and processing of aluminum alloys*, CRC Press, New York, 2011
52. P. Wouters, B. Verlinden, H. McQueen, E. Aernoudt, L. Delaey, and S. Cauwenberg, Effect of homogenization and precipitation treatments on the hot workability of an aluminium alloy AA2024, *Mater. Sci. Eng., A*, 1990, **123**(2), p 239-245
53. H.R. Ashtiani, M. Parsa, and H. Bisadi, Constitutive equations for elevated temperature flow behavior of commercial purity aluminum, *Mater. Sci. Eng., A*, 2012, **545**, p 61-67
54. Y. Prasad, H. Gegel, S. Doraivelu, J. Malas, J. Morgan, K. Lark, and D. Barker, Modeling of dynamic material behavior in hot deformation: forging of Ti-6242, *Metall. Trans., A*, 1984, **15**(10), p 1883-1892
55. P. Dadras and J. Thomas, Characterization and modeling for forging deformation of Ti-6Ai-2Sn-4Zr-2Mo-0.1 Si, *Metall. Trans., A*, 1981, **12**(11), p 1867-1876
56. A.K. Kumar, *Criteria for predicting metallurgical instabilities in processing maps*, Indian Institute of Science, Bangalore, 1987

CHAPTER 7

CONCLUSIONS AND SUGGESTION FOR FUTURE WORK

Chapter 7

Conclusions and suggestion for future work

7.1 Conclusions

In this thesis, scandium and zirconium as alloying elements were introduced into Al–15 vol.% B_4C composites to examine the effect of precipitates and B_4C particles on the mechanical properties and their thermal stability of as cast Al–B_4C composites at ambient and elevated temperatures. The strengthening mechanisms at ambient and elevated temperatures of the composites were clarified and a strengthening model was developed to predict yield strength of the composites at elevated temperatures. Moreover, the mechanical properties, thermal stability, microstructure and tensile fracture of two hot-rolled Al-15 vol.% B_4C composite sheets (4 mm) containing Sc and Zr, were investigated. The post-deformation heat treatment of the composite sheets was developed. In addition, the hot

deformation and processing maps of the composites with and without Sc and Zr additions were investigated. From the experimental results and the analyses, following conclusions are summarized, corresponding to the three aspects studied in the thesis.

Part I: Mechanical properties and strengthening mechanisms of Al–15%B_4C composites with Sc and Zr at elevated temperatures

1. The presence of large B_4C particles (15 vol.% with average size 23 μm) has a moderate strengthening effect on Al–B_4C composites. The yield strength contribution of 15vol.% B_4C is approximately 12 MPa at ambient temperature and remains about 10 MPa at 300 °C. The precipitation of nanoscale Al_3Sc and Al_3(Sc, Zr) in the composite matrix provides a significant and predominate contribution to the composite strength at both ambient and elevated temperatures.

2. During long-term thermal annealing, the Al_3Sc precipitates in the Al-15 vol.%B_4C composite with 0.4 wt.%Sc (S40) remain coarsening-resistant at 250 °C, whereas the Al_3(Sc, Zr) precipitates in the Al-15 vol.%B_4C composite with 0.4 wt.%Sc plus 0.24 wt.%Zr (SZ40) are thermally stable at 300 °C. At higher annealing temperatures 300 °C for S40 and 350 °C for SZ40, both Al_3Sc and Al_3(Sc, Zr) precipitates coarsen with increasing annealing time. The yield strengths of S40 and SZ40 at ambient temperature decrease with increasing precipitate size, which can be explained by the classical precipitate shearing and Orowan bypass mechanisms.
3. The yield strengths of S40 at 250 °C and 300 °C slightly increase in the first 500 h of annealing and subsequently remain constant till 2000 hours, whereas the yield strengths of the SZ40 at 300 °C and 350 °C are always stable up to 2000 hours. At elevated temperatures, the yield strengths of S40 and SZ40 become approximately independent of precipitate coarsening, which can be described and predicted by the dislocation climb mechanism.

4. The dislocation climb mechanism is invoked to explain the yield strength at elevated temperatures (> $0.5T_m$). The dislocation climb and Orowan bypass mechanisms are proposed as the governing strengthening mechanisms for high-temperature mechanical properties. The combination of dislocation climb and Orowan models can explain the lower strengthening efficiency of coherent precipitates and the stable strength with coarse precipitates at high temperature compared to those at ambient temperature. The predicted yield strengths at elevated temperatures are consistent with the experimental data of S40 and SZ40 composites.

Part II: Mechanical properties and their thermal stability of hot-rolled Al–15%B_4C composite sheets containing Sc and Zr at elevated temperatures

5. Alloying with Sc and Zr, the hot-rolled Al–15 vol.%B_4C composite sheets can regain a significant precipitation hardening under an appropriate post-rolling heat treatment, due

to the precipitation of nanoscale Al_3Sc and $Al_3(Sc,Zr)$ that uniformly distributed in aluminum matrix. After the peak aging, the UTS at ambient temperature of S40 (0.4 wt.%Sc containing) and SZ40 (0.4 wt.%Sc and 0.24 wt.%Zr containing) sheets can reach 197 MPa and 210 MPa, respectively. The tensile strength of both materials decreased with increasing test temperature. The UTS at 300 ºC of S40 and SZ40 became close and retained in the range of 65 MPa.

6. During 2000 h annealing at 300 ºC, a slow coarsening process occurred for Al_3Sc (S40) and $Al_3(Sc,Zr)$ (SZ40) precipitates. The strengths at ambient temperature of both S40 and SZ40 composite sheets decreased slowly with increasing annealing time. The UTS at ambient temperature of S40 changed from 197 to 190 MPa while the UTS of SZ40 decreased from 210 to 191 MPa after 2000 h annealing.
7. The UTS and YS at 300 ºC of both S40 and SZ40 composite sheets remained almost unchanged during 2000 h annealing and they were less sensible with annealing time and

more tolerable for precipitate coarsening, showing an excellent long-term thermal stability of both materials at elevated temperature.

8. The tensile fracture mechanism of both S40 and SZ40 composite sheets were temperature dependent. The fracture at ambient temperature was dominated by the brittle B_4C particle fracture, while the interfacial decohesion of B_4C particles became the prominent characteristic of the fracture at 300 ºC.

Part III: Hot deformation and processing maps of Al-15%B_4C composites with Sc and Zr

9. The flow stress increases with the increase of the deformation temperature and the decrease of the strain rate during hot deformation. The addition of Sc and Zr in Al-15%B_4C composites increases the flow stress, which is attributed to the synthetic effect of dynamic precipitation and solute atoms.

10. The activation energies are 187, 193 and 201 kJ/mol for the Al-15 vol.%B_4C (base composite), S40 and SZ40, respectively in the deformation temperature range (300-500 °C) and strain rate range (0.001-1s^{-1}). The additions of Sc and Zr moderately increase the activation energy for hot deformation of the Al–B_4C composites.
11. The predominant softening mechanism is dynamic recovery for the three composites at low temperature with high strain rate. When deformed at high temperature with low strain rate, dynamic recrystallization is the main softening mechanism for the base composite, but dynamic recovery still controls the softening process for S40 and SZ40. The additions of Sc and Zr limit the dynamic softening process, especially for dynamic recrystallization.
12. Constitutive equations of the three composites are established based on the hyperbolic-sine equation. The predicted peak stresses on various deformation conditions are in good agreement with the experimental data for the three composites.

13. The processing maps of the three experimental composites at a true strain of 0.8 are established. Two safe domains are recommended for each composite. The recommended domain I in the three composite are located in the similar deformation zone with high deformation temperatures and high strain rates. The recommended domain II of the composites containing Sc and Zr shifts to a region with a lower stain rate compared to the based composite.
14. The flow instability zones in the processing maps for three experimental composites are attributed to void formation, cracking and flow localization.

7.2 Suggestion for future work

The goal of this research is to develop the neutron absorber materials that are applicable and sustainable at elevate temperatures for spent nuclear fuel transport and storage. In the current study, the investigation is focused on the understanding of the materials behaviors and the mechanical properties at elevated temperatures, strengthening mechanisms, hot deformation and post deformation heat treatment. However, some

interesting questions still remain. The following extended study is recommended in the future work:

1) Dislocation climb mechanism and Orowan mechanism had been employed to explain elevated strengthening mechanism. However, the application conditions of dislocation climb mechanism are still not clear. Which temperature can the dislocation climb mechanism be active? What's the critical time and strain rate for a dislocation climb over a given size precipitate? These are some fundamental questions that need to be investigated.

2) During post deformation heat treatment for thin sheets, the alloying elements (particularly Sc) could be consumed. We already know that the heat treatment medium, solution temperature and deformation ratio would greatly affect the consumption. The diffusion rate of Sc and Zr under help of dislocation and subgrain boundaries and grain boundaries is uncertain. The quantity of the consumption in the atmosphere

furnace dependent on solution temperature can be investigated by TEM and image analysis.

3) The microstructure and mechanical properties of the composites by the optimized processing parameters in Chapter 6 are necessary to be verified.

4) The activation energies of the composites in Chapter 6 are calculated as average values. But it could be affected by test temperature and strain rate. Hence, a 3-D map, which can demonstrate the effect of test temperature and strain rate on activation energy, could be established. Also, dynamic precipitate occurs during the hot deformation in Chapter 6. The relations between precipitate radius and activation energy would be further studied.